PhD-FSTM-2022-152
The Faculty of Science, Technology and Medicine

DISSERTATION

Defence held on 20/12/2022 in Luxembourg

to obtain the degree of

DOCTEUR DE L'UNIVERSITÉ DU LUXEMBOURG

EN BIOLOGIE

by

Catherine DELBROUCK
Born on 24 March 1994 in Luxembourg (Luxembourg)

ELUCIDATING THE ROLE OF FORMATE ON CANCER CELL INVASION

Dissertation defence committee

Dr Johannes Meiser, dissertation supervisor
Luxembourg Institute of Health

Dr Virginie Neirinckx
Assistant Professor, Université de Liège

Dr Anne Grünewald, Chair
Professor, Université du Luxembourg

Dr Michael Ronellenfitsch
Universitätsklinikum Frankfurt

Dr Iris Behrmann, Vice Chair
Professor, Université du Luxembourg

“You are braver than you believe, stronger than you seem, and smarter than you think.”

Christopher Robin, Winnie the Pooh

The work presented in this thesis was conducted at the:

Cancer Metabolism Group (CMG)
Department of Cancer Research (DoCR)
Luxembourg Institute of Health (LIH)

The work presented in this thesis was sponsored by:

FNR-ATTRACT program (A18/BM/11809970)
Fonds National de la Recherche Luxembourg (FNR)

Doctoral Program in Systems and Molecular Biomedicine
Doctoral School in Science and Engineering (DSSE)
University of Luxembourg (uni.lu)

Fondation du Pélican de Mie et Pierre Hippert-Faber

Affidavit

I hereby confirm that the PhD thesis entitled “Elucidating the role of formate on cancer cell invasion” has been written independently and without any other sources than cited.

Luxembourg, the 7th of November 2022 **Catherine Delbrouck**

Acknowledgements

First, I wish to express my greatest gratitude to everyone who accompanied me on this challenging journey.
I thank the Luxembourg Institute of Health (LIH) as well as the University of Luxembourg (uni.lu) for providing me with the exceptional privilege to pursue my scientific adventure as a doctoral candidate. I also address my thanks to the Fonds National de la Recherche (FNR) and the Fondation du Pélican de Mie et Pierre Hippert-Faber for funding this project and for providing me with sufficient resources to finish my doctoral studies in the finest way.

I owe a special thanks to my supervisor Dr Johannes Meiser for welcoming me as the first PhD student in his Cancer Metabolism Group. I thank you for your continuous support during the last four years, our stimulating scientific discussions, your extraordinary constructive feedback, and our social exchanges over a glass of cold beer. Your passion for the one-carbon metabolism is contagious and inspires me every day!

I thank my non-supervising CET members, Dr Simone Niclou and Dr Alexander Skupin for their guidance and helpful comments. I also want to thank the members of my defence jury, Dr Iris Behrmann, Dr Anne Grünewald, Dr Johannes Meiser, Dr Virginie Neirinckx and Dr Michael Ronellenfitsch. Thank you for having accepted to evaluate my thesis, and dedicate some of your time to read what with effort and dedication I have compiled during the last four years. Your constructive criticism of my work and your presence at the thesis defence is greatly valued.
Special thanks, to Dr Elisabeth Letellier and Dr Vitaly Pozdeev for excellent and efficient collaboration in the *in vivo* part of this study. I would also like to express my gratitude to Anaïs Oudin and Virginie Baus from NORLUX for performing the *in vivo* brain tumour experiment. A big thank you to our collaborators at the Helmholtz AI department Dr Marie Piraud and her PhD student Ruolin Shen for providing us with a python script for automated Boyden chambers count. I also want to thank Dr Aymeric Fouquier d'Hérouël for equipping us with a Fiji Macro identifying the signal distribution in the two brain hemispheres. Next, I would like to acknowledge the great work of Dr Rashi Halder on the RNAseq analysis. Special thanks to Dr Michael W. Ronellenfitsch and Nadia I. Lorenz for supplying AMPK-deficient LN-229 cells. I would also like to thank Dr Christian Jaeger, Xiangyi Dong and Floriane Gavotto from the metabolomic platform at the Luxembourg Center for System Biomedicine (LCSB) for their valuable comments and their high-quality work. I express a big thank you to Dr Antoine Lesur and Francois Bernardin for building up a high-quality metabolomic platform at LIH.

Next, I express my deepest gratitude to all the members of the Cancer Metabolism Group. The lab experience would not have been the same without your endless support. You did not only help me to improve my technical skills but also taught me what a healthy work environment should look like.
Thank you for not only being team members but also being good friends.
A particular thanks to Dr Nicole Kiweler, for … everything! Thank you for your assistance in the laboratory, your ideas for the project, your critical feedback, your meticulous corrections, and your mental support. My research experience would not have been half as enjoyable without our nice chats in the office. Thank you very much for the last 4 years; you are a true inspiration for every young researcher!

Major thanks to Laura Neises, who always had time for me inside and outside of the lab. Thank you for the many hours of excellent support and good humour. Your good mood is highly contagious (even in the darkest times of the PhD period).

Big thanks to Dr Björn Becker for his constructive feedback and his various ideas for my project. I enjoyed always our living discussions. You can, and will, fill every silence!

Thank you also to our newest team member Dr Oleg Chen for helping to uncover the underlying mechanism how formate promotes invasion. I wish you all the best.

I would also like to thank my fellow PhD mates Lara Haase, Mohaned Benzarti, and Kim Eiden.
Thank you, Lara, for always having time for a tasteful break with (chocolate) cake and ice cream. It was always fun to talk with you about life-changing topics.
Thank you, Mohaned, for always making time for me and teaching me how to use the Tracefinder software.
Thank you, Kim, for supporting me during the last months of my doctoral studies.
Although I would like to continue to thank everyone individually, I risk filling hundreds of pages but still forgetting one of you. Thus, I address a cumulative thank you to all of you, PhD students, Post-Docs, PIs and technicians from BAM -1, -2, -3, LCSB, and everyone else who contributed to my work, who provided me with the necessary tools for my research, or who joined me for some leisure activities.

I would like to end with a personal thank you, to my entire family for their tremendous support during my academic journey. I cannot express my appreciation for knowing you on my side. Although you did not fully understand what I was doing, you always listened to my never-ending lab stories. Finally, yet importantly, I want to specifically thank Dr Jim Barthel for his mental and scientific support over the last ten years. Thank you for sharing my suffering and joy over all this time. I would not have reached this academic level without your teaching units explaining to me basic science, especially mathematics.

For all of you who contributed to this memorable adventure, even just in the subtlest way possible – Thank you!

Table of Contents

List of Publications and Manuscripts

The following thesis will be based on the below mentioned manuscript:

- Research publication (*first author*)

Formate Promotes Invasion and Metastasis by Activating Fatty Acid Synthesis and Matrix Metalloproteinases

Catherine Delbrouck, Nicole Kiweler, Vitaly I. Pozdeev, Laura Neises, Anaïs Oudin, Anne Schuster, Aymeric Fouquier d'Hérouël, Ruolin Shen, Rashi Halder, Antoine Lesur, Christoph Ogris, Nadia I. Lorenz, Christian Jaeger, Michael W. Ronellenfitsch, Marie Piraud, Alexander Skupin, Simone P. Niclou, Elisabeth Letellier, Johannes Meiser
Under Review in "Cell Reports"

Additional publications that are not further discussed in the thesis:

- Review publication (*shared first author*)

Metabolic Potential of Cancer Cells in Context of the Metastatic Cascade
Mohaned Benzarti, Catherine Delbrouck, Laura Neises, Nicole Kiweler, Johannes Meiser
DOI: 10.3390/cells9092035
Cells (2021)

- Research publication (*co-author*)

The gut microbial metabolite formate exacerbates colorectal cancer progression

Dominik Ternes, Mina Tsenkova, Vitaly I. Pozdeev, Marianne Meyers, Eric Koncina, Sura Atatri, Martine Schmitz, Jessica Karta, Maryse Schmoetten, Almut Heinken, Fabien Rodriguez, Catherine Delbrouck, Anthoula Gaigneaux, Aurelien Ginolhac, Tam Thuy Dan Nguyen, Lea Grandmougin, Audrey Frachet-Bour, Camille Martin-Gallausiaux, Maria Pacheco, Lorie Neuberger-Castillo, Paulo Miranda, Nikolaus Zuegel, Jean-Yves Ferrand, Manon Gantenbein, Thomas Sauter, Daniel Joseph Slade, Ines Thiele, Johannes Meiser, Serge Haan, Paul Wilmes, Elisabeth Letellier
DOI: 10.1038/s42255-022-00558-0
Nature Metabolism (2022)

- Research publication (*co-author*)

Mitochondria preserve an autarkic one-carbon cycle to confer growth-independent cancer cell migration and metastasis

Nicole Kiweler, Catherine Delbrouck, Vitaly Pozdeev, Laura Neises, Leticia Soriano-Baguet, Kim Eiden, Feng Xiang, Mohaned Benzarti, Lara Haase, Eric Koncina, Maryse Schmoetten, Christian Jäger, Muhammad Noman, Alexei Vazquez, Bassam Janji, Gunnar Dittmar, Dirk Brenner, Elisabeth Letellier, Johannes Meiser
DOI: 10.1038/s41467-022-30363-y
Nature Communications (2022)

List of Abbreviations

A	
Amino Acids	aa
Acetyl-CoA Carboxylase	ACC
Acetonitrile	ACN
Alzheimer's Disease	AD
A Disintegrin and Metalloproteinase with Thrombospondin Motifs	ADAMTS
Adenosine Diphosphate	ADP
Aryl Hydrocarbon Receptor	AHR
Alanine	Ala
Aldehyde Dehydrogenase 1 Family Member L2	ALDH1L2
Adenosine Monophosphate	AMP
AMP-activated Protein Kinase	AMPK
Aspartate	Asp
Adenosine Triphosphate	ATP
B	
Basic Fibroblast Growth Factor	bFGF
C	
Carbonyl Cyanide M-Chlorophenyl Hydrazone	CCCP
Complementary DNA	cDNA
Citrate	Cit
Consumption And Release Rate	CORE
Colorectal Cancer	CRC
Cycle Threshold	Ct
One-Carbon	1C
D	
4′,6-Diamidino-2-Phenylindole	DAPI
2',7'-Dichlorofluorescein Diacetate	DCFDA
Dihydrofolate Reductase	DHFR
Dulbecco's Modified Eagle's Medium	DMEM
Deoxyribonucleic Acid	DNA
Dithiothreitol	DTT
Deoxythymidine Monophosphate	dTMP
Deoxyuridine Monophosphate	dUMP
2-Deoxy-D-Glucose	2DG
E	
Extracellular Matrix	ECM
Ethylenediaminetetraacetic Acid	EDTA
Epidermal Growth Factor	EGF

Epithelial-to-Mesenchymal Transition	EMT
Electron Transport Chain	ETC
Ethanol	EtOH
F	
Fatty Acid Desaturase 2	FADS2
Fatty Acid Synthesis	FAS
Fatty Acid Synthase	FASN
Foetal Bovine Serum	FBS
Free Fatty Acid Receptor 1	FFAR1
Formyl-Peptide Receptor	FPR
Folylpolyglutamate Synthetase	FPGS
Fumarate	Fum
G	
Glioblastoma	GBM
Gas Chromatography	GC
Genetically Engineered Mouse Models	GEMMs
Green Fluorescent Protein	GFP
Glucose	Gluc
Glutamine	Gln
Glycine	Gly
Glioblastoma Stem-Like Cells	GSC
Gene Set Enrichment Analysis	GSEA
Glutathione	GSH
Glutathione disulfide	GSSG
Genome-Wide Association Studies	GWAS
Glucose-6-Phosphate	G6P
H	
Hydrochloric Acid	HCl
β-Hydroxy β-Methylglutaryl-CoA	HMG-CoA
Hematoxylin & Eosin	H&E
I	
Ion Chromatography	IC
Insulin-Induced Gene 1	INSIG1
Immunoprecipitation	IP
J	
K	
Knock-Down	KD
Knock-Out	KO
α-Ketoglutarate	αKG
L	

Lactate	Lac
Liquid Chromatography	LC
Leucine	Leu
Lysine	Lys
M	
Malate	Mal
Methanol	MeOH
Methionine	Met
Mitochondrial Folate Transporter	MFT
Mass Isotopologue Distribution	MID
Matrix Metalloproteinase	MMP
Matrix Metalloproteinase inhibitor	MMPi
Messenger Ribonucleic Acid	mRNA
Mass Spectrometry	MS
Mass Selective Detector	MSD
N-Tert-Butyldimethylsilyl-N-Methyltrifluoroacetamide	MTBSTFA
Methylenetetrahydrofolate Dehydrogenase 1	MTHFD1
Methylenetetrahydrofolate Dehydrogenase 2	MTHFD2
Methylenetetrahydrofolate Dehydrogenase 1 Like	MTHFD1L
Methylenetetrahydrofolate Reductase	MTHFR
Mechanistic Target of Rapamycin Complex 1	mTORC1
Methotrexate	Mtx
N	
Sodium-Formate	Na-formate
N-Acetyl-L-Cysteine	NAC
Sodium Chloride	NaCl
Nuclear Magnetic Resonance	NMR
Neural Tube Defects	NTDs
O	
Oxygen Consumption Rate	OCR
P	
Phosphate-Buffered Saline	PBS
Packed Cell Volume	PCV
Phosphoglycerate Dehydrogenase	PHGDH
Poly-L-Lysine	PLL
Oxygen Partial Pressure	pO_2
Pentose Phosphate Pathway	PPP
Pyruvate	Pyr
3-Phosphoglycerate	3PG
Q	

R	
RNA Integrity Number	RIN
Ribonucleic Acid	RNA
Reactive Oxygen Species	ROS
Quantitative Reverse Transcription PCR	RT-qPCR
S	
S-Adenosyl Methionine	SAM
Stearoyl-CoA Desaturase 1	SCD
Standard Deviation	SD
Sodium Dodecyl Sulfate	SDS
Standard Error of the Mean	SEM
Serine	Ser
Sideroflexin 1	SFXN1
Serine Hydroxymethyltransferase	SHMT
Sphingolipids	SL
Single Nucleotide Polymorphism	SNP
Sterol Regulatory Element Binding Transcription Factor	SREBF
Serine Synthesis Pathway	SSP
Succinate	Suc
T	
Tumour-Associated Macrophages	TAMs
Tert-Butyldimethylchlorosilane	TBDMCS
Tris-Buffered Saline	TBS
TBS with Tween® 20 Detergent Solution	TBS-T
Tricarboxylic Acid Cycle	TCA
Tetrahydrofolate	THF
Tumour Interstitial Fluid	TIF
Thymidylate Synthase	TYMS
Tumour Microenvironment	TME
Tongue Squamous Cell Carcinoma	TSCC
U	
V	
Valine	Val
W	
World Health Organisation	WHO
Wild Type	WT.
X	
Y	
Z	

List of Illustrations

List of Figures

Summary

Metabolic rewiring is essential to enable cancer onset and progression. One important metabolic pathway that is often hijacked by cancer cells is the one-carbon (1C) cycle, in which the third carbon of serine is oxidized to formate. It was previously shown that formate production in cancer cells often exceeds the anabolic demand, resulting in formate overflow. Furthermore, extracellular formate was described to promote the *in vitro* invasiveness of glioblastoma (GBM) cells. Nevertheless, the mechanism underlying the formate-induced invasion remains elusive.

In this present study, we aimed to characterize formate-induced invasion in greater detail. At first, we studied the generalizability of formate-induced invasion in different GBM models as well as in different breast cancer models. We applied different *in vitro* assays, like the Boyden chamber assay to probe the impact of formate on different cancer cell lines. Then, we studied the *in vivo* relevance and the pro-invasive properties of formate in physiological models by using different *ex vivo* and *in vivo* models. Lastly, we investigated the mechanism underlying the formate-dependent pro-invasive phenotype. We applied a variety of different biochemical as well as cellular assays to investigate the underlying mechanism.

In the present study, we underline that formate specifically promotes invasion and not migration in different cancer types. Furthermore, we now demonstrate that inhibition of formate overflow results in a decreased invasiveness of GBM cells *ex vivo* and *in vivo*. Using breast cancer models, we also obtain first evidence that formate does not only promote local cancer cell invasion but also metastasis formation *in vivo*, suggesting that locally increased formate concentrations within the tumour microenvironment promote cancer cell motility and dissemination.

Mechanistically, we uncover a previously undescribed interplay where formate acts as a trigger to alter fatty acid metabolism, which in turn affects cancer cell invasiveness and metastatic potential via matrix metalloproteinase (MMP) release.

Gaining a better mechanistic understanding of formate overflow, and how formate promotes invasion in cancer, may contribute to preventing cancer cell dissemination, one of the main reasons for cancer-related mortality.

Introduction

1. The Hallmarks of Cancer

Cancer is a group of diseases characterized by abnormal cell growth with the potential to invade or spread to other parts of the body (Meza-Junco et al., 2006). It consists in one of the most severe diseases affecting the global population. According to the World Health Organization (WHO), cancer is the second leading cause of death worldwide, accounting for nearly 10 million deaths in 2020 (Ferlay J, 2020).

Tumorigenesis is a complex and multi-step process that reflects the accumulation of genetic and epigenetic alterations in the cell. In 2000, Hanahan and Weinberg published in their seminal analysis “The Hallmarks of Cancer” six essential physiological alterations that collectively dictate malignant growth (Hanahan and Weinberg, 2000). The hallmarks included: (1) self-sufficiency in growth signals, (2) insensitivity to growth-inhibitory signals, (3) evasion of programmed cell death, (4) limitless replication potential, (5) sustained angiogenesis, and (6) tissue invasion and metastasis (Hanahan and Weinberg, 2000). These hallmarks of cancer describe a set of functional characteristics that have to be acquired during the process of oncogenesis. Understanding cancer formation and progression as a complex, multi-step process explains the increase in cancer incidence with age. Indeed, as mutagenic events are rare incidences, the evolution of a healthy cell into a neoplastic cell is long-lasting. Yet, exposure to carcinogens has been identified to increase the number of harmful changes in the cell, which leads to cancer development at a younger age (Loeb and Harris, 2008).

Although the hallmarks of cancer underline similarities between multiple cancer entities, the acquisition of those characteristics varies, both mechanistically as well as chronologically (Hanahan and Weinberg, 2000).

The hallmark model of Hanahan and Weinberg soon became an essential resource for cancer research and provides a comprehensive foundation for understanding and studying cancer biology. Recent technological advances and new bioinformatic tools pushed cancer research forward. To account for the progress in the field, Hanahan and Weinberg extended their hallmarks of cancer over the last years (Hanahan, 2022; Hanahan and Weinberg, 2000, 2011). In 2011, the authors added two new hallmarks: (7) reprogramming of energy metabolism and (8) evading immune destruction (Hanahan and Weinberg, 2011). Beginning of this year, Hanahan pointed out the importance of the hallmarks of cancer and added (9) phenotypic plasticity and disrupted differentiation as new features (Hanahan, 2022).

2. The Hallmarks of Metastasis

Metastasis is the primary cause of cancer-related death. It is estimated that the five-year survival rate of metastatic diseases is below 30% (Siegel et al., 2020). Metastasis is a multi-step process whereby distinct cancer cells within a tumour dissociate and propagate into the surrounding tissue.

In most cases, metastasis starts with a single cell that detaches from the primary tumour, migrates, invades the neighbouring environment, enters the vascular system by intravasation, survives in the bloodstream, exits the bloodstream by extravasation, migrates to a distant organ, adapts to the new microenvironment, and proliferates to form a macrometastasis (Benzarti et al., 2020; Welch and Hurst, 2019) (**Illustration 1**).

Among the hallmarks, invasion was the only characteristic defining the process of disseminating cancer cells (Welch and Hurst, 2019). Thus in 2019, Welch and Hurst further defined the “hallmarks of metastasis”, describing essential characteristics that neoplastic cells have to acquire to become malignant (Welch and Hurst, 2019). To detach from the primary tumour and disseminate elsewhere, the neoplastic cells have to (1) become motile and invasive, (2) modulate the surrounding environment, (3) undergo molecular and phenotypic changes (plasticity), and (4) colonize a non-native environment (Welch and Hurst, 2019) (**Illustration 1**).

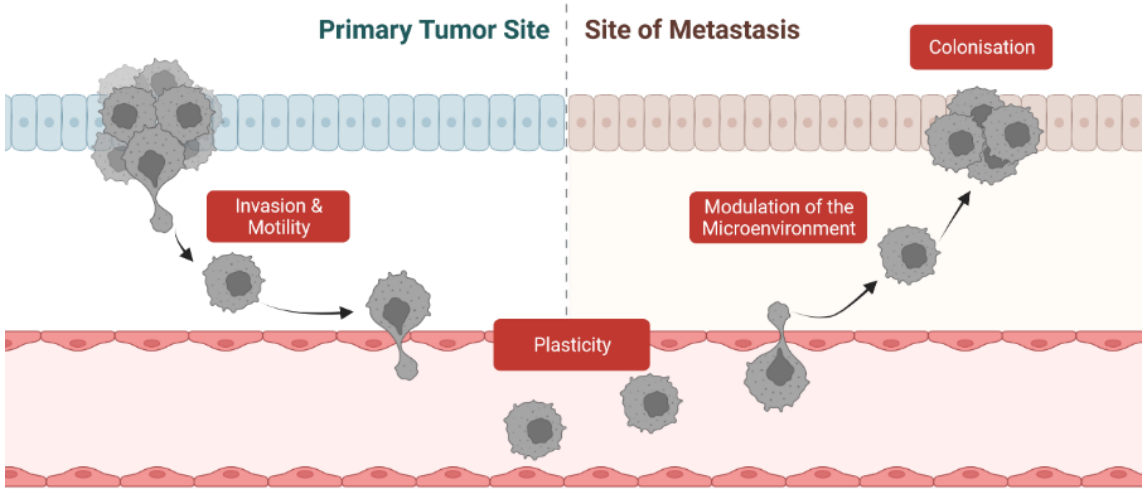

Illustration 1: The Hallmarks of Metastasis
Neoplastic cells begin to invade through the surrounding stroma via a variety of motility mechanisms. After detaching from the primary tumour, the neoplastic cells have to intravasate into the vascular system, survive within the bloodstream, extravasate into a distant organ, adapt to the new microenvironment, and multiply to form macrometastases. Adapted from (Welch and Hurst, 2019) and created with BioRender.com.

2.1 Invasion & Motility

Two distinct mechanism with regard to cell motility have been described in cancer biology: migration and invasion. While cell migration refers to an active cell movement on the surface, invasion is defined as the restructuring and destructive movement of a cell through a 3D barrier. Although epithelial-to-mesenchymal transition (EMT) is often assumed to be indispensable for cancer cell invasion, increasing evidence suggests the necessity of additional mechanisms to support tumour cell dissemination (Krakhmal et al., 2015). To successfully spread into the surrounding tissues, cancer cells underlie migratory mechanisms that are similar to those that occur in normal physiological processes. More precisely, cancer cell motility is orchestrated by a sequence of complex interdependent processes involving cytoskeletal modifications, changes in cell-substrate adhesive properties as well as the alteration in the extracellular matrix (ECM).

The invasion begins with the loss of cell-ECM and cell-cell adhesion (Fogar et al., 1997; Johnson, 1991; Kaiser et al., 1996). The loss of cell-cell adhesion permits cells to detach from the primary tumour and changes in cell-ECM adhesion allow the cells to disseminate into the surrounding stroma. Several families of biochemically and genetically unique cell receptors have been identified to play a major role in cancer cell invasion comprising the integrins, cadherins and selectins (Bussemakers and Schalken, 1996). In the second step of the invasion, freely migrating cancer cells invade the surrounding tissue. To efficiently migrate, cytoskeleton components like actin, myosin, intermediate filaments, and their associated proteins have to operate in a coordinated way to produce the required traction force to move forwards (Aseervatham, 2020). Finally, to invade through the surrounding 3D barrier, cancer cells have to secrete substances that degrade the basement membrane and the ECM. Protease genes upregulation, and protease inhibitor genes downregulation have been identified in many cancers (Coussens and Werb, 1996).

Although cancer cell invasion has been described as one of the hallmarks of cancer, the exact molecular mechanism underlying tumour cell migration and invasion through multiple different microenvironments remains incompletely understood.

Tumour cells can invade as single cells via an amoeboid or a mesenchymal mode, or move as a group of collective cells (Krakhmal et al., 2015; Wu et al., 2021) (**Illustration 2**). Amoeboid invasion is characterized by fast, small and roundish cells that can squeeze through narrow spaces and small pores of the ECM in the absence of tumour microenvironment remodelling. Experiments have shown that this process is accompanied by cell volume reduction (30-35%), allowing cells to invade while maintaining weak adhesion to the ECM. This mode of invasion is characterised by swift changes in the cell shape and the expansion of filopodia allowing cells to examine their microenvironment and move through small gaps in the matrix (Eichinger et al., 2005; Krakhmal et al., 2015; Wu et al., 2021).

Conversely, mesenchymal-type cells exhibit an elongated, spindle-like shape triggered by changes in the cytoskeleton. Indeed, mesenchymal displacement is characterized as a slow and complex process which generates traction forces through cytoskeletal rearrangements and integrin-mediated ECM-adhesion (Pearson, 2019). Furthermore, mesenchymal invasion relies on proteolytic ECM degradation to generate invasion paths in the microenvironment (Wu et al., 2021).

It became evident that tumour cells can switch between these two invasion modes in response to the tumour microenvironment (TME). Indeed, experiments identified migratory plasticity of cancer cells due to ECM stiffness (Taddei et al., 2013). Distinct from individual cell invasion, collective cell migration is characterized by a coherent movement of a group of cells maintaining cell-cell connections. This type of cancer cell movement depends on actin dynamics, integrin-based ECM adhesion, and ECM degradation. Collective migration consists of heterogeneous tumour cells including front-leading cells, which sense and release guidance signals (Haeger et al., 2015; Wu et al., 2021).

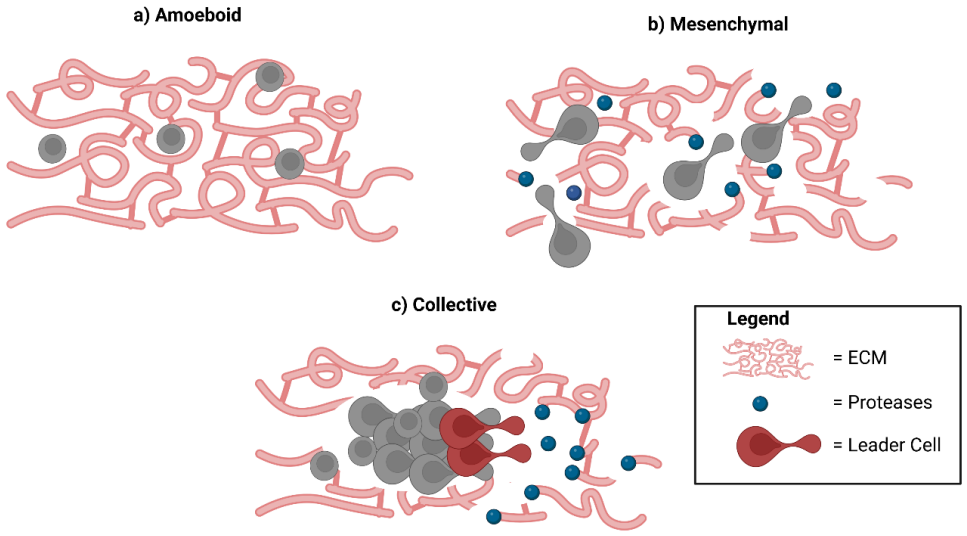

Illustration 2: Different Models of Tumour Cell Invasion
Tumour cells can invade as single cells through an amoeboid or mesenchymal mode, or move as a group of collective cells. Each mode can be distinguished through several distinct characteristics. Adapted from (Wu et al., 2021) and created with BioRender.com.

2.1.1 Proteolysis of the Extracellular Matrix

The main difference between amoeboid and mesenchymal invasion is, that the mesenchymal mode requires active ECM degradation.

The ECM forms an extremely versatile environment surrounding the cells and plays many functions in addition to its structural role. Indeed, ECM plays an important role in basic cellular processes, such as proliferation, adhesion, migration, and differentiation (Hynes, 2009). Being highly dynamic, the ECM can easily change its composition. Biochemically, ECM components are glycoproteins, proteins, and proteoglycans, each of which can be subdivided according to their physical and biochemical properties (Bonnans et al., 2014).

To effectively invade, mesenchymal-type cells have to create an invasion path by actively degrading the ECM. The most relevant enzymes involved in ECM remodelling are metalloproteinases. Metalloproteinases are grouped into two main families: (1) matrix metalloproteinase (MMP) and (2) A disintegrins and metalloproteinase with thrombospondin motifs (ADAMTS) (Lu et al., 2011).

In vertebrates, including humans, 23 different MMPs have been identified (**Illustration 3**). MMPs are zinc-dependent endopeptidases that are involved in tissue remodelling by targeting a wide range of ECM components and other extracellular proteins. For instance, MMP3 and MMP10 target proteoglycans, fibronectin, and laminin. MMP1 targets collagen III, MMP8 collagen I and MMP13 collagen II. In addition, MMP2 and MMP9 degrade gelatin (Cawston and Young, 2010).

Subgroup	MMP	Name	Substrate
1. Collagenases	MMP-1	Collagenase-1	Col I, II, III, VII, VIII, X, gelatin
	MMP-8	Collagenase-2	Col I, II, III, VII, VIII, X, aggrecan, gelati
	MMP-13	Collagenase-3	Col I, II, III, IV, IX, X, XIV, gelatin
2. Gelatinases	MMP-2	Gelatinase A	Gelatin, Col I, II, III, IV, VII, X
	MMP-9	Gelatinase B	Gelatin, Col IV, V
3. Stromelysins	MMP-3	Stromelysin-1	Col II, IV, IX, X, XI, gelatin
	MMP-10	Stromelysin-2	Col IV, laminin, fibronectin, elastin
	MMP-11	Stromelysin-3	Col IV, fibronectin, laminin, aggrecan
4. Matrilysins	MMP-7	Matrilysin-1	Fibronectin, laminin, Col IV, gelatin
	MMP-26	Matrilysin-2	Fibrinogen, fibronectin, gelatin
5. MT-MMP	MMP-14	MT1-MMP	Gelatin, fibronectin, laminin
	MMP-15	MT2-MMP	Gelatin, fibronectin, laminin
	MMP-16	MT3-MMP	Gelatin, fibronectin, laminin
	MMP-17	MT4-MMP	Fibrinogen, fibrin
	MMP-24	MT5-MMP	Gelatin, fibronectin, laminin
	MMP-25	MT6-MMP	Gelatin
6. Others	MMP-12	Macrophage metalloelastase	Elastin, fibronectin, Col IV
	MMP-19		Aggrecan, elastin, fibrillin, Col IV, gelati
	MMP-20	Enamelysin	Aggrecan
	MMP-21	XMMP	Aggrecan
	MMP-23		Gelatin, casein, fibronectin
	MMP-27	CMMP	Unknown
	MMP-28	Epilysin	Unknown

Illustration 3: Table of Different Identified MMPs
(Cawston and Young, 2010)

Upregulation of MMP expression was associated with cancer, shorter progression-free survival and a shorter relapse-free time in lung, colon, ovarian, head and neck, thyroid, breast, prostate, and gastric carcinoma (Lu et al., 2011; Westermarck and Kähäri, 1999). Yet, specific MMP expression is tumour type-specific. For example, the expression of MMP1 was identified to positively correlate with poor prognosis in colorectal cancer and oesophageal cancer (Murray et al., 1998; Murray et al., 1996). In contrast, MMP2 and MMP3 expression was found to be upregulated in metastatic oesophageal carcinomas (Shima et al., 1992), while MMP2 and MMP9 were identified to play an important role in human gliomas (Wang et al., 2003).

The ADAMTS enzymes are multi-domain matrix-associated zinc metalloendopeptidases that have different roles in tissue remodelling. 19 members of ADAMTS proteinases have been identified in humans and most of them target proteoglycans. For illustration, ADAMTS -1, -4, -5, -8, -9, -15, -16, and -18 are proteoglycanases (Apte, 2009).

2.2 Cellular Plasticity

Throughout the metastatic cascade, the cancer cells must adapt to dynamic changes, triggered by external signals. To be precise, during the dissemination process, cancer cells must respond to continuously changing tumour microenvironmental conditions, including oxygen partial pressure (pO_2), nutrients, and mechanical stress (Benzarti et al., 2020; Welch and Hurst, 2019). Only cells that effectively adapt to the distinct microenvironments can metastasise to a distant organ (**Illustration 1**). Loss of plasticity (i.e., in terminally differentiated cells) was shown to result in the inability to form metastases (Ishay-Ronen et al., 2019).

2.3 Modulation of the Microenvironment

The intercommunication between neoplastic cells and the surrounding environment is of the highest importance (**Illustration 1**). During tumorigenesis, the ECM functions as a biological barrier limiting cancer cell proliferation and metastasis. However, the cancer cells can transform the ECM for their benefit. Indeed, disseminating cells release cytokines and growth factors into the surrounding environment to recruit and reprogram stromal cells, such as fibroblasts and immune cells. Furthermore, cancer cells secrete enzymes, such as MMPs, that degrade and remodel the surrounding ECM (Neophytou et al., 2021). For example, cancer cells recruit macrophages via chemokines production to support tumorigenesis. M2-type tumour-associated macrophages (TAMs) are pro-tumorigenic and exert immunosuppressive functions by producing IL-10-inducing angiogenesis and stimulating tumour cells to release MMPs that favour cancer progression by disrupting the ECM (Neophytou et al., 2021).

2.4 Colonisation

The colonisation of distant organs represents the last critical step in metastasis. It is estimated that only 0.01% of cancer cells that are injected directly into the bloodstream form macrometastases (Chambers et al., 2002; Luzzi et al., 1998). Having travelled from the primary tumour to the secondary tumour site, cancer cells are exposed to a new tissue microenvironment, containing distinct stromal cells, growth factors, and ECM constituents. Once arrived on the new site, cells must adapt to the new microenvironment, initiate and maintain growth to form metastases, and also sustain the development of new blood

vessels (Chambers et al., 2002). It has long been recognised that some types of cancer show an organ-specific pattern of metastasis (seed and soil hypothesis) (Paget, 1989). Indeed, tumour metastasis is the product of favourable interactions between metastatic tumour cells (the “seed”) and the organ microenvironment (the “soil”) (Savci-Heijink et al., 2015). For example, breast cancer frequently metastasises into the liver, lungs, bone, and brain, whereas prostate cancer preferentially metastases into the bone.

2.5 Experimental Assays and Models to Study Invasion and Metastasis

Due to the high importance of invasion in the metastatic process, a broad range of experimental methods to quantify cancer cell invasion has been established. Some of the most relevant experiments are enumerated in the following:

Scratch Assay: Cell invasion can be assessed using a scratch wound assay. Using a pin tool or a needle, cells are removed from a discrete area of a confluent monolayer. The remaining cells have to migrate to close the wound. To study invasion instead of migration, the resulting wound is covered with ECM. To close the wound, the cells must now invade this matrix.

Invasion is determined as a measurement of the cell density (confluence) in the wound area when compared to the outer spatial cell density, or as the variation of the wound width over time, or as the area change over time. Essen BioScience has commercialized a WoundMaker Tool as well as a software to analyse the corresponding scratch assays (Hulkower and Herber, 2011) (**Illustration 4**).

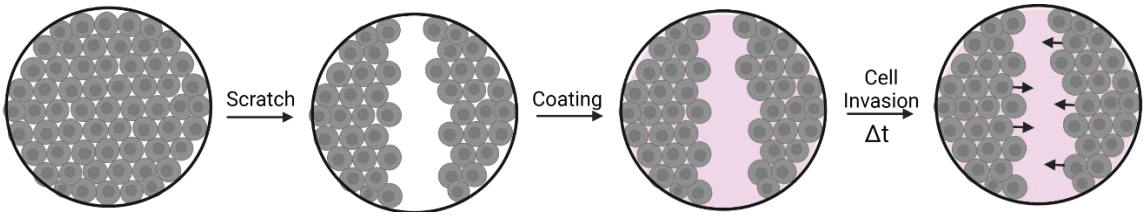

Illustration 4: Scratch Wound Assay
Schematic representation of a Scratch Wound Assay. Illustration created with BioRender.com

Scratch wound assays provide several advantages: (1) The experiment is fast and can be performed in a 96-well plate by using the commercialized tool set by Essen BioScience. (2) Invasion can be studied on different matrices as the surface can be coated with an ECM of choice. (3) At last, the movement and morphology of the cells can be visualized at any moment of the experiment.

However, there are also some negative aspects of this experimental setup: (1) The scratch wound assay does not mimic the microenvironment, as the cells are cultured as an artificial monolayer. (2) Invasion is not normalized on cancer cell proliferation. (3) The scratch wound assay can only be performed with adherent cells.

Transmembrane Assay: Cell invasion can be measured using a Boyden chamber assay. In this assay, cells are seeded on a coated membrane, while a solution containing a chemoattractant is pipetted into the lower part of the chamber. After an incubation period, invasion through the coated membrane is quantified by counting the number of cells that invaded the lower part of the chamber (Hulkower and Herber, 2011) (**Illustration 5**).

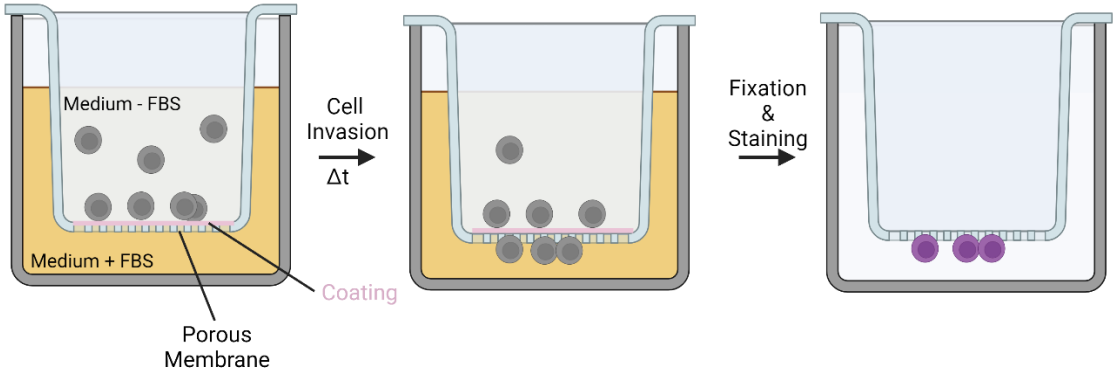

Illustration 5: Boyden Chamber Assay
Schematic representation of a Boyden chamber assay. Illustration created with BioRender.com

Transmembrane assays provide several advantages: (1) Invasion can be studied on different matrices as the surface can be coated with an ECM of choice. (2) Boyden chamber assays can be used with adherent and non-adherent cells. (3) The experiment is fast and easy to perform. (4) Finally, this method also allows to separate invading and non-invading cells.

Some drawbacks of this experiment when compared to other assessment methods are: (1) The chemoattractant gradient is non-linear as it equilibrates between both compartments over time. (2) The cells can only be visualized at the end-point of the experiment. (3) As the cells have to invade through a polycarbonate or polypropylene filter, this experiment does not mimic the *in vivo* microenvironment. (4) Cell-clumping and over-trypzination can falsify the results. (5) Accurate and statistically significant results are difficult to obtain when only a low number of cells pass the filter or when the distribution of the invaded cells is uneven. (6) The counting of the cells is time-consuming. Even though some automated cell counters exist, they are not reliable, as they do not always discern the difference between a cell and a pore (Hulkower and Herber, 2011).

Spheroid Sprouting Assay: The spheroid sprouting assay studies the invasion of cells from three-dimensional tumour spheroids embedded in ECM. Cancer cell invasion is quantified by the distance travelled by single cells into the surrounding matrix (Blacher et al., 2014) (**Illustration 6**).

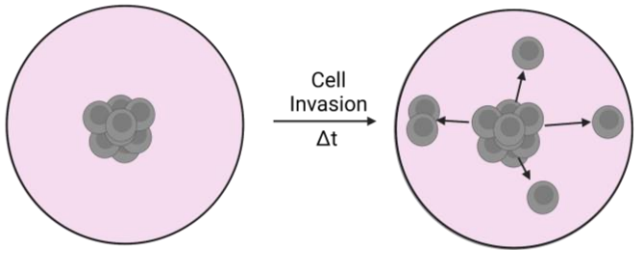

Illustration 6: Spheroid Sprouting Assay
Schematic representation of the spheroid sprouting assay. Illustration created with BioRender.com

The Spheroid Sprouting Assay provides numerous advantages: (1) It mimics well the *in vivo* environment as it considers three-dimensional cell-cell interactions. (2) It represents an easy and rapid method to measure cancer cell invasion. (3) Invasion can be studied on different matrices as the surface can be coated with an ECM of choice. (4) The movement and morphology of the cells can be visualized at any moment of the experiment (Blacher et al., 2014). Yet, some drawbacks of this experiment are: (1) Not all cell lines can form spheroids. (2) The analysis of the cell velocity is time taking as cells invade in every direction.

Organotypic Cell Invasion: To mimic the important characteristics of the tumour microenvironment (TME), cancer cell invasion can be monitored in *ex vivo* tissue slices. For example, GBM cell invasion can be monitored in mouse brain slices. Thin brain slices remain viable and tissue architecture can be maintained for up to 10 days if the slices are cultured in an appropriate medium. Fluorescent-labelled tumour cells can be injected and single-cell movements can be monitored over time using a live imager (**Illustration 7**). The cancer cell velocity informs on the dissemination capacity of the monitored cancer cell.

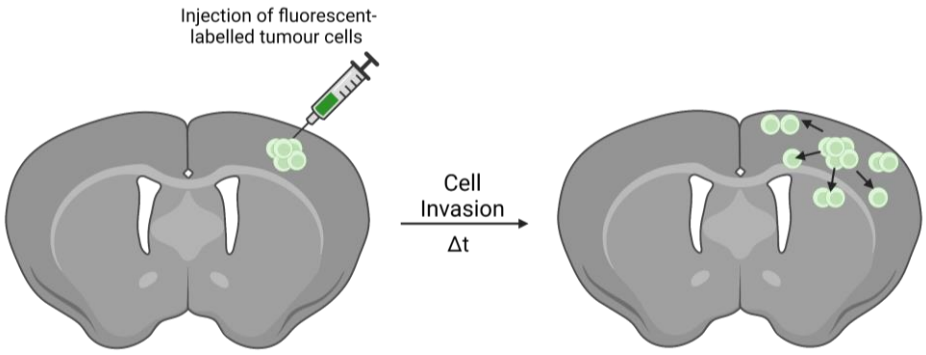

Illustration 7: *Ex Vivo* Brain Slice Culture
Schematic representation of an *ex vivo* brain slice culture. Illustration created with BioRender.com

Being an *ex vivo* system, this experiment is the best procedure to recapitulate invasion in the TME without the need for an animal protocol. Yet, this experiment requires animal sacrifice, special equipment, and technical expertise.

While major advances have been made to develop three-dimensional *in vitro* cultures or *ex vivo* assays to investigate invasion, these systems only allow for the investigation of a specific step of the metastatic cascade. Moreover, some aspects of metastasis, including the role of the immune system, are not taken into account *in vitro* and *ex vivo*. This is why animal models remain indispensable to study the full metastatic cascade.

Tail Vein Injection: In the tail vein injection assay, cancer cells are injected into the bloodstream of a mouse to study the extravasation and the colonisation step of the metastatic cascade. Cancer cells are maintained in a tissue culture before being dissociated into single cells, counted, and finally injected into the tail vein of a mouse (**Illustration 8**). After a predefined incubation time, the animals are sacrificed and the metastases are counted (Elkin and Vlodavsky, 2001).

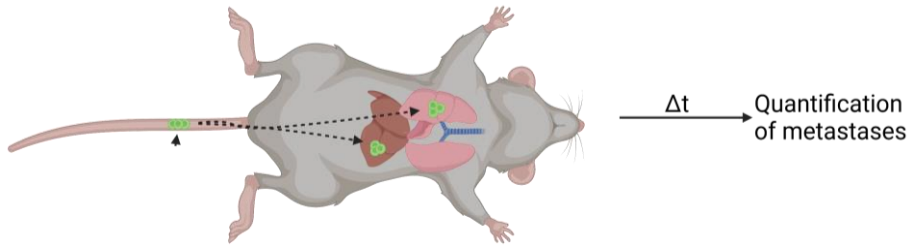

Illustration 8: Tail Vein Injection
Schematic representation of an *in vivo* tail vein injection. Illustration created with BioRender.com

The tail vein injection assay represents an easy and rapid method to measure the seeding capacity of cells. The main advantage of this assay is that it is independent of primary tumour growth and thus less variable. Yet, by enforcing metastasis without a primary tumour, the tail vein injection assay (1) ignores the intravasation processes and (2) does not account for possible primary tumour-metastasis interactions.

Orthotopic Implantation: Orthotopic implantation implies the direct injection of tumour cells into the corresponding tissue in a mouse. For example, breast cancer cells can be injected into the mammary fat pad of a mouse (**Illustration 9**). This experimental model allows studying the primary tumour development and subsequent metastasis formation in a physiologically relevant environment.

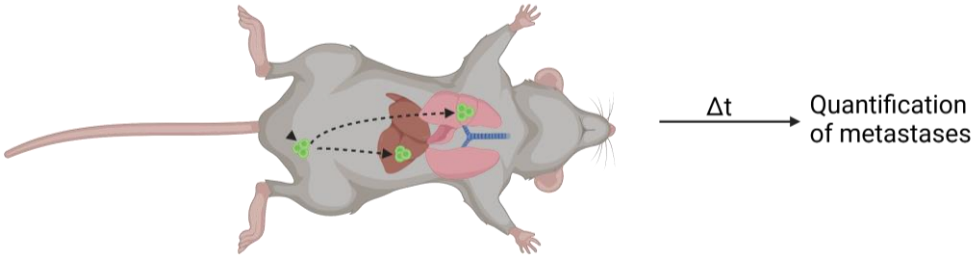

Illustration 9: Orthotopic Implantation
Schematic representation of a breast orthotopic mouse model. Illustration created with BioRender.com

(1) The orthotopic implantation model simulates the progression of cancer cells from the primary tumour to metastasis. (2) This model also allows for the investigation of primary tumour-metastasis interaction. Yet, this experiment is not always successful as not all cancer cells metastasize easily.

Genetically engineered mouse models (GEMMs): GEMMs are mice which were genetically altered to spontaneously form tumours (Kersten et al., 2017). These models provide a valuable tool: (1) To study complex processes such as cancer initiation, organ-specific metastasis formation and the involvement of the TME. (2) These models also allow for the investigation of the tumour development in fully immune-competent mice.
Nowadays a large collection of GEMMs imitating the most common cancer types can be purchased. However, a severe drawback of this model is that the mice develop the diseases at different, unpredictable stages. The heterogeneity in the frequency, latency and cancer growth, makes the experiment complex and costly (Kersten et al., 2017).

3. Cancer Metabolism

Already in the late 1920s, Otto Warburg identified metabolic rewiring as an important step of cancer cell adaptation that promotes tumorigenesis. He reported that highly proliferative cancer cells are characterized by a high glucose consumption and a high lactate release rate regardless of the cellular oxygen levels (Warburg et al., 1927). Warburg proposed that such enhanced aerobic glycolysis is caused by a mitochondrial dysfunction and that it is the primary cause of cancer (Warburg, 1956). Today we know that mitochondria are functional and very important for tumour progression. Despite intense studies over the last 100 years, the definite function of the “Warburg Effect” remains debated.

Although more than a century ago, altered metabolism has been identified to support cancer progression, it was not included in the initial hallmarks of cancer (Hanahan and Weinberg, 2000). Boosted by modern biochemical and molecular biological tools, cancer metabolism gained increasing interest over the last years which led to advances in the understanding of the mechanisms that derive tumorigenesis.

It became evident that cancer cells hijack metabolic pathways (1) to increase nutrient availability, (2) to support tumorigenic properties, and (3) to enforce changes in the cells’ behaviour/function (Pavlova and Thompson, 2016).

As metabolic alterations have been observed in a large variety of cancer types, a reprogrammed metabolism was included in the updated version of the hallmarks of cancer in 2011 (Hanahan and Weinberg, 2011).

Despite the heterogeneity of tumours, cancer cell metabolism seemed to involve a finite set of metabolic pathways that support core functions like (1) biosynthesis, (2) energy production, and (3) Redox balance (Cantor and Sabatini, 2012).

Biosynthesis: Macromolecules are synthesized through anabolism. Anabolism is the set of metabolic pathways by which energy is used to synthesise complex molecules such as proteins, DNA/RNA, lipids and sugars.

Energy production: Energy is produced through catabolism, which is the set of metabolic pathways by which molecules, such as amino acids, fatty acids and sugars are oxidized to generate energy in form of adenosine triphosphate (ATP).

Redox Balance: Redox metabolism is the set of metabolic pathways by which the oxidation state of a substrate changes. More precisely, in a Redox reaction, electrons are transferred from a reductant (electron donor) to an oxidant (electron acceptor). Within the cell, the majority of Redox reactions are endothermic and require specific enzymatic catalysts known as oxidoreductases as well as corresponding Redox cofactors. The most common Redox cofactors are the pyridine nucleotides NAD and NADP, which in their oxidized form (NAD^+ and $NADP^+$) act as electron acceptors and in their reduced form (NADH and NADPH) act as electron donors.

It is commonly believed that tumour cells can reprogram their metabolism to improve cellular fitness and provide a selective advantage during tumorigenesis. A flexible metabolic conversion allows cancer cells to dynamically set up their metabolic pathways to support their current metabolic needs along the metastatic cascade formed by the three pillars: (1) biosynthesis, (2) energy production, and (3) Redox balance (Benzarti et al., 2020; DeBerardinis and Chandel, 2016) (**Illustration 10**).

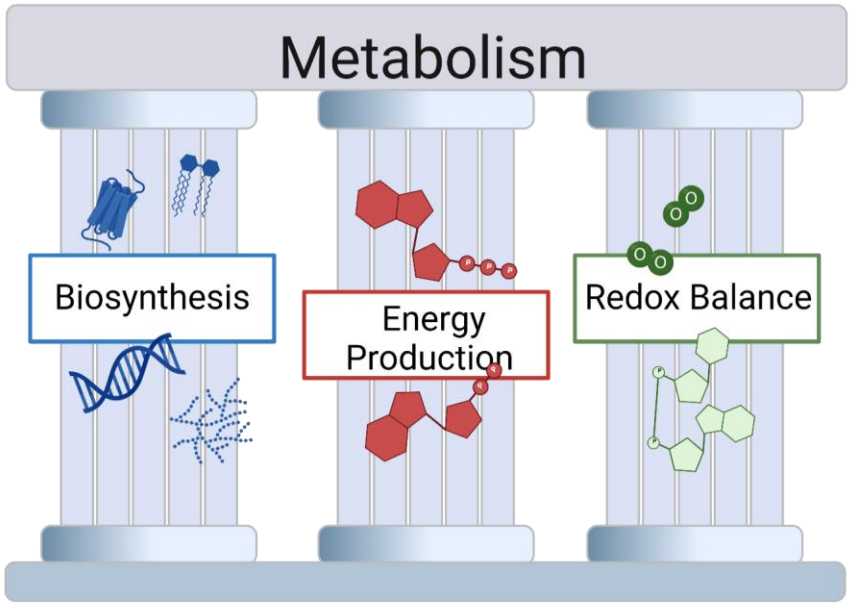

Illustration 10: The Three Metabolic Pillars
Cancer cells can switch their metabolism to better support anabolism, catabolism, or Redox balance. Edited from (https://cancercommunity.nature.com/posts/mitochondrial-one-carbon-metabolism-as-a-driver-of-migration) and created with BioRender.com

3.1 Three fundamental metabolites in cancer

Glucose: Glucose is simultaneously the most abundant nutrient in the blood and the main contributor to mammalian cell metabolism. In the resting state, cells first catabolise glucose into pyruvate by glycolysis, and then pyruvate is further metabolized through the tricarboxylic acid cycle (TCA). The chemical energy of pyruvate released during full oxidation is used to ultimately synthesize ATP, which can release this energy upon hydrolysis of the phosphate group(s). All cells use glucose to support energy synthesis, yet cancer cells differ in the way they utilize glucose. As highlighted by Otto Warburg, cancer cells are characterised by aerobic glycolysis (Warburg et al., 1927). Cancer cells convert glucose into lactate in the presence of O_2 and fully functioning mitochondria. The catabolism of 1 mol glucose to lactate yields little energy as it only generates 2 mol ATP per molecule of glucose, whereas oxidative phosphorylation generates up to 36 mol ATP upon complete oxidation of 1 mol glucose. The definite function of the “Warburg Effect” remains debated, yet the most established assumption conjectures that high glycolysis allows the synthesis of intermediate metabolites to support anabolic processes (Vander Heiden et al., 2009).

Recent research even states that cells transform glucose to lactate, only when glycolysis-derived NADH saturates the mitochondrial NADH shuttle (Wang et al., 2022).
High proliferation imposes a large requirement for nucleotides, amino acids, and lipids. Many intermediates in glycolysis support the needed requirement: Pyruvate contributes to acetyl-CoA synthesis, a precursor of fatty acid, cholesterol and lipid synthesis. Furthermore, pyruvate is also needed to synthesise different non-essential amino acids (aa) such as aspartate and asparagine. Additionally, Glucose-6-Phosphate (G6P) is the rate-limiting enzyme in the pentose phosphate pathway (PPP), which generates the ribose group required for nucleotide synthesis. The PPP also plays an important role in the Redox balance as it is the major pathway for NADPH synthesis. Finally, 3-phosphoglycerate (3PG) an intermediate of glycolysis, is also the branching point for serine synthesis (**Illustration 11**). Overall, cancer cells use the catabolism of glucose through aerobic glycolysis to generate energy, biosynthetic precursors and NADPH.
In addition to increased glucose uptake, cancer cells also increase their uptake of other metabolites to support tumorigenesis.

Glutamine: Glutamine (Gln) mostly represents the second most consumed nutrient after glucose in cancer cells. Usually, its consumption exceeds its biosynthetic demand (Jain et al., 2012). Entering glutamine is, in many cancer cells, deamidated and exported out of the cell as glutamate (Bannai and Ishii, 1988; Jain et al., 2012; Timmerman et al., 2013). The export of glutamate through the xCT antiporter is coupled with cysteine import (Bannai and Ishii, 1988; Timmerman et al., 2013). The antiporter xCT was identified to positively correlate with cancer malignancy in glioma and breast cancer patients (Robert et al., 2015; Timmerman et al., 2013). In case glutamate is not exported out of the cell, glutamate is either used to generate glutathione (GSH), an important cellular antioxidant, or it is converted into α-ketoglutarate (αKG), which can be oxidized in the TCA cycle. The synthesis of citrate from αKG through the reductive TCA cycle was identified to facilitate the proliferation of cancer cells with defects in the electron transport chain (ETC) (Metallo et al., 2011; Mullen et al., 2011). An additional role of glutamine is to provide nitrogen for nucleotide synthesis (**Illustration 11**). Although glutamine plays a crucial role in the central carbon metabolism, the nitrogen metabolism, and multiple signalling pathways, clinical trials targeting the glutamine metabolism did not yield satisfying results yet.

Serine: Serine represents the third most consumed metabolite in many cancer cells (Hosios et al., 2016). Being a non-essential aa, the cell can either take up serine through specific membrane transporters or *de novo* synthesise it from the glycolytic intermediate 3PG using the intracellular serine synthesis pathway (SSP).

The importance of serine metabolism in cancer development was discovered in the 1980s, when researchers recorded SSP upregulation in different cancer types (Snell, 1985; Snell et al., 1988).

These findings are supported by recent experiments which identified SSP gene upregulation (including phosphoglycerate dehydrogenase (PHGDH)) in a wide spectrum of cancer types including breast, melanoma, and lung cancer (Amelio et al., 2014; Locasale et al., 2011; Pollari et al., 2011; Possemato et al., 2011; Zhang et al., 2017). Indeed, SSP gene upregulation in lung cancer patients negatively correlates with patient survival (Zhang et al., 2017). Additionally, cancer cell proliferation in xenograft and allograft models was significantly reduced during a serine-deficient diet (Maddocks et al., 2013; Maddocks et al., 2016; Maddocks et al., 2017).

The serine-dependent biosynthesis of various molecules supports the proliferation of cancer cells. More precisely, serine is a precursor of the non-essential amino acids glycine and cysteine. Glycine, in turn, is directly incorporated into purine nucleotide bases and GSH. Furthermore, serine is necessary for the synthesis of sphingolipids (SL) via the synthesis of spingosine and serine supplies carbon to the one-carbon (1C) metabolism (Mattaini et al., 2016; Tedeschi et al., 2013). The 1C metabolism generates precursors for anabolic sinks including thymidine monophosphate (dTMP), purines, Redox equivalents, and ATP (Benzarti et al., 2020) (**Illustration 11**).

Taken together, metabolism supports cancer cell progression by generating building blocks (including proteins, nucleotides, and lipids), energy and reducing equivalents to support cancer proliferation, dissemination and survival.

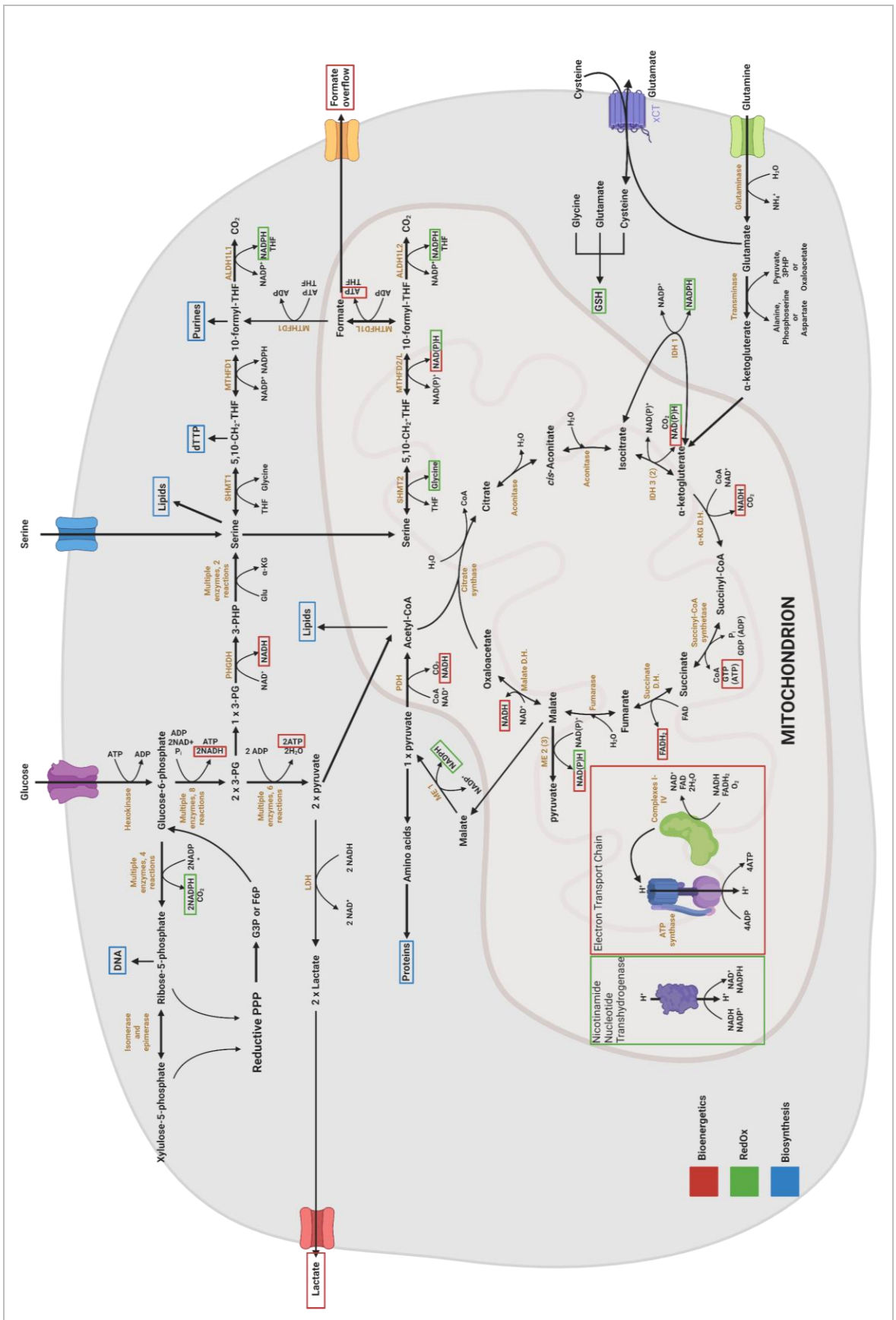

Illustration 11: Central Carbon Metabolism

The fate of available carbon sources within cancer cells according to different metabolic sinks. Glucose, serine, and glutamine are utilised in various pathways to generate co-factors and intermediates that the cell then utilises for biosynthesis (blue), bioenergetics (red) or Redox balance (green). Illustration adapted from (Benzarti et al., 2020) and created with BioRender.com.

3.2 Metabolic Profiling

The interconnection between the different metabolic pathways presents a special challenge in the study of cancer cell metabolism. Two main methods are currently used to detect and quantify metabolites: (1) nuclear magnetic resonance (NMR) and (2) mass spectrometry (MS). The strengths of NMR are precise quantification and superior compound identification; however, the main disadvantage of this method is its low sensitivity (metabolite concentration must exceed 1 µM). In comparison, MS is characterised to be highly sensitive as it can detect metabolites in the femtomolar range. Coupled either with liquid chromatography (LC), ion chromatography (IC) or gas chromatography (GC), MS can detect hundreds of compounds in one single run, making it a powerful and high-throughput technique. Three distinct MS approaches have been established over the last years to study different aspects of cellular metabolism: (1) Steady-State Levels, (2) Consumption and Release Rate, and (3) Flux Analysis.

***Steady-State Levels*:** This analytical method informs about the intracellular metabolite level at the dynamic equilibrium. Mass spectrometry-based quantification represents a powerful tool for gaining insights into metabolomics. Yet, the signal intensity depends on the ionization efficiency and therefore does not reliably reflect absolute concentrations.
This limitation can be overcome by using internal and external standards. Absolute quantification is obtained through a calibration curve allowing to determine the unknown concentration of a compound by applying a fit and interpolation. Absolute levels allow (1) to compare diverse metabolites with each other, (2) to contrast the level of a specific metabolite at different times and (3) to study the kinetics of a specific enzyme. Although absolute metabolite concentrations provide additional information, this method is very time-consuming. Accordingly, as the key objective of metabolite analyses lies in detecting changes in response to perturbations, relative quantification is often sufficient. Relative levels are semi-quantitative, meaning that the metabolite spectral patterns and intensities are measured and statistically compared between the different biological conditions (Kapoore and Vaidyanathan, 2016). Hence, relative levels allow to relatively compare one specific metabolite between the different experimental conditions, but cannot be employed to compare levels of different metabolites against each other.

***Consumption and Release Rate (CORE)*:** CORE, is an analytical method that profiles the dynamic changes between the intracellular and the extracellular metabolome (Buescher et al., 2015). Measuring the extracellular metabolites at two distinct time points (at the beginning and the end of the experiment), CORE informs about the cellular metabolic activity over a defined time span. For instance, measuring the rate of glucose depletion in a cell culture medium informs on the glucose consumption of the cells.

CORE measurements are used to study non-essential aa such as serine. As the cell can either take up serine through specific membrane transporters or *de novo* synthesise it from glucose, both sources have to be monitored. Serine uptake can be studied through CORE measurements and serine production by a flux analysis.

Flux Analysis: Quantification of metabolite concentration alone is insufficient to understand the dynamic nature of the metabolic network. Indeed, as a single metabolite can be involved in different metabolic pathways, the concentration itself does not provide sufficient information. For example, an increase in metabolite concentration can be explained by an increased production or a decreased consumption of the specific metabolite. To examine intracellular fluxes, metabolic tracers are commonly used. A labelled metabolic tracer is a molecule that is chemically and functionally identical to the naturally occurring metabolite, but in which one or more atoms are replaced with an isotope of the same element. As isotopes differ in the number of neutrons only, a metabolic tracer differs in its mass from its natural equivalent. Depending on the auxiliary number of neutrons inside its nucleus, an isotope may be stable or radioactive.

In metabolomics research, the most commonly used stable isotopes include deuterium (^{2}H), carbon (^{13}C), and nitrogen (^{15}N), as their non-labelled counterpart build the organic molecules that are metabolised by mammalian cells. Such tracer metabolites containing stable isotopes can be fed to cells and will be metabolised identically as the non-labelled metabolites. Isotope enrichment into downstream metabolites of interest can be determined by MS based on the mass increase and thereby inform about pathway activity. When a ^{13}C labelled isotopic tracer is added to cells, this labelled substrate will be metabolized along its specific metabolic pathway. The thereby generated downstream metabolites will become increasingly enriched over time for ^{13}C, informing about relative pathway activities, qualitative changes in the pathway contributions via alternative metabolic routes, and nutrient contribution to the production of different metabolites (**Illustration 12**). At isotopic steady-state, equilibrium is reached and ^{13}C incorporation remains unchanged over time.

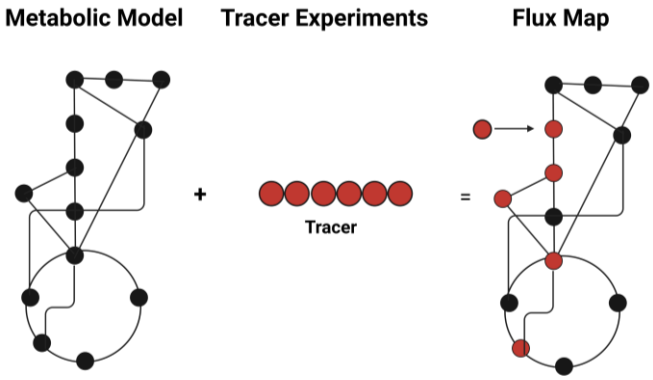

Illustration 12: Metabolic Flux Analysis
Using metabolic models and isotopic tracer experiments, the dynamic nature of metabolism can be studied. Adapted from (Antoniewicz, 2021) and created with BioRender.com.

A mass isotopomer distribution (MID) informs about the fractional enrichment of a metabolite of interest (Buescher et al., 2015). The fractional enrichment of a metabolite represents the abundance of a particular isotopologue among all the measured isotopologues of that metabolite. The resulting distribution informs on (1) the substrate contribution, and (2) the relative activity of the implicated metabolic pathways (Buescher et al., 2015).

Although isotopic tracers generate substrate- and pathway-specific labelling patterns, the results are very difficult to decipher. Due to the high complexity and dynamic of the metabolic network, the results are ambiguous and have to be verified by supplementary experiments (Hiller et al., 2011; Keibler et al., 2012).

The MID alone does not provide any information about the position of the isotopic atom within the metabolite (**Illustration 13**). Information about the positional labelling can be obtained by tandem MS (MS/MS). In principle, in MS/MS a metabolite of interest is isolated based on its mass and subsequently, the metabolite is fragmented by collision. Each fragment's mass is then measured in a second step. The labelled position can then be determined by recombining the different pieces of the fragmentation (Tepper and Shlomi, 2015).

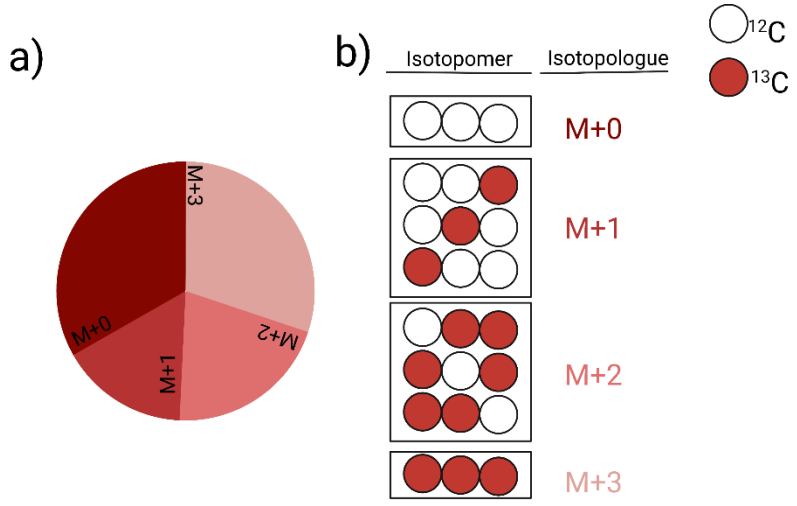

Illustration 13: Mass Isotopomer Distribution
a) MIDs indicate the distribution of the isotopologues b) but it does not provide any information about the position of the isotope within the metabolite. Adapted from (Buescher et al., 2015) and created with BioRender.com.

The development and application of new metabolic methods not only permitted scientists to reveal the heterogeneity and plasticity of tumours but also revealed new metabolic pathways that are important to support tumour growth and metastasis. One pathway that gained importance over the last year is the One-Carbon (1C) metabolism.

4. One-Carbon Metabolism

The 1C metabolism is a highly compartmentalized metabolic pathway, which catabolises multiple carbon sources to derive 1C units and metabolic by-products to be used in fundamental cellular functions (Ducker and Rabinowitz, 2017) such as biosynthesis, methylation, and Redox reactions.

Although serine as well as glycine can function as 1C donors in the 1C metabolism (Kalhan and Hanson, 2012; Yang and Vousden, 2016), serine, a non-essential aa, was identified as the major 1C source in most organisms, including humans (Fan et al., 2014; Labuschagne et al., 2014). Several scientific reports highlighted that in the presence of serine, glycine is not even consumed by the cells (Labuschagne et al., 2014; Maddocks et al., 2013; Meiser et al., 2016).

The 1C cycle is composed of two complementary pathways, one of which is localised in the cytosol and the other in the mitochondria (**Illustration 14**) (Tibbetts and Appling, 2010).

In the mitochondria, serine hydroxymethyltransferase 2 (SHMT2) starts the cycle by generating 5,10-methylene-THF (5,10-CH_2-THF) and glycine from serine and tetrahydrofolate (THF). Then, the bifunctional enzyme methylene-THF dehydrogenase 2 (MTHFD2) oxidizes 5,10-CH_2-THF to 10-CHO-THF in two steps. First, 5,10-CH_2-THF is oxidized to 5,10-CH_2=THF using either NAD^+ or $NADP^+$. Subsequently, 5,10-CH_2=THF is hydrolysed to 10-formyl-THF (10-CHO-THF). Remarkably, two isoforms of methylene-THF dehydrogenase were identified in the mitochondria: MTHFD2 and MTHFD2 like (MTHFD2L). Whereas MTHFD2 is expressed mainly in embryos, tumours, and undifferentiated tissues (Mejia and MacKenzie, 1985), MTHFD2L is more widely expressed in differentiated cells (Bolusani et al., 2011). Recent experiments identified that both enzymes can process NAD^+ as well as $NADP^+$ as co-factors (Shin et al., 2017).

Mitochondrial 10-CHO-THF can then either be used as a substrate of methylene-THF dehydrogenase 1-like (MTHFD1L) to produce formate and ATP, or it can be further oxidized to CO_2 and THF in an $NADP^+$-dependent manner by the mitochondrial folate enzyme aldehyde dehydrogenase 1 family member L2 (ALDH1L2) (**Illustration 14**).

In the cytosol, the trifunctional enzyme methylene-THF dehydrogenase 1 (MTHFD1) catalyses both: the ATP-dependent synthesis of 10-formyl-THF (10-CHO-THF) from THF and formate, and the two-step conversion of 10-CHO-THF to 5,10-CH_2-THF. Finally, SHMT1 converts 5,10-methylene-THF and glycine back to serine and THF.

All of the resulting biochemical reactions involve the 1C acceptor THF, which originates from folic acid. To be precise, folic acid is reduced to THF by the enzyme dihydrofolate reductase (DHFR) using two molecules of NADPH. Whereas most bacteria, yeast, and plants can generate folate molecules on their own, animals, including humans, do not and require dietary folate intake, for example by eating leafy green vegetables (Rossi et al., 2011).

Albeit most reactions in the 1C metabolism are reversible, 75% of the 1C units for cytoplasmic processes derive from the mitochondrial pathway (Pike et al., 2010). This justifies the chemical reaction succession described in the above paragraph. Such directionality of the 1C cycle may be explained by the high NAD^+/NADH ratio in the mitochondria favouring serine oxidation to formate, and the low $NADP^+$/NADPH ratio in the cytosol favouring the inverse reaction. However, the thermodynamically favourable reactions performed by cytosolic SHMT1 and MTHFD1 can be reverted to meet the 1C demand when the mitochondrial pathway is defective (Ducker et al., 2016).

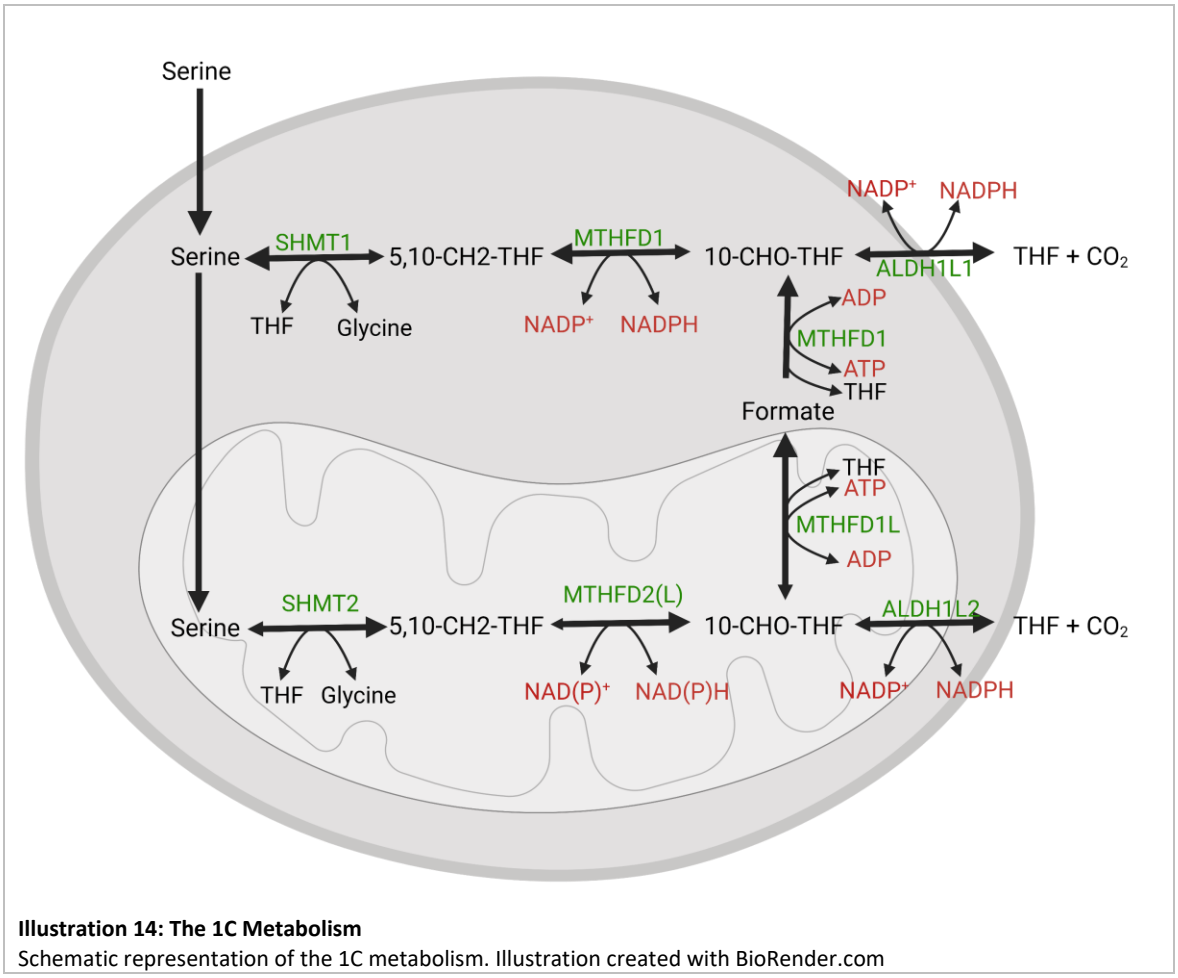

Illustration 14: The 1C Metabolism
Schematic representation of the 1C metabolism. Illustration created with BioRender.com

4.1 Transport Processes

Although the 1C cycle is physically divided into a cytoplasmic and a mitochondrial part, both compartments are metabolically connected as THF, serine, glycine, and formate can be transported via specific transporters across the mitochondrial membrane to support the 1C cycle (Tibbetts and Appling, 2010).

***Mitochondrial Folate Transporter (MFT)*:** Administration of labelled folic acid revealed a rapid increase of labelled folates into the mitochondria, suggesting the existence of a specific MFT (Cook and Blair, 1979). SLC25A32, a member of the solute carrier 25 family of mitochondrial transporter was identified to transport THF across the mitochondrial membrane (Titus and Moran, 2000). Cells lacking this protein were characterized by glycine deficiency, a common phenotype of mitochondrial folate pathway loss (Titus and Moran, 2000). The transport of folate through the MFT is governed by the number of glutamates attached to the folate molecule. Polyglutamated folates are poor substrates for folate transport systems, whereby these folates are usually restricted to the intracellular compartment. In the mitochondrion, the folylpolyglutamate synthetase (FPGS) adds polyglutamate tails to mitochondrial folates capturing so the folate to this organelle (Lin and Shane, 1994; Tibbetts and Appling, 2010).

Mitochondrial Serine Transporter: The mitochondrial serine transporter sideroflexin 1 (SFXN1) was found to be involved in the 1C metabolism. Cells lacking the *SFXN1* gene were shown to be defective in glycine and purine synthesis (Kory et al., 2018). Furthermore, serine transport by purified SFXN1 proteins was verified *in vitro* (Kory et al., 2018).

Mitochondrial Glycine Transporter: Although some mitochondrial glycine transporters are described in the literature, no specific transporter has been linked to the 1C metabolism (Tibbetts and Appling, 2010).

Mitochondrial Formate Transporter: The transport of formate through the mitochondrial membrane is of the highest importance to supply the cytosolic part of the 1C cycle. Due to their hydrophilic nature, every 10-CHO-THF must first be converted to formate before being transported to the cytoplasm to support nucleotide production (Tibbetts and Appling, 2010). Given the negative charge of formate, it is assumed that formate does not simply cross the mitochondrial membrane through passive transport (Nicholls, 1975). However, no formate-specific mitochondrial transporter has been identified to date.

4.2 One-Carbon Metabolism and Cancer

The 1C metabolism supports a variety of different physiological processes (Benzarti et al., 2020): (1) biosynthetic processes such as nucleotide synthesis (purine and thymidine) (Tedeschi et al., 2013) and aa homeostasis (serine and glycine), (2) epigenetic processes such as methylation (Young et al., 2017), (3) bioenergetic processes such as ATP synthesis (Maddocks et al., 2016; Meiser et al., 2016; Tedeschi et al., 2013), and (4) Redox balance (Maddocks et al., 2016; Meiser et al., 2016; Tedeschi et al., 2013) (**Illustration 15**).

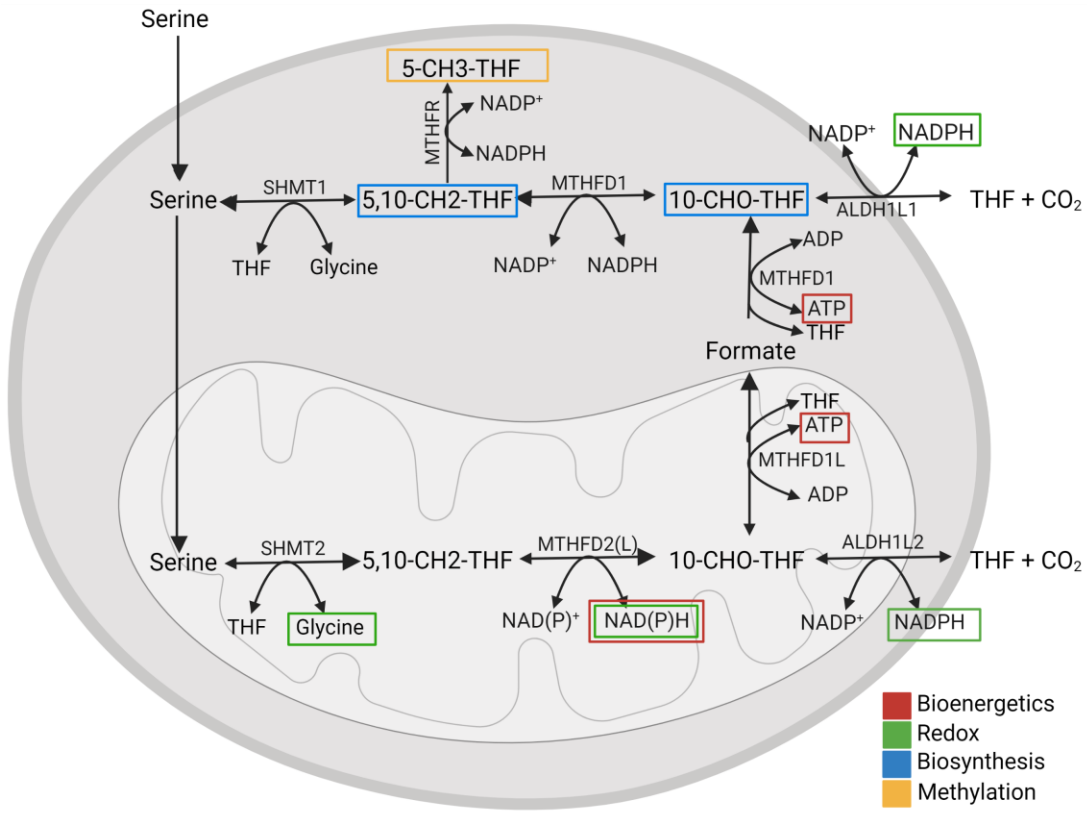

Illustration 15: Outputs of the 1C Metabolism
The 1C metabolism mediates the redistribution of 1C units from various nutrients into purine and thymidine synthesis, homocysteine remethylation, glutathione synthesis, and ATP and NADPH homeostasis. Illustration created with BioRender.com

The implication of 1C unit synthesis in cancer was observed for the first time more than 70 years ago. In 1947, 4-aminopteroyl-glutamic acid (aminopterin), a folic acid antagonist, was administered by intramuscular injection to 16 children suffering from acute leukaemia. 10 out of 16 patients presented a temporary remission after the treatment (Farber and Diamond, 1948). This clinical trial led to the development of several antifolates, including methotrexate (Mtx) (Osborn et al., 1958) the most well-known antifolate treatment in cancer, that is still in medical use today.

The implication of the 1C metabolism in cancer was also explicitly underlined. *SHMT2* and *MTHFD2* were identified among the most overexpressed metabolic genes in cancer patients when compared to healthy individuals (Jain et al., 2012; Nilsson et al., 2014). The mitochondrial enzymes of the 1C metabolism were identified to promote cancer cell proliferation and tumorigenesis (Jain et al., 2012; Ye et al., 2014). Furthermore, overexpression of *SHMT2* or *MTHFD2* correlates with a low survival rate for multiple cancer types including breast cancer, non-small cell lung cancer, pancreatic cancer, gliomas, and cholangiocarcinoma (DeNicola et al., 2015; Nilsson et al., 2014; Ning et al., 2018; Noguchi et al., 2018; Wu et al., 2017; Yin, 2015; Zhang et al., 2016).

4.3 The Relevance of the 1C Metabolism

4.3.1 Relevance of the 1C Metabolism in Biosynthesis

The most important difference between normal cells and cancer cells is the uncontrolled cell proliferation. This implies that cancer cells must rewire their metabolism to support the increased synthesis of biomass from the available nutrients. The 1C metabolism support cell proliferation through (1) purine and (2) thymidylate synthesis.

***Purine synthesis*:** In proliferating mammalian cells, purine synthesis has the highest demand for cytoplasmic 1C units (Ron Milo, 2015). Purines are synthesised in an 11-step process incorporating CO_2, glycine, 2 molecules of formate, glutamine, and TCA cycle-derived aspartate (Ducker and Rabinowitz, 2017) (**Illustration 16**).

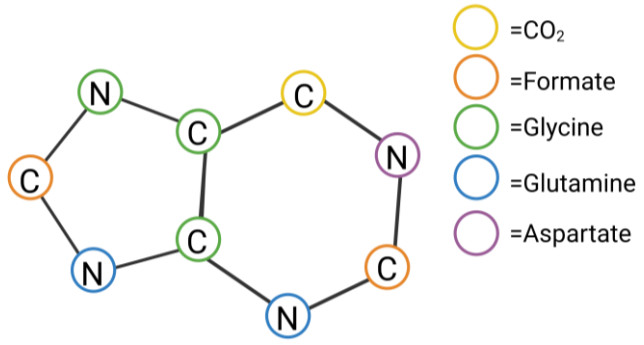

Illustration 16: Purine Molecule
Schematic representation of a purine molecule. Illustration created with BioRender.com

Thymidylate synthesis: Thymidylate synthase (TYMS) converts deoxyuridine monophosphate (dUMP) into deoxythymidine monophosphate (dTMP) in a 5,10-methylene-THF-dependent reaction (Ducker and Rabinowitz, 2017). The 1C metabolism provides the 1C units required for thymidylate synthesis. In absence of dTMP synthesis due to folate deficiency, uracil is wrongly incorporated into the DNA causing chromosome breaks (Blount et al., 1997; Goulian et al., 1980).

Thus, the 1C metabolism provides the cancer cell with the necessary nucleotides to support cancer cell progression and tumorigenesis (Yin et al., 2018) (**Illustration 17**). Targeting nucleotide synthesis has been proven to be an effective treatment to stop DNA replication and to cause apoptosis by DNA damage. Mtx exerts deleterious effects on cancer cells by nucleotide synthesis inhibition (Allegra et al., 1987; Bruce-Gregorios et al., 1991; Yin et al., 2018).

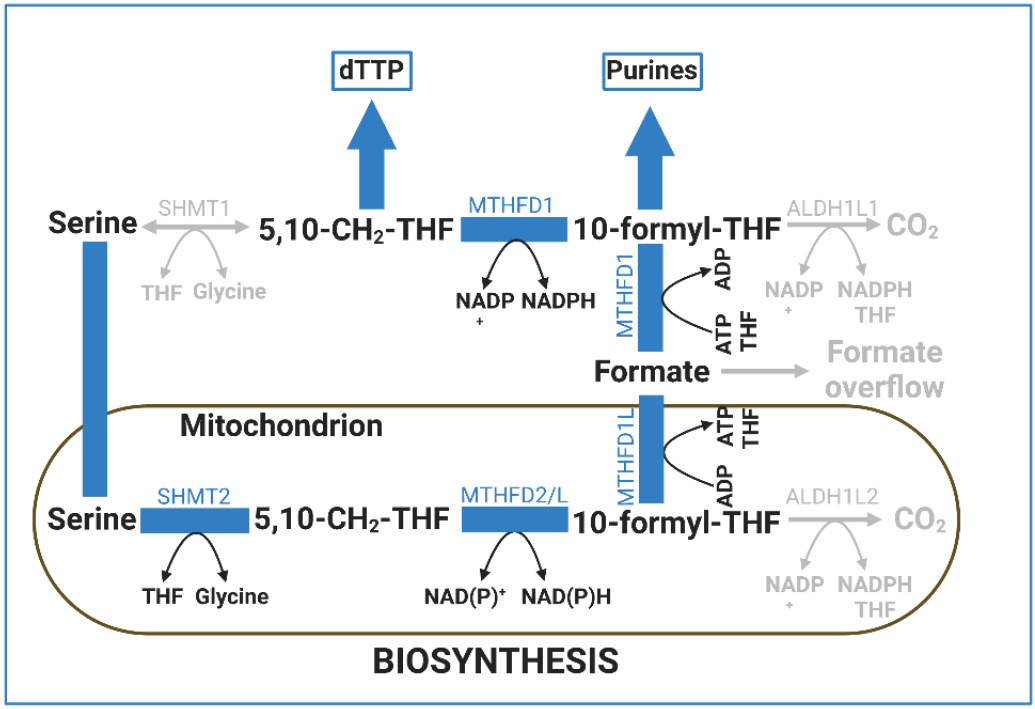

Illustration 17: Relevance of the 1C Metabolism in Biosynthesis
Illustration adapted from (Benzarti et al., 2020) and created with BioRender.com.

The 1C metabolism not only supports cancer cell proliferation by providing sufficient nucleotides but also generates energy, provides methyl groups, and is important for the cellular Redox balance of the cells.

4.3.2 Relevance of the 1C Metabolism in Bioenergetics

The 1C metabolism was also hypothesised to support energy synthesis (Tedeschi et al., 2013). Using metabolic flux analysis it was discovered that the rate of formate production in cancer cells is often higher than the anabolic 1C demand for nucleotide synthesis. Excess formate and glycine is excreted into the extracellular medium (Meiser et al., 2016). Comparable to the uncompleted catabolism of glucose into lactate, the uncompleted catabolism of serine into glycine and formate goes along with the net production of ATP (Meiser et al., 2016). At a biochemical level, every released formate molecule equals a net production of 3.5 ATP (**Illustration 18**). One adenosine diphosphate (ADP) is phosphorylated to ATP by MTHFD1L and the produced NADH by MTHFD2(L), can be oxidized by complex I in the ETC, which then produces an additional 2.5 molecules of ATP (Meiser et al., 2018). It was observed in different cancer models, that under nutrient stress conditions, where glycolysis is limited and cell growth is arrested, serine catabolism and formate overflow increases (Meiser et al., 2016). In these conditions, the cancer cells can rewire the 1C metabolism to generate energy (Benzarti et al., 2020).

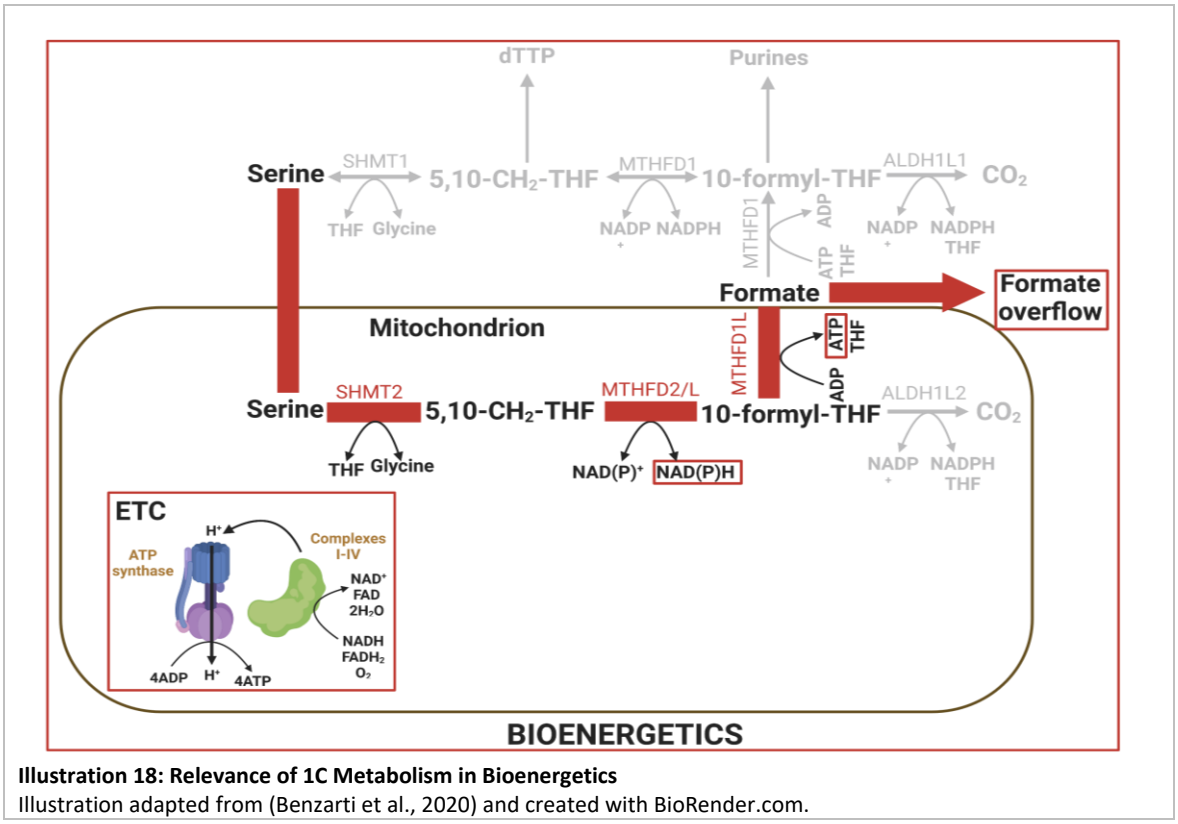

Illustration 18: Relevance of 1C Metabolism in Bioenergetics
Illustration adapted from (Benzarti et al., 2020) and created with BioRender.com.

4.3.3 Relevance of the 1C Metabolism in Methylation

It has been shown that cancer cells present an altered methylation pattern on RNA/DNA. For illustration, hyper-methylation of tumour-suppressor genes is commonly detected in cancer cells and favours their survival (Kulis and Esteller, 2010). An important substrate of the methylation process is S-Adenosyl methionine (SAM). SAM is generated by methionine adenosyltransferase through the addition of ATP to methionine. Upon transfer of its methyl group to an acceptor, SAM becomes S-adenosylhomocysteine, which in turn, is rapidly converted to homocysteine. Homocysteine is then re-methylated into methionine using one molecule of 5-methyl-THF (Yang and Vousden, 2016).

The 1C metabolism plays a dual role in the process of methylation. (1) It provides 5,10-CH_2-THF, which is transformed by methylene tetrahydrofolate reductase (MTHFR) into 5-methyl-THF, the substrate for homocysteine re-methylation. (2) The 1C metabolism provides the required ATP for SAM synthesis (Maddocks et al., 2016).

Surprisingly, independent experiments underlined that the 5,10-CH_2-THF supply plays only a minor role in the re-methylation process (Bhatia et al., 2020; Maddocks et al., 2016). Indeed, it was shown that the major contribution of the 1C metabolism in the methylation process is through the *de novo* synthesis of ATP (Maddocks et al., 2016). For example, serine starvation was shown to decrease the methylation ratio of DNA and RNA, as well as the ATP levels in CRC cells (Kottakis et al., 2016) (**Illustration 19**).

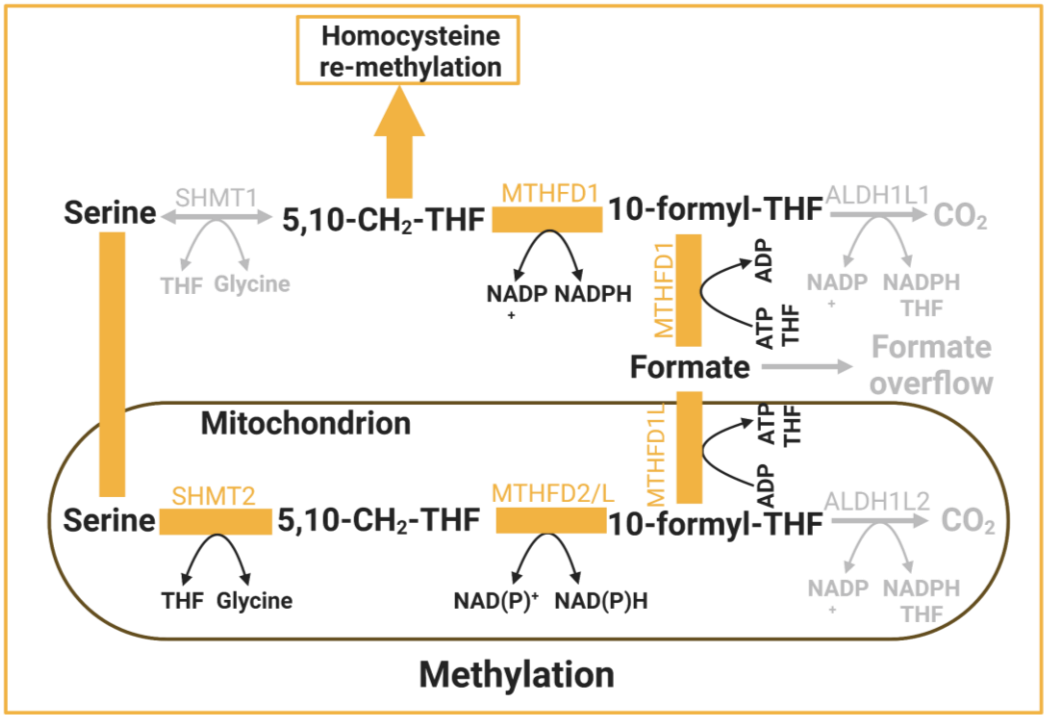

Illustration 19: Relevance of 1C Metabolism in Methylation
Illustration adapted from (Benzarti et al., 2020) and created with BioRender.com.

4.3.4 Relevance of the 1C Metabolism in Redox Balance

Glutathione (GSH), the most important antioxidant synthesized in the cell, is a tripeptide composed of glutamate, cysteine, and a molecule of glycine. The antioxidant mechanism of glutathione is a Redox reaction in which the GSH interacts with a Reactive Oxygen Species (ROS). More precisely, GSH peroxidases reduce ROS into unreactive products (H_2O and O_2), whereby GSH is oxidized to glutathione disulfide (GSSG). The power of GSH lies in its reusability, as GSSG can be transformed and recycled back into GSH by GSH reductase, using NADPH as a reducing agent (**Illustration 20**) (Ducker and Rabinowitz, 2017).

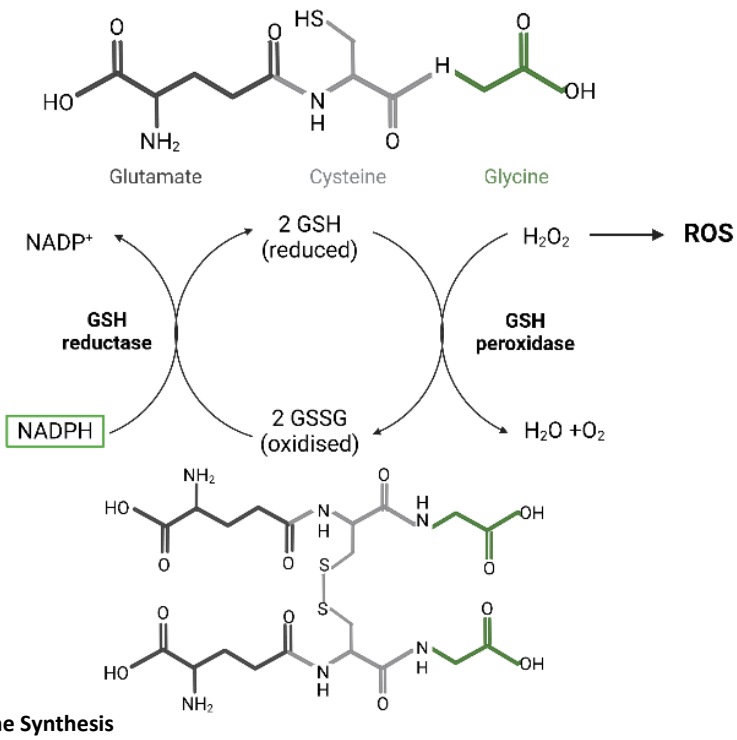

Illustration 20: Glutathione Synthesis
Schematic depiction of the action of GSH. Illustration created with BioRender.com

The 1C metabolism plays also a dual role in the Redox balance of the cell: (1) Glycine, a metabolic by-product of the 1C cycle, is directly incorporated into GSH. (2) NADPH, required for the conversion of GSSG into GSH, can be generated by the 1C metabolism. Actually, 2 molecules of NADPH can be generated by the 1C cycle when the third carbon of serine is completely oxidized into CO_2 – one by MTHFD2 as well as one by ALDH1L2/ALDH1L1 (**Illustration 21**).

The NADPH/$NADP^+$ ratio in cancer cells and the influence of the 1C cycle on this ratio has been investigated in several independent studies. The knockdown (KD) of the mitochondrial enzymes: *SHMT2*, *MTHFD2* or *ALDH1L2* decreases the NADPH/$NADP^+$ ratio, which in turn leads to an increase in ROS (Fan et al., 2014). Notably, at high levels, ROS is a key factor in cancer progression as it can promote cell proliferation, the accumulation of oncogenic mutations, the survival and the adaptation to hypoxia (Liou and Storz, 2010).

Furthermore, the level of ALDH1L2, an enzyme that directly affects the NADPH/NADP$^+$ ratio, was identified to be increased in many tumour types. Silencing of *ALDH1L2* prevented the distant metastasis of melanoma cells in mice (Krupenko and Krupenko, 2018; Piskounova et al., 2015).

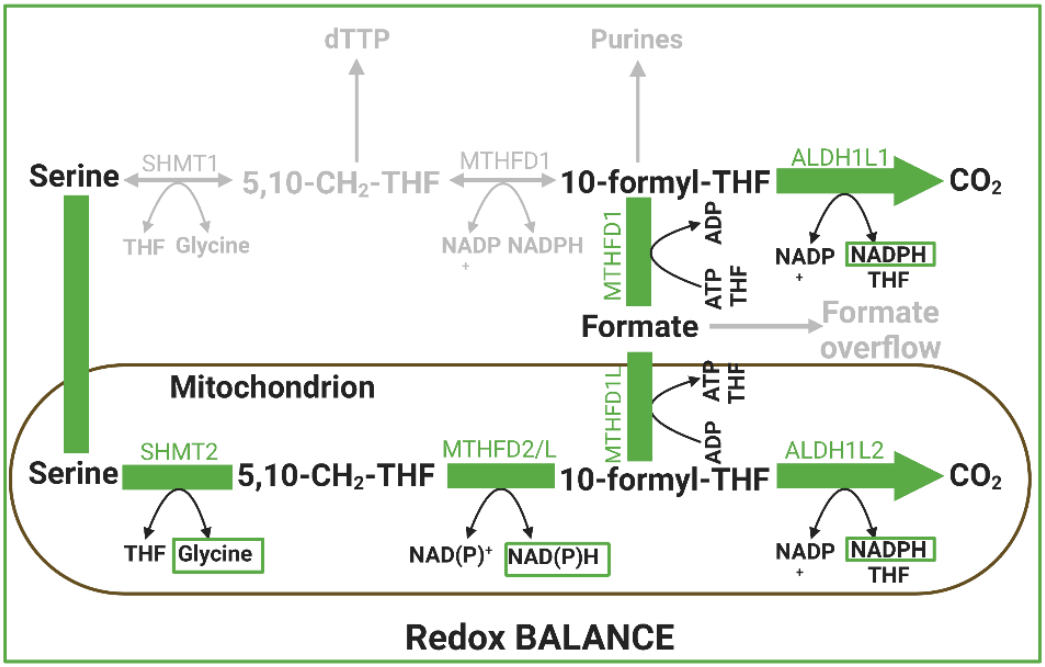

Illustration 21: Relevance of the 1C Metabolism in Redox Balance
Illustration adapted from (Benzarti et al., 2020) and created with BioRender.com.

The previous observations highlight that, cancer cells can adapt the 1C metabolism to support macromolecule biosynthesis, provide ATP to support bioenergetics, support DNA/RNA methylation, and balance oxidative stress.

4.4 The Flexibility of the 1C Metabolism during Cancer Progression

As the 1C metabolism plays an essential role in biosynthesis, bioenergetics, and Redox balance, it is not surprising that cancerous cells hijack the 1C metabolism to support tumorigenesis. As the metabolic need strongly varies between the different steps of cancer progression, cancer cells need to constantly adapt their 1C metabolism to their current demand. During the primary and secondary tumour growth, cancer cells rewire the 1C metabolism to support nucleotide synthesis, which enables a fast cell proliferation. In contrast, during the growth-independent processes of invasion and metastasis, cancer cells polarize their metabolism towards energy synthesis and Redox balance (Benzarti et al., 2020) (**Illustration 22**).

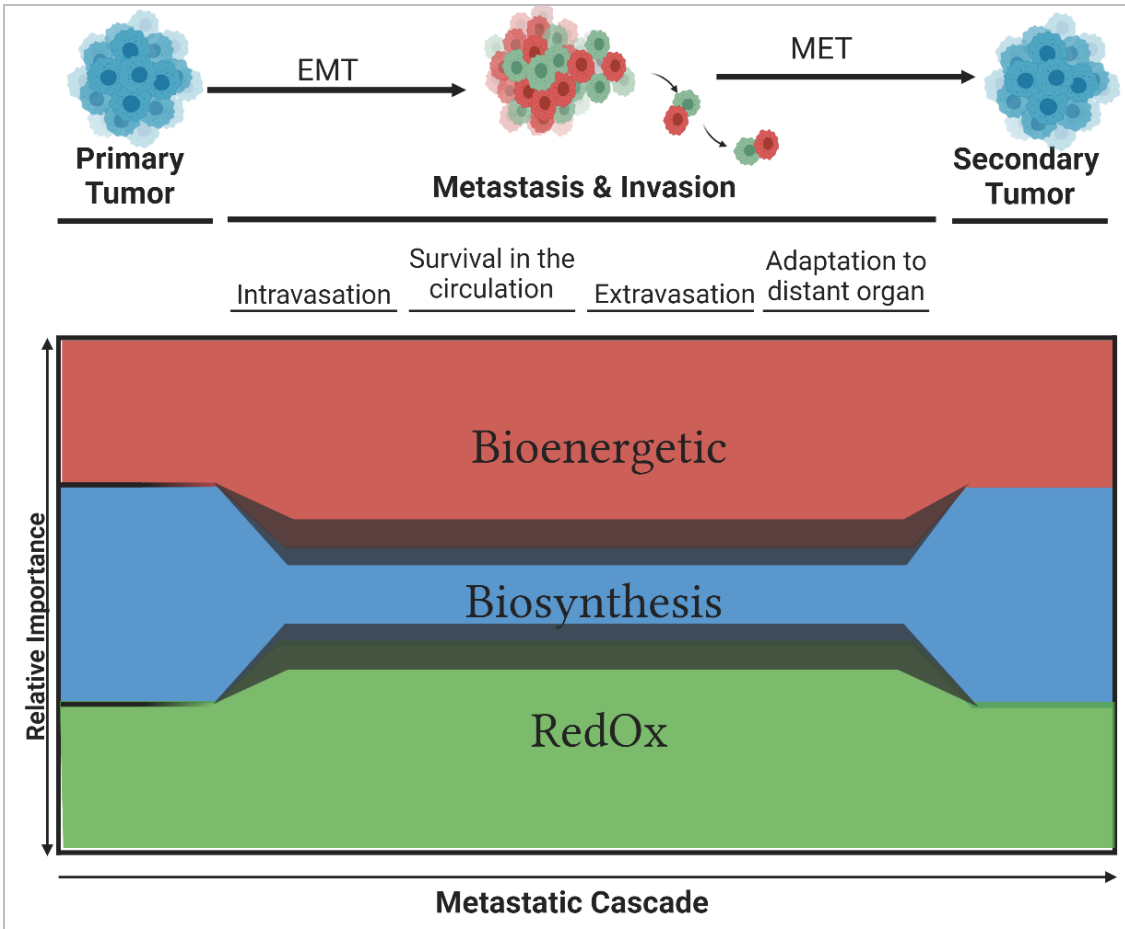

Illustration 22: Flexibility of the 1C Metabolism during Cancer Progression
Illustration adapted from (Benzarti et al., 2020) and created with BioRender.com.

5. Methylene THF Dehydrogenase 1-Like (MTHFD1L)

The mitochondrial enzyme MTHFD1L was first discovered in *Saccharomyces cerevisiae* by Paukert and his co-workers in 1977 (Paukert et al., 1977). Ten years later, the enzyme was cloned and characterized by Shannon and Rabinowitz (Shannon and Rabinowitz, 1986, 1988). Interestingly, in yeast, MTHFD1L is a trifunctional enzyme with dehydrogenase, cyclohydrolase, and synthetase activity (Christensen and Mackenzie, 2008). In contrast, the mammalian mitochondrial 1C cycle only contains a monofunctional MTHFD1L enzyme that catalyses the conversion of 10-formyl-THF and ADP into formate and ATP. MTHFD1L is similar in size and structure to its cytoplasmic homologue MTHFD1. However, due to mutations of critical residues, its dehydrogenase and cyclohydrolase reaction sites are non-functional in mammalian cells (Christensen and Mackenzie, 2008).

MTHFD1L acts as a peripheral membrane protein, which is associated with the matrix side of the mitochondrial inner membrane (Prasannan and Appling, 2009). Like MTHFD1, the mitochondrial isoform MTHFD1L is ubiquitously expressed in mammalian tissue. Yet, the expression level varies between different organs. High levels of MTHFD1L were detected in the brain, thymus, spleen, lung, ovary, and placenta, while liver, muscle, lymphocytes, and kidney levels are relatively low (Prasannan and Appling, 2009; Prasannan et al., 2003; Sugiura et al., 2004; Walkup and Appling, 2005).

5.1 MTHFD1L and Disease

The interest in MTHFD1L significantly increased (**Illustration 23**) after it was identified to be causally related to several common diseases including coronary artery diseases, Alzheimer's disease (AD), neural tube defects (NTDs), and cancer (Ma et al., 2012; Momb et al., 2013; Samani et al., 2007; Sugiura et al., 2004).

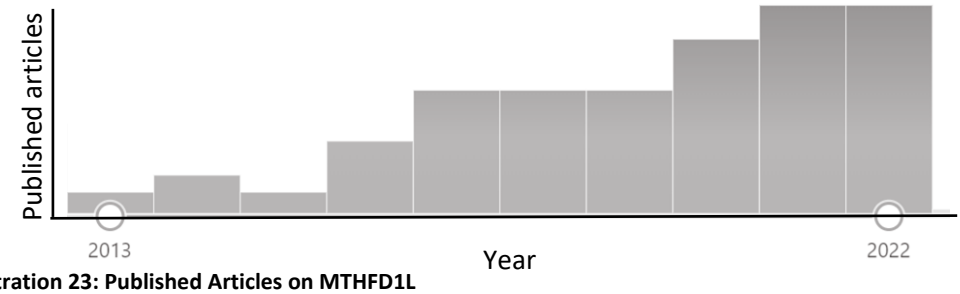

Illustration 23: Published Articles on MTHFD1L
Increase of published articles focusing on MTHFD1L. The data was obtained from PubMed. (copied the 10/01/2023)

In 2007, genome-wide association studies (GWAS) identified the *MTHFD1L* gene to be strongly associated with coronary artery disease (Samani et al., 2007). The statistical disease risk increased by 23% when the *MTHFD1L* gene harboured a single nucleotide polymorphism (SNP) in intron 9 leading to the genetic variant rs6922269 (Samani et al., 2007). These findings were later confirmed by an independent GWAS performed in a German population (Bressler et al., 2010).

Another GWAS demonstrated that SNP rs11754661, in *MTHFD1L* intron 6, is associated with AD risk (Naj et al., 2010). This finding was confirmed by two independent case-control studies performed on a Chinese population (Ma et al., 2012; Ren et al., 2011). Studies characterizing the rs11754661 variant concluded that the enzyme was less active resulting in decreased folate and increased homocysteine levels (Molloy et al., 1997). Imperatively, elevated plasma homocysteine levels have already been associated with AD progression (Van Dam and Van Gool, 2009).

Furthermore, MTHFD1L was identified to be very important in the neural tube development that takes place during the embryogenesis. Loss of *MTHFD1L* in genetically engineered mice was found to be lethal, causing foetal growth restriction and aberrant NTDs (Momb et al., 2013). Similarly, mutations in *MTHFD1L* in humans were associated with an elevated risk of NTDs (Parle-McDermott et al., 2009).

Recently, MTHFD1L was also associated with different types of cancer. An increased expression of *MTHFD1L* was denoted in benign adenoma tissues (1.45-fold), colon adenocarcinoma (2.38-fold), stomach cancer (1.97-fold), and pancreatic cancer (1.44-fold) (Sugiura et al., 2004). In the same paper, the authors demonstrated that the overexpression of *MTHFD1L* promoted cell growth and colony formation of HEK293 cells (Sugiura et al., 2004). In 2017, *MTHFD1L* was identified to be involved in hepatocellular carcinomas growth and *MTHFD1L* deletion resulted in a significant cancer growth arrest (Lee et al., 2017). In 2019, *MTHFD1L* was linked to colorectal cancer (CRC), and *MTHFD1L* blocking attenuated various malignant characteristics of CRC cells, such as proliferation, colony formation, invasion and migration (Agarwal et al., 2019). In 2019, *MTHFD1L* overexpression in tongue squamous cell carcinoma (TSCC) correlated with shorter overall survival and disease-free survival (Li et al., 2019).

Although these findings underline the importance of MTHFD1L in different diseases, mechanistic insights highlighting their relation are still missing. Understanding this fundamental key enzyme in further detail may help to develop novel targeted therapeutics.

New research results further highlighted a possible link between *MTHFD1L* upregulation and cancer progression. Using a genome-scale model of human cell metabolism, Vazquez *et al.*, predicted energy generation through the mitochondrial 1C metabolism coupled with the release of one formate molecule (Vazquez et al., 2011). Subsequently, the computational prediction was experimentally proven *in vitro* as well as *in vivo* using stable isotope labelling and metabolic flux analysis. Therein, cultured cancer cells were shown to excrete formate into the extracellular medium in an MTHFD1L-dependent manner (Meiser et al., 2016). *MTHFD1L* silencing resulted in reduced formate release or even a switch to formate uptake (Meiser et al., 2018; Meiser et al., 2016).

Furthermore, the catabolic conversion of serine to formate was measured to be significantly increased in tumours also *in vivo* (Meiser et al., 2018). Three out of four GEMMs showed higher plasma formate levels at the clinical end-point compared to their age-matched controls (Meiser et al., 2018). An in-depth analysis of colorectal and breast cancer tissues revealed also increased formate overflow in cancer tissues compared to normal tissues (Meiser et al., 2018).

Moreover, recent results from our laboratory, revealed that MTHFD1L remains active upon anti-folate treatment. Due to the compartmentalization of the 1C metabolism, the THF pool in the mitochondria is maintained to allow SHMT2-dependent serine catabolism (Kiweler et al., 2022). As a result, formate overflow is sustained even in the presence of Mtx. Taken together, the results consolidate that formate overflow is a frequent phenotype in cancer cells (**Illustration 24**).

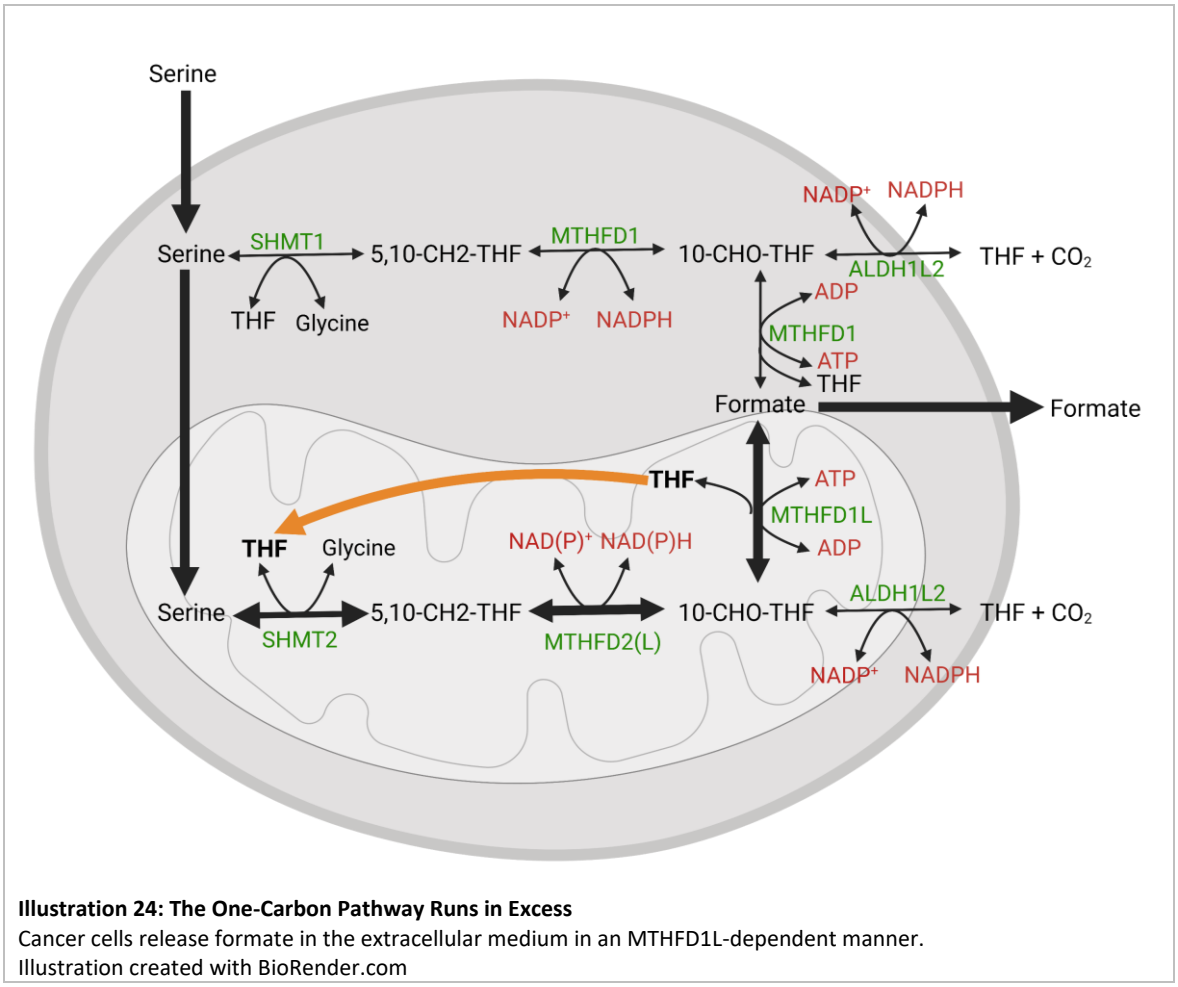

Illustration 24: The One-Carbon Pathway Runs in Excess
Cancer cells release formate in the extracellular medium in an MTHFD1L-dependent manner.
Illustration created with BioRender.com

6. Formate

Formate, also known as methanoate, is a monocarboxylic acid anion representing the conjugate base of formic acid (**Illustration 25**). The word “formic” is derived from the Latin word “*formica*”, referring to its isolation from a distillate of the ant species *Formicidae Hymenoptera* in 1670 (Wray, 1670). Ants and other insects accumulate formic acid in secretory glands and release their content as a defence mechanism. Later, it was discovered that the biosynthesis of formic acid in ants is closely related to the mammalian 1C metabolism (Hefetz and Blum, 1978). Indeed, through radioactive labelling, Hefetz and Blum identified serine to be the major precursor of formic acid biosynthesis (Hefetz and Blum, 1978). Furthermore, they observed that mitochondrial 1C enzymes were highly expressed in the poisonous glands of ants (Hefetz and Blum, 1978).

Formate **Formic Acid**

Illustration 25: Chemical Structure of Formate and Formic Acid

In mammals, standard blood formate levels are found in the range of 10-100 µM (Pietzke et al., 2020). It was assessed that the 1C cycle generates 50% of the global formate production. Indeed, in mice half of the plasma formate was labelled after a bolus intraperitoneal injection of labelled serine (Meiser et al., 2016). The remaining 50% was conjectured to be generated by the gut microbiome as it was found at a millimolar concentration range in the intestinal lumen of mice (Hughes et al., 2017; Pham et al., 2017; Ternes et al., 2022). Methanol (MeOH), another by-product of gut microbial fermentation, can also be metabolized in the liver to formaldehyde and then to formate (Dorokhov et al., 2015). Furthermore, choline catabolism, glycine cleavage, tryptophan catabolism, cholesterol synthesis and sterol synthesis are additional potential sources for formate generation (Pietzke et al., 2020). Yet, the net contribution of these pathways is currently unknown but expected to be little (Pietzke et al., 2020). Recent evidence supports the idea that the origin of formate is highly context-dependent. For example, in absence of serine and glycine, tryptophan-derived formate was shown to be incorporated into nucleotides in cells expressing high IDO1 (the rate-limiting enzyme in the conversion of tryptophan to formyl-kynurenine) levels (Newman et al., 2021).

Much of the work on formate toxicity is related to MeOH poisoning. At a systemic level, MeOH is converted by alcohol dehydrogenase into formaldehyde, which is further converted into formic acid by aldehyde dehydrogenase. High formate levels (around 500 mg/l) are responsible for acidosis, coma, and eventually death (Moon, 2017). At doses between 5 and 30 mM, formate was shown to inhibit cytochrome *c* oxidase (Nicholls, 1975). More recently, 1 mM formate was shown to cause neurotoxicity in rat hippocampal brain slices (Kapur et al., 2007).

6.1 Non-metabolic Function of Formate

It was shown that formate is not fully metabolized further for nucleotide synthesis even in highly proliferative cancer cells. In contrast, formate was shown to be released at rates lower but comparable to the rate of serine uptake in proliferating cancer cells. Reducing the biosynthetic demand by slowing down cell proliferation significantly increased formate overflow (Meiser et al., 2018; Meiser et al., 2016).

As previously described, loss of *MTHFD1L* was found to be embryonically lethal, causing foetal growth restriction and aberrant NTDs. Yet, sodium-formate supplementation in the drinking water of *MTHFD1L*-deficient mice was able to rescue NTDs (Momb et al., 2013). Nonetheless, the exact mechanism for this observation remains unknown. As neural tube formation relies on similar processes than cancer cell progression (cell proliferation, cell polarity, and cell migration) (Copp and Greene, 2013), Meiser *et al*. hypothesised that formate impacts cancer cell motility and invasion.

Using Boyden chamber assays, they analysed the cell invasion of three different glioblastoma (GBM) cell lines (LN-229, NCH601, and U87) that were exposed to different formate concentrations. This study revealed that formate has a dose-dependent effect on cellular invasion (Meiser et al., 2018). Loss of *MTHFD1L* and thus, loss of formate overflow, resulted in lower invasiveness which could be rescued by formate supplementation in the cell culture medium (Meiser et al., 2018).

Overall, these results underline that formate, a metabolic by-product of the 1C cycle, promotes cancer cell invasion through an unknown mechanism (**Illustration 26**).

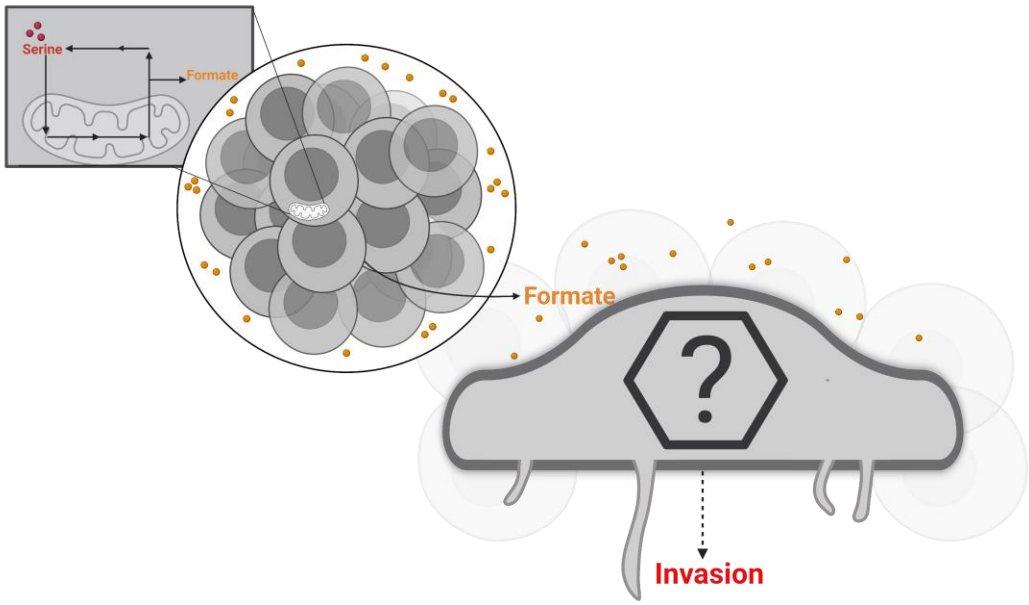

Illustration 26: Formate Promotes Cancer Cell Invasion
Formate, a metabolic by-product of the 1C cycle, promotes cancer cell invasion through an unknown mechanism. Illustration created with BioRender.com

While physiological formate concentration in murine and human plasma is in the range of 10 - 100 µM (Pietzke et al., 2020), the analysis of tumour interstitial fluid (TIF) suggested that in the tumour microenvironment, formate concentration can be significantly above 100 µM (Ternes et al., 2022). Unpublished data even suggests that formate levels in tumours could reach concentrations highly above 500 µM. Considering that 100 µM sodium formate (Na-formate) was already sufficient to significantly increase cancer cell invasion (Meiser et al., 2018), the study of formate-induced invasion is of the highest importance.
Additionally, formate-induced invasion was confirmed by another laboratory in the context of CRC. Specifically, microbiome-derived formate and related high formate concentrations in the gut (10 mM) were shown to exacerbate CRC progression via aryl hydrocarbon receptor (AHR) signalling (Ternes *et al.*, 2022).

Overall, these independent results provide compelling evidence that formate overflow is a feature of different tumours that may increase local formate concentrations in the TME. Such increased local formate concentrations might in turn promote cancer cell invasiveness. Yet, the underlying mechanism that confers such phenotype remains unknown.

Scope & Aims

Mitochondrial 1C production through serine catabolism was shown to exceed the anabolic demand in cancer cells resulting in a phenotype called “formate overflow” (Meiser et al., 2016). Subsequent studies provided compelling evidence that increased extracellular formate concentrations promote the invasiveness of various GBM cell lines *in vitro* (Meiser et al., 2018). However, corresponding *in vivo* evidence and the mechanistic link between formate and invasion are missing.
The objectives of my thesis are as follows:

- Confirm the specificity of formate versus other metabolites as a pro-invasive molecule.

- Investigate the generalizability of formate-induced invasion in various cancer types and assess the applicability of the mechanism to other glioblastoma models as well as to other cancer types.

- Study the physiological relevance of these observations and validate formate as a pro-invasive molecule in physiological models (*ex vivo* and *in vivo)*.

- Investigate the effect of formate on the metastatic capacity of cells.

- Understand the mechanistic details underlying the formate-dependent pro-invasive phenotype.

The conclusions of this work help to understand the selective advantage of serine catabolism with formate overflow and explain its effect on cell invasion. My results outline a function of the 1C cycle beyond serine catabolism and improve the current understanding of mammalian metabolism. Furthermore, the resulting mechanism that models formate-induced cancer cell invasion opens a wide range of potential entry points for therapeutic interventions.

Methodology

1. Cancer Cell Lines and Culture Conditions

The commercially available human GBM cells (LN-229 and U87) and the breast cancer cells (MDA-MB-468, 4T1 and BT20) were cultured in Dulbecco's modified Eagle's medium (DMEM) with no glucose, no glutamine, and no phenol red (**Thermo Fisher Scientific: A1443001**). This culture medium was complemented with 17 mM glucose (**Sigma: G8769**), 2 mM glutamine (**Sigma-Aldrich: 25030081**), and 10% qualified South American foetal bovine serum (FBS) (**Thermo Fisher Scientific: 10500064**).

The LN-229 and MDA-MB-468 cells have been authenticated by Eurofins (ID: 11107531009).

The glioblastoma stem-like cells (GSC) NCH601, which were kindly gifted by Dr Simone Niclou (NORLUX Neuro-Oncology Lab, Luxembourg Institute of Health), were cultured as described in Schuster *et al.* (Schuster et al., 2020). In brief, the cells were cultured as non-adherent spheres in DMEM-F12 medium (**Lonza: 12634010**) supplemented with 1 x Bit-100 (**Provitro: 2043100**), 2 mM of glutamine (**Sigma-Aldrich: 25030081**), 30 U/ml Pen/Strep (**Westburg: LO DE17-602E**), 20 ng/ml basic fibroblast growth factor (bFGF) (**Miltenyi: 130-093-841**), 1 U/ml heparin (**Sigma-Aldrich: H0200000**), and 20 ng/ml epidermal growth factor (EGF) (**Provitro: 1325950500**). The sh*Ctrl* and the formate overflow negative sh*MTHFD1L* cells have been previously described and characterized by Meiser *et al.* (Meiser et al., 2018). The LN229 WT. and the corresponding *AMPK* CRISPR/Cas9-based double knockout, which were kindly gifted by Dr Michael W. Ronellenfitsch, were characterized by Lorenz *et al.* (Lorenz et al., 2022).

The GSCs BG5, BG7, GG6, and GG16 cells, which were also kindly gifted by Dr Simone Niclou (NORLUX Neuro-Oncology Lab, Luxembourg Institute of Health), were also cultured as described in Schuster *et al.* (Schuster et al., 2020). In brief, the GSCs were cultured as non-adherent spheres in a neurobasal base medium (**Thermo Fisher Scientific: 21103049**) supplemented with 1 x B27 (**Thermo Fisher Scientific: 12587010**), 2 mM glutamine (**Sigma-Aldrich: 25030081**), 30 U/ml Pen/Strep (**Westburg: LODE17-602E**), 20 ng/ml bFGF (**Miltenyi: 130-093-841**), and 20 ng/ml EGF (**Provitro: 1325950500**).

The physiological medium, namely Plasmax medium, was set up according to the published protocol by Vande Voorde *et al*. (Vande Voorde et al., 2019). The references and concentrations of the used chemicals are listed below:

Chemical Name	[µM]	Purchase Number
Proteinogenic Amino Acids		
L-Alanine	510	**Carl Roth: 3076.1**
L-Arginine monohydrochloride	65	**Carl Roth: 1689.1**
L-Asparagine	41	**Sigma-Aldrich: A0884**
L-Aspartate	6	**Sigma-Aldrich: A9256**
L-Cysteine hydrochloride	33	**Carl Roth: 3468.1**
L-Glutamate	98	**Sigma-Aldrich: G1251**
L-Glutamine	650	**Thermo Scientific: 25030081**

Glycine	330	**Sigma-Aldrich: 50046**
L-Histidine monohydrochloride monohydrate	120	**Applichem: A3733**
L-Isoleucine	140	**Carl Roth: 1698.1**
L-Leucine	170	**Carl Roth: 1699.1**
L-Lysine	220	**Sigma-Aldrich: L5626**
L-Methionine	30	**Carl Roth: 1702.1**
L-Phenylalanine	68	**Carl Roth: 1709.1**
L-Proline	360	**Sigma-Aldrich: 81709**
L-Serine	140	**Sigma-Aldrich: 84959**
L-Threonine	240	**Carl Roth: 1738.1**
L-Tryptophan	78	**Carl Roth: 1739.1**
L-Tyrosine	74	**Sigma-Aldrich: T3754**
L-Valine	230	**Carl Roth: 1742.1**
Non-proteinogenic Amino Acids		
L-2-Aminobutyric acid	41	**Sigma-Aldrich: A2536**
L-Citrulline	55	**Sigma-Aldrich: C7629**
L-Cystine	65	**Sigma-Aldrich: C7602**
L-Homocysteine	9	**Sigma-Aldrich: 69453**
Trans-4-hydroxy-L-proline	13	**Sigma-Aldrich: 56250**
L-Ornithine monohydrochloride	80	**Carl Roth: 1703.1**
L-Pyroglutamate	20	**Sigma-Aldrich: 83160**
Amino Acids Derivates		
N-Acetyl glycine	70	**Sigma-Aldrich: A16300**
L-Carnosine	6	**Carl Roth: 4148.2**
L-Glutathione (reduced)	37	**Carl Roth: 6832.2**
Taurine	130	**Sigma-Aldrich: T0625**
Betaine	72	**Sigma-Aldrich: 61962**
Other Components		
Sodium acetate	42	**Sigma-Aldrich: S2889**
Acetone	55	**Sigma-Aldrich: 34850**
Acetyl carnitine	5	**Sigma-Aldrich: A6706**
Citrate	114	**Sigma-Aldrich: 27488**
L-Carnitine hydrochloride	46	**Sigma-Aldrich: C0283**
Creatine	37	**Sigma-Aldrich: C0780**
Creatinine	74	**Sigma-Aldrich: C4255**
Formate	33	**Sigma-Aldrich: 71539**
D-Glucose	5560	**Sigma-Aldrich: G8769**
Glycerol	82	**Sigma-Aldrich: G2025**
2-Hydroxybutyric acid sodium salt	31	**Sigma-Aldrich: 220116**
(R)-(−)-3-Hydroxybutyric acid sodium salt	77	**Sigma-Aldrich: 298360**
(±)-Sodium β-hydroxyisobutyrate	20	**Sigma-Aldrich: 36105**
Hypoxanthine	5	**Sigma-Aldrich: H9377**
Sodium L-Lactate	500	**Sigma-Aldrich: 71718**
Methyl acetoacetate	41	**Sigma-Aldrich: 537365**
Phenol red sodium salt	25	**Carl Roth: 2566.1**
Sodium pyruvate	100	**Sigma-Aldrich: S8636**
Succinic acid sodium salt	23	**Sigma-Aldrich: 224731**
Uracil	2	**Sigma-Aldrich: U0750**
Uric acid	270	**Carl Roth: 4999.1**
Urea	3000	**Carl Roth: 7638.1**
Uridine	3	**Carl Roth: 0714.1**
Inorganic Salts		
Ammonium chloride	50	**Sigma-Aldrich: A9434**
Calcium chloride	1800	**Carl Roth: CN93.1**
Magnesium sulfate	813	**Carl Roth: 0682.1**
Potassium chloride	5330	**Sigma-Aldrich: P9541**
Sodium bicarbonate	26191	**Sigma-Aldrich: S6297**
Sodium chloride	118706	**Carl Roth: HN00.2**

di-Sodium hydrogen phosphate heptahydrate	1010	**Carl Roth: X987.1**
Trace Elements		
Ammonium monovanadate	0.0026	**Carl Roth: 4232.1**
Copper(II) sulphate	0.0052	**Carl Roth: CP86.1**
Iron(III)nitratre nonahydrate	0.1238	**Sigma-Aldrich: 216828**
Iron(II) sulphate heptahydrate	1.0428	**Carl Roth: P015.1**
Manganese(II) chloride tetrahydrate	0.0002	**Carl Roth: T881.3**
Sodium selenite	0.0289	**Sigma-Aldrich: S5261**
Zinc sulphate heptahydrate	1.5	**Carl Roth: K301.1**
Vitamins		
Ascorbic acid	62	**Sigma-Aldrich: A0278**
BME vitamins solution 100x	1x	**Sigma-Aldrich: B6891**
Vitamine B12	0.005	**Sigma-Aldrich: V6629**

All the cultured cells were maintained in incubators at 37°C, 5% CO_2, and 95% air atmosphere. Mycoplasma tests were regularly performed by Laura Neises (Cancer Metabolism Group, Luxembourg Institute of Health). No contamination has been encountered during the entire period.

2. Chemicals

Sodium formate (**Sigma-Aldrich: 71539**), sodium acetate (**Sigma-Aldrich: S2889**), sodium lactate (**Sigma-Aldrich: 1614308**), glycine (**Sigma-Aldrich: 50046**), MitoTempo (**Merck: SML0737**), Trolox (**Merck: 238813**), and the calcium chelator BAPTA-AM (**Merck: A1076**) were purchased from Sigma-Aldrich. N-Acetyl-L-Cysteine (NAC) (**Carl Roth: 4126.2**) was purchased from Carl Roth. The MMP inhibitors ARP100 (MMP2 inhibitor) (**Santa Cruz: SC-203522**) and MMP-9 Inhibitor I (MMP9 inhibitor) (**Santa Cruz: SC-311437**) were purchased from Santa Cruz. The FASN inhibitors C75 (**Cayman Chemicals: 10005270-5**) and TVB-2640 (**Selleckchem: S9714**) were purchased from Cayman Chemicals and Selleckchem respectively. The cholesterol biosynthesis inhibitors Fatostatin (**Cayman Chemicals: 13562**) and Simvastatin (**Cayman Chemicals: 10010344**) were purchased from Cayman Chemicals.

3. Cell Proliferation, Adhesion, Migration and Invasion

3.1. Proliferation Assay

The IncuCyte® Live-Cell Analysis (**Essen Bioscience**) system was used to assess cell proliferation. In brief, 5 x 10^3 cells in 100 µL DMEM were seeded on a Greiner 96-well plate. In the case of a pharmacological intervention, the treatment was added to the medium during the entire imaging span. Measurements for individual treatment conditions were performed in technical replicates (n = 6). The proliferation was determined every 4 hours for a total of 72 hours. Cell proliferation was estimated as a measurement of cell density (confluence) using the Incucyte® analysis software.

3.2. Adhesion Assay

The attachment speed of cells was assessed on an ECM-collagen (0.5 mg/ml protein of ECM gel (**Sigma-Aldrich: E1270**) and 0.05 mg/ml collagen type I (**Sigma-Aldrich: A1048301**)) coated coverslips. 5 x 10^4 cells were seeded on coverslips and incubated for 1 hour at 37°C. Subsequently, the cells were fixed through a 15 minutes treatment with 4% Formaldehyde (**VWR: 11699404**) and stained for 15 minutes with 0.05% crystal violet solution (**Sigma-Aldrich: HT90132**). Five pictures per coverslip were taken by an optical inverted microscope at x 20 magnification and the number of adherent cells was counted using a Python script written by the AI department of the Helmholtz Institute München. The script automatically counts the crystal violet stained cells. All counts were manually corrected. The Python code and the full description of the tool can be publicly accessed on GitHub (Piraud, 2022).

3.3. Transwell Migration/Invasion Assay

Migration and invasion were determined using transwell chambers with 8 µm pore size (**Greiner Bio-one: 662638**). Migration was assessed on blank chambers and invasion was determined on matrix-coated chambers. The standard coating is an ECM-collagen coating. The concentrations and references of the used chemicals are listed below:

Coating	Composition
ECM-collagen	0.5 mg/ml protein of ECM gel (**Sigma-Aldrich: E1270**), 0.05 mg/ml collagen type I (**Sigma-Aldrich: A1048301**)
collagen	0.05 mg/ml collagen type I (**Sigma-Aldrich: A1048301**)
ECM	0.5 mg/ml protein of ECM gel (**Sigma-Aldrich: E1270**)
fibronectin	1.12 µg/ml protein of fibronectin (**Sigma-Aldrich: F0895**)
laminin	0.01 mg/ml laminin (**Sigma-Aldrich: L2020**)
poly-L-lysine	25 µg/ml poly-L-lysine (**Sigma-Aldrich: P1274**)

More precisely, 5 x 10^4 cells in 300 µl DMEM lacking FBS, were pipetted into the upper transwell chamber in duplicates per condition. The lower part of the chamber was filled with 750 µl of DMEM supplemented with 10 % FBS. In case of chemical intervention, the compound was spiked into the upper chamber. 24 hours post-seeding, the cells were fixed through a 15 minutes treatment with 4% of formaldehyde (**VWR: 11699404**) and stained for 15 minutes with 0.05% of crystal violet solution (**Sigma-Aldrich: HT90132**). Non-invading cells were removed from the top of the chamber using a cotton tip.

Invasion/migration was quantified by counting the number of cells that invaded/migrated to the lower part of the chamber. Five images per chamber were taken by an inverted microscope at x 20 magnification and the cell count was assessed using a Python script written by the AI department of the Helmholtz Institute München. The script automatically counts the crystal violet stained cells. All counts were manually corrected. The Python code and the full description of the tool can be publicly accessed on GitHub (Piraud, 2022).

3.4 Scratch Assay

Cell Migration was assessed using the IncuCyte® Scratch Wound Assay system for 96-well plates (**Essen Bioscience**). 5 x 10^4 cells contained in 100 µL medium were seeded on 25 µg/ml poly-L-lysine (PLL) coated (**Sigma-Aldrich: P1274**) scratch-plate. Using the 96-pin IncuCyte WoundMaker Tool (**Essen Bioscience**), a wound was scratched through the cell monolayer across each well one day after seeding. Measurements for individual treatment conditions were performed in technical replicates (n = 6). The confluence of the wound area was monitored every 2 hours for a total of 72 hours. Migration was determined as a measurement of cell density (confluence) in the wound area relative to the outer spatial cell density using the Incucyte® analysis software.

3.5 Ex *vivo* brain slice culture

Ex vivo invasion was assessed in an organotypic brain slice culture, as described by Schuster *et al.* (Schuster et al., 2020). Concretely, NSG mice (NOD.Cg-Prkdc^{SCID} Il2rg^{tm1Wjl}/SzJ) were sacrificed through cervical dislocation and their brains were immediately transferred into an ice-cold cutting solution. The cutting solution is composed of DMEM that is supplemented with 0.1% of GlutaMax (**Thermo Fisher Scientific: 35050061**), 25 mM of HEPES (**Thermo Fisher Scientific: 15630080**), and 50 U/ml Pen-Strep (**Westburg: LO DE17-602E**).

Subsequently, the brains were dissected in 400 µm slices using the McIlwain tissue chopper (**Mcclwain Tissue Chopper TC752**). Up to two brain slices have been harvested for one 1 µm transwell chamber. The lower part of the chamber was filled with 1 ml Hibernate^{TM}-A medium (**ThermoFisher: A1247501**) supplemented with 20 % BIT-100 (**Provitro: 2043100**) and 100 U/ml Pen-Strep (**Westburg: LO DE17-602E**). 5 x 10^4 GFP-positive cells contained in 1 µl of ECM, were manually injected with a pipette above the *corpus callosum*. In case of chemical intervention, the compound was added into the lower part of the chamber for the entire experiment. The medium and treatment were renewed every second day. Ten days post-injection, the velocity of cancer cells was assessed for 24 hours using a live cell imager (Green channel, x 4 objective). The movement of 15 cells per condition was tracked using an ImageJ plugin (Schneider, 2012).

3.6 Orthotopic brain tumour model

In vivo invasion was assessed in an orthotopic brain tumour model. The experiment was performed by Anaïs Oudin and Virginie Baus from the Luxembourg Institute of Health (NORLUX Neuro-Oncology Lab, Luxembourg Institute of Health). The NCH601 cells (sh*Ctrl* or *MTHFD1L* KD) were implanted intracranially into the right frontal part of the brain according to the protocol published in Oudin *et al. (Oudin et al., 2021)*. In brief, NU/NU Nude female mice (n=16) were anaesthetized and 3 x 10^5 NCH601 cells were implanted into the right hemisphere of the brain. Two or four months post-implantation, the mice were perfused under deep anaesthesia with a cold heparinized saline solution followed by a fixative solution (**VWR: 11699404**). Subsequently, the brains were rapidly transferred for 48 hours into a 30 % sucrose gradient solution and then stored at - 80°C. 10 µm cryosections were mounted on microscopy slides and stained with 4′,6-diamidino-2-phenylindole (DAPI) (**ThermoFisher Scientific: D1306**) according to the manufacturer's protocol. The distribution of fluorescent-labelled cells was revealed by a fluorescent microscope at x 4 magnification. The invasion was normalised onto the total cell number through a logarithmic ratio (cells left hemisphere/cells right hemisphere). The number of cells in the different hemispheres was determined using a Fiji plugin written by Dr Aymeric Fouquier d'Hérouël from the University of Luxembourg (Cell signalling group, Luxembourg Centre for Systems Biomedicine). The code and the full description of the tool can be publicly accessed on GitHub (Fouquier d'Hérouël, 2021).

4 Metastasis Formation

4.1 Tail Vein Injection Assay

The tail vein injection experiments were performed in collaboration with Dr Elisabeth Letellier's group (Molecular Disease Mechanisms group, University of Luxembourg). The metastatic seeding capacity of MDA-MB-468 cells was studied by intravenous injection of 1 million cells into the tail vein of NSG mice (NOD.Cg-Prkdc^{SCID} Il2rg^{tm1Wjl}/SzJ). Six weeks post-injection the mice were sacrificed by cervical dislocation. The lung and liver were collected and metastatic outgrowth was examined. Half of the organs were dehydrated by ethanol (EtOH), before being stored in phosphate-buffered saline (PBS) and the other half of the organ was snap-frozen into liquid nitrogen. In the dehydrated organs, macroscopic metastases were blindly counted using an optical microscope. The snap-frozen organs were cut into 10 µm cryosections, which were mounted on microscopy slides and microscopic metastases were visualized by Hematoxylin & Eosin (H&E) staining.

4.2 Orthotopic Breast Cancer Model

The orthotopic breast cancer models were performed in collaboration with Dr Elisabeth Letellier's group (Molecular Disease Mechanisms group, University of Luxembourg). The mammary carcinoma 4T1 cancer cells were orthotopically implanted into the left mammary fat pads of immune-competent female Balb/c mice as described in Kocatürk *et al.* (Kocatürk and Versteeg, 2015). In brief, 2000 4T1 cells in a mixture of 25 µL PBS and 25 µl matrigel were injected per mouse. Nine mice per group were injected with either sh*Ctrl* or sh*MTHFD1L* cells. Primary tumour growth was monitored between 7 and 35 days. No change in body weight has been observed during the entire experiment. The experiment was terminated 6 weeks post-injection and lungs and livers were prepared for the examination of metastatic outgrowth. Half of the organs were dehydrated in EtOH, before being stored in PBS and the other half of the organ was snap-frozen into liquid nitrogen. In the dehydrated organs, macroscopic metastases were blindly counted using an optical microscope. The snap-frozen organs were cut into 10 µm cryosections, which were mounted on microscopy slides and microscopic metastases were visualized by H&E staining.

4.3 Hematoxylin & Eosin Staining

Snap-frozen organs were embedded in Tissue-Tek® O.C.T. (**Sakura: 4583**) and 10 µm thick slices were cryosectioned using Leica Cryostat (**Leica Biosystems**). Five sections, each at a distance of 100 µm from the other were stained per organ. H&E staining was performed according to the following protocol: The sections were dehydrated for 10 minutes in 100% methanol (MeOH) (**Carl Roth: 83885**), stained for 1 minute with Gill-2 hematoxylin (**Sigma-Aldrich: GHS232**), and subsequently washed with tap water, hard water (10g $MgSO_4$ (**Carl Roth: 0682.1)** and 0.7g $NaHCO_3$ (**Sigma-Aldrich: S6297**) per litre) and distilled water for 1 minute respectively. Subsequently, the sections were stained for 1 minute with Eosin (**Sigma-Aldrich: 1.09844)** and dehydrated through successive washes of 80%, 95%, and 100% EtOH. Finally, the sections were washed for 5 minutes with Xylol (**VWR: 2875.325**) before being mounted.

5 Metabolomics

5.1 Gas-Chromatography- Mass Spectrometry (GC-MS)

5.4.1 Stable Isotope Tracing and Metabolite Extraction

Stable isotope tracing was performed in DMEM without glucose, glutamine, and phenol red, supplemented with 2 mM glutamine, 17 mM [U-^{13}C]glucose tracer (**Cambridge Isotope Laboratories: CLM-1396**), and 10 % FBS or charcoal-stripped FBS (**Sigma-Aldrich: F6765**). For fatty acid detection, the 2 mM glutamine was replaced by 2 mM [U-^{13}C]glutamine.

4 x 10^5 cells in 1 ml DMEM were seeded in triplicates into a 12-well plate. To normalize intracellular metabolite levels, the packed cell volume (PCV) of identical triplicate wells was calculated (cell volume x cell number) in parallel to metabolite extraction. 24 hours post-seeding, the medium was exchanged for the labelled medium. The cells were cultured for 24 hours in the labelled medium, and for fatty acid detection, the cells were cultured for 72 hours in the labelled medium.

For metabolite extraction, the cells were first washed with 0.9 % ice-cold sodium chloride (NaCl) solution (**Carl Roth: HN00.2**). Subsequently, 400 µl ice-cold GC-MS extraction buffer was added to each well. The extraction buffer is composed of 50 % MeOH (**Carl Roth: KK44.1**) and 50% H_2OMQ supplemented with the internal standards pentanedioc-d6 acid and [U-^{13}C]-ribitol at a final concentration of 1 µg/ml and tridecanoid-d25 acid at a final concentration of 5 µg/ml. After 5 minutes of incubation at 4°C on a rocking shaker, the supernatant was collected into Eppendorf tubes containing 200 µl of ice-cold chloroform (**Sigma-Aldrich: 154733**). Centrifugation for 10 minutes at 13000 g and 4°C separated the sample into two phases: a polar (upper phase) and a non-polar (lower phase). The respective phases were transferred into a vial and dried in a speedvac at 4°C before the MS analysis was launched.

5.1.2. Measurement: Polar Phase

The measurements were performed following the procedure described by Kiweler *et al.* (Kiweler et al., 2022) at the metabolomic platform of the Luxembourg Center of System Biomedicine (LCSB):

“In brief, polar metabolites were derivatized for 90 minutes at 55 °C with 20 µl of methoxyamine (c = 20 mg/ml) dissolved in pyridine under continuous shaking and subsequently for 60 minutes at 55 °C with 20 µl of N-tert-Butyldimethylsilyl-N-methyltrifluoroacetamide (MTBSTFA) w/ 1% tert-butyldimethylchlorosilane (TBDMCS). GC-MS analysis was performed using an Agilent 7890B GC coupled with an Agilent 5977A Mass Selective Detector (**Agilent Technologies**). A sample volume of 1 µl was injected into a Split/Splitless inlet, operating in splitless mode at 270 °C. The gas chromatograph was equipped with a 30 m (I.D. 250 µm, film 0.25 µm) ZB-35MS capillary column with a 5 m guard column (**Phenomenex**). Helium was used as carrier gas with a constant flow rate of 1.2 ml/min. GC oven temperature was held at 100 °C for 2 minutes, then increased to 300 °C at a rate of 10 °C/min, and finally held for 4 min at 300 °C. The total run time was 26 minutes. The transfer line temperature was set to 280 °C. The mass selective detector (MSD) was operating under electron ionization at 70 eV. The MS source was held at 230 °C and the quadrupole at 150 °C. For precise quantification of the MID, measurements were performed in selected ion monitoring mode.

The MetaboliteDetector software package (Version 3.220180913) was used for mass spectrometric data post-processing, quantification, MID calculations, correction of natural isotope abundance, and determinations of fractional carbon contributions (DOI:10.1021/ac802689c)."

5.1.3. Measurements: Non-Polar Phase

The measurements were performed at the metabolomic platform at the Luxembourg Center of System Biomedicine (LCSB). The experiments were performed as described by Modamio *et al.* (Modamio et al., 2021). In brief, derivatization was performed using a multi-purpose sample preparation robot (**Gerstel**). Dried non-polar extracts were dissolved in 30 µl of MTBSTFA w/ 1% TBDMCS and incubated for 60 minutes at 55 °C under continuous shaking.

GC-MS analysis was performed by using an Agilent 7890A GC coupled with an Agilent Mass Selective Detector (**Agilent Technologies**). A sample volume of 1 µl was injected into a Split/Splitless inlet, operating in splitless mode at 280 °C. The gas chromatograph was equipped with a 30 m (I.D. 0.25 mm, film 0.25 µm) ZB-5MSplus capillary column (**Phenomenex**) with a 5 m guard column in front of the analytical column. Helium was used as carrier gas with a constant flow rate of 1.4 ml/min. GC temperature program: 100 °C for 1 minute then increased to 325 °C at 7.5 °C/min and held for 4 minutes. The total run time was 35 minutes. The transfer line temperature was set to 280 °C. The MSD was operating under electron ionization at 70 eV. The MS source was held at 230 °C and the quadrupole at 150 °C. GC-MS measurements were performed in selected ion monitoring mode for precise determination of the MIDs.

5.1.4. Data Procession and Normalization

The analysis was performed as described by Modamio *et al.* (Modamio et al., 2021). MetaboliteDetector (v3.2.20190704) was used to process all GC-MS chromatograms (Hiller et al., 2009). Compounds were annotated by retention time and mass spectrum using an in-house mass spectral library (overall similarity: >0.85). The following deconvolution settings were applied: peak threshold: 2; minimum peak height: 2; bins per scan: 10; deconvolution width: 8 scans; no baseline adjustment; minimum 1 peak per spectrum; no minimal required base peak intensity. MIDs for the following fragments were calculated:

Derivative	Metabolite	m/z	Sum Formula	MID
Hexadecanoic acid 1TBDMS	C16:0	313-332	$C_{18}H_{37}O_2Si$	17
Hexadecenoic acid 1TBDMS	C16:1	311-330	$C_{18}H_{35}O_2Si$	17
Cholesterol 1TBDMS	Cholesterol	443-473	$C_{29}H_{51}OSi$	28

5.2 Liquid-Chromatography - Mass Spectrometry (LC-MS)

5.2.1. Stable Isotope Tracing and Metabolite Extraction

Stable isotope tracing was performed in DMEM without glucose, glutamine, and phenol red, supplemented with 2 mM glutamine, 17 mM [U-^{13}C]glucose tracer (**Cambridge Isotope Laboratories: CLM-1396**), and 10 % FBS (**Sigma-Aldrich: F6765**).

2 x 10^5 cells in 500 µl DMEM were seeded in triplicates in a 24-well plate. 24 hours post-seeding, the medium was exchanged for the labelled medium. The cells were cultured for 24 hours in the labelled medium before the metabolites were extracted. The cells were washed once with ice-cold PBS. Subsequently, 200 µl ice-cold LC-MS extraction buffer (50 % MeOH (**Carl Roth: KK44.1**), 30 % acetonitrile (ACN) (**Carl Roth: AE70.1**), and 20% H_2OMQ containing the internal standards IS-AMP, IS-CPR, IS-CPA, IS-TFL, and IS-TNAD at a final concentration of 1 µg/ml) were added into each well. After 5 minutes of incubation time at 4°C on a rocking shaker, the supernatant was collected into Eppendorf tubes. The tubes were centrifuged for 10 minutes at 13000 g, and 4°C. Subsequently, 100 µl of the metabolite solution was transferred into an LC-MS vial.

5.2.2. Measurements

The measurements were performed at the metabolomic platform of the Luxembourg Institute of Health (LIH).

The LC-MS setup consisted in a Vanquish Flex (**Thermo Fisher Scientific**) liquid chromatography configured to a binary gradient and coupled with a Q-Exactive Plus mass spectrometer (**Thermo Fisher Scientific**). The analytical column was a SeQuant ZIC-pHILIC (**Merck**) (2.1 mm × 150 mm, 5 µm) with a guard column (2.1 mm × 20 mm) and was heated at 45°C in the column oven. Solvent A consisted of 20 mM ammonium carbonate at pH 9.2 with 5 µM of medronic acid. Solvent B consisted in pure ACN. Samples were injected onto the column and eluted by linear gradient ranging from 80% B to 20% B in 15 minutes at a constant flow rate of 200 µl/min. The MS acquisition was performed with a polarity switch between the positive and negative electrospray ionization modes. Full MS spectra were acquired from 75 to 1000 m/z at 70000 resolution (at 200 m/z) with an automatic gain control set to 1e6 charges and a maximum ion trap fill set to 250 ms.

5.2.3. Data Processing

Termo TraceFinderGeneral GC (v4.0) was used to process all LC-MS chromatograms. Compounds were annotated by retention time and mass spectrum using an in-house mass spectral library. The following settings were applied: retention time window: 30 seconds; detection: algorithm genesis; threshold: 1; smoothening 9.

5.3 Seahorse Assay

Basal Oxygen Consumption Rate (OCR) was measured using the XF96 Extracellular Flux Analyser (**Agilent**) according to the manufacturer's manual. In brief, 4 x 10^3 cells contained in 100 µl DMEM were seeded on a 25 µg/ml PLL (**Sigma-Aldrich: P1274**) coated seahorse plate. In the case of chemical intervention, the substance was added 24 hours prior to acquisition.

During OCR acquisition, the cells were sequentially treated with 1.5 µM oligomycin (**Sigma-Aldrich: 495455**), 15 µM carbonyl cyanide *m*-chlorophenyl hydrazone (CCCP) (**Sigma-Aldrich: C2759**), a mixture containing 0.5 µM rotenone (**Sigma-Aldrich: R8875**), and 0.5 µM antimycin A (**Sigma-Aldrich: A8674**).

6. Molecular Assays

6.1 Gelatin Zymography

MMP activity was measured by gelatin zymography assay according to published protocols. In detail, the cells were cultured for 72 hours in DMEM lacking FBS. Subsequently, the proteins contained in the medium were concentrated using Pierce™ Protein Concentrator PES tubes (**Thermo Fisher Scientific: 88517**). The proteins were concentrated through three subsequent centrifugation steps of 13000 g for 30 minutes at 4°C. Protein concentration was assessed by Bradford assay. In total 5 µg of proteins were loaded on NovexTM 10% Zymogram Plus (Gelatin) Protein Gels (**Thermo Fisher Scientific: ZY00102BOX**) contained in 2x non-reducing sample buffer (1M Tris-Hydrochloric acid (HCl) of pH 6,8 (**Carl Roth: 0188.2**); 10% sodium dodecyl sulfate (SDS) (**Carl Roth: 0183.3**); 50% glycerol (**Sigma-Aldrich: G5516**), 0.1% bromophenol blue (**Bio-Rad: 1610404**)).

The proteins were separated by molecular weight using an electrophoresis process at 90 Volt for 2 hours. Subsequently, the gels were washed in a 2.5% Triton X-100 solution (**Carl Roth: 3051.3**) and incubated overnight in an incubation buffer (1% Triton X-100 (**Carl Roth: 3051.3**); 50 mM Tris-HCl pH 7.5 (**Sigma-Aldrich: C1016**); 1 µM Zinc sulphate heptahydrate (**Carl Roth: K301.1**)) at 37°C for the development of zymolytic bands. The gels were stained for 30 minutes in Coomassie Brilliant Blue before being destained for some minutes with a 90% acetic acid solution. Protease bands were detected through the absence of Coomassie Brilliant Blue staining as a result of digested gelatin. The signal under the curve was quantified using an ImageJ plug-in.

6.2 Western Blot

Protein expression and phosphorylation status were assessed by Western Blots.

To study the intracellular proteins of adherent cells, the cells were cultured for 24 hours in DMEM. Subsequently, the cells were lysed directly onto the cell culture dishes with ice-cold cell lysis buffer (150 mM NaCl (**Sigma-Aldrich: S3014**), 1 mM Ethylenediaminetetraacetic

acid (EDTA) (**Sigma-Aldrich: ED**), 50 mM Tris-HCl (**Carl Roth: 0188.2**), 1% IGEPAL® CA-630 (**Sigma-Aldrich: I3021**) containing Protease and Phosphatase Inhibitors (**Sigma-Aldrich: 490687001** & **4693124001**)). To increase cell lysis efficiency, lysates were sonicated for 10 minutes in a water bath. Finally, purification was achieved through 10 minutes of centrifugation at 13000 g and 4°C.

To assess extracellular proteins in the cell culture medium, the cells were cultured for 72 hours in DMEM lacking FBS. Subsequently, the proteins contained in the medium were concentrated using Pierce™ Protein Concentrator PES tubes (**Thermo Fisher Scientific: 88517**). The proteins were concentrated through three subsequent centrifugation steps each lasting 10 minutes at 13000 g, and 4°C.

Protein concentration was assessed by Bradford assays. 30 µg of total protein were loaded on RunBlue 4 - 12% Bis-Tris gels (**GeneScript: M00656**) contained in 4 x NuPage LDS sample buffer (**Thermo Fisher Scientific: NP0007**) and 10 mM dithiothreitol (DTT) (**Sigma-Aldrich: 10708984001**). The proteins were separated by molecular weight through an electrophoresis process with 130 Volt running for 1.5 hours. After migration, proteins were blotted on a nitrocellulose membrane. Total protein loading was quantified using the REVERT staining solution (**LI-COR: 926-11011**) and imaged with the Odyssey CLx Imaging System (**LI-COR**) at 700 nm. Subsequently, the membrane was blocked in 5% milk solution for a minimum of 1 hour at room temperature. Primary antibodies were incubated overnight at 4°C in a 1X Tris-Buffered Saline (TBS), 0.1% Tween® 20 Detergent solution (TBS-T). The used antibodies are listed below:

Antibody	**Reference**
β-actin	**Cell Signaling Technology** (3700) clone 8H10D10, lot18
AMPKα (D5A2)	**Cell Signaling Technology** (5831) clone D5A2, lot8
Phospho-AMPKα (Thr172) (40H9)	**Cell Signaling Technology** (2535) clone T172, lot21
MMP-2 (D4M2N)	**Cell Signaling Technology** (40994) clone D4M2N, lot3
MMP-9	**Abcam** (ab38898) clone GR3204084, lot24
Acetyl-CoA carboxylase	**Cell Signaling Technology** (3676) clone C83B10, lot9
P-Acetyl-CoA carboxylase (Ser79) (D7D11)	**Cell Signaling Technology** (11818) clone D7D11, lot6
mTORC1 (7C10)	**Cell Signaling Technology** (2983S) clone 7C10, lot14
P-mTORC1 (Ser2448)(D9C2)	**Cell Signaling Technology** (5536S) clone D9C2, lot5
Fatty Acid Synthase (C20G5)	**Cell Signaling Technology** (3180S) clone C8D54, lot9

All primary antibodies were used in a 1:1000 dilution in TBS-T. IRDye® secondary antibodies (**LI-COR**) were incubated for 1 hour in the dark at room temperature in a 1:10 000 dilution in TBS-T. Imaging was performed using the Odyssey CLx Imaging System (**LI-COR**) and analysis was done using the ImageStudioLite Software Vers.5.2 (**LI-COR**).

6.3 RNA Extraction, cDNA Synthesis, and RT-qPCR Analysis

To study the intracellular gene expression of adherent cells, the cells were cultured for 24 hours in DMEM. Subsequently, total ribonucleic acid (RNA) was directly extracted from the cell culture dishes according to the RNeasy Mini Kit protocol (**Qiagen: 74104**). The amount and purity of RNA was assessed using a NanoDrop Spectrophotometer.

RNA were converted to complementary DNA (cDNA) using the high-capacity cDNA Reverse Transcription Kit (**Thermo Fisher Scientific: 4368814**).

Quantitative reverse transcription PCR (RT-qPCR) was performed on 20 ng of cDNA per sample using Fast SYBR™ Green Master Mix (**Thermo Fisher Scientific: 4385614**). All samples were analysed in technical triplicates. RT-qPCR using Fast SYBR Green was conducted at 95°C for 20 seconds, followed by 40 cycles at 95°C for 1 second and finally at 60°C for 20 seconds. The comparative cycle threshold (Ct) method was used to quantify the relative mRNA levels. Experiments were performed using the QuantStudio 5 Real-Time PCR System (**Applied Biosciences, ThermoFisher Scientific**). The data was processed by the QuantStudio Design & Analysis v1.5.1 software (**Applied Biosciences, ThermoFisher Scientific**). The expression data was normalized with respect to two housekeeping controls (*GAPDH* and *CycloA*). The primers and their corresponding sequence are listed in the table below:

Gene	Sequence Fwd (5’ – 3’)	Sequence Rev (5’ – 3’)
MMP2	GACCGCTTGGCTTCAAATCA	GGTGTTCAGGTATTGCATGTG
MMP9	CGCGCTGGGCTTAGATCATT	GGTTCAGGGCGAGGACCATA
MMP11	GATCGACTTCGCCAGGTACT	CCCCGATAGTCCAGGTCTCA
MMP16	TGCGGAACGGAGCAGTATTT	GGGGCTTCTTCATCCAGTCAAT
SCD	GTGATGTTCCAGAGGAGGTACTA	TGGCATTAAGCACCACAGC
INSIG1	TTGTTGGCATTAACCACGCC	CAAATGTCCACCAAAGGCCC
FADS2	TTGTCGGGTGTCATGGGC	ACAAATTGCAGCATCTCGTCG
SREBF1	GCACTGAGGCAAAGCTGAAT	GCTGTGTTGCAGAAAGCGAA
FFAR1	CTCAGGCTAATGGCCCTGTC	CAGCGTCACAGGAGATAGGA
FASN	TCGTGTTGACTTCTCGCTCC	CCATCTCTCAAGACCACGGC
CycloA	CAGACAAGGTCCCAAAGACA	CCATTATGGCGTGTGAAGTC
GAPDH	CATGAGAAGTATGACAACAGCCT	AGTCCTTCCACGATACCAAAGT

6.4 RNAseq

RNAseq was performed at the RNAseq platform of the Luxembourg Center for Systems Biomedicine (LCSB).

The RNA was directly extracted from the cell culture dishes using the RNeasy Mini Kit (**Qiagen: 74104**) following the manufacturer's manual. RNA integrity and quantity were determined using the Agilent 2100 Bioanalyzer. An RNA Integrity Number (RIN) above 9 was accepted for downstream analysis.

For library preparation, 1 µg of RNA was poly-(A) selected, fragmented, and reverse transcribed using the Elute, Prime, and Fragment Mix from Illumina.

End repair, A-tailing, as well as adaptor ligation and library enrichment were performed as described in the TruSeq Stranded mRNA library preparation kit (**Illumina: RS-122-2101**). RNA libraries were finally assessed for quality with the Agilent 2100 BioAnalyzer using a high-sensitivity DNA kit (**Agilent: 5067-4626**) and quantified using Qubit high-sensitivity DNA assay (**Thermo Fischer Scientific: Q32854**). An equimolar pool of all RNA libraries was sequenced as a 75 bp single-read run on an Illumina NextSeq500 sequencer at the LCSB sequencing platform (**RRID: SCR_021931**).

RNA-Seq Raw Data was uploaded on GEO under the submission Number: GSE196706.

6.5 Membrane Fluidity Measurement

Membrane Fluidity was assessed according to the manufacturer's protocol using the membrane fluidity kit by abcam (**Abcam: ab189819**). Concretely, in a 6 cm dish, 10^6 cells were seeded in 4 ml supplemented DMEM medium. 24 hours later, a labelling solution containing 10-20 µM fluorescent lipids was mixed in the dark with the cells for 20 minutes at 25°C. Subsequently, the labelling solution was removed and the cells were washed twice with perfusion buffer (provided with the kit). The cells were suspended in DMEM and fluorescence at both 400 and 450-470 nm was read using the appropriate laser emission at 360 nm using the Clariostar Plus (**BMG Labtech**).

7 Statistics

An unpaired *t*-test with Welch's correction was applied for pairwise comparison (two-sided) using GraphPad Software Version 9. Data points of one experiment were either normalized to the untreated control or divided by the global mean of the individual experiment. We define the number of data points as the number of independent biological experiments. In some cases, we consider one such biological independent experiment as the average of technical replicates in several wells, for example, triplicate wells for all stable isotope tracing experiments. The mean values of independent, biological experiments were plotted as data points and used for the statistical analysis as indicated in the corresponding figure legends.

Results

1. Formate is a Specific Activator of Glioblastoma Cell Invasion

1.1 Formate Induces GBM Cell Invasion *In Vitro*

To strengthen the assumption that formate acts as an oncometabolite (Meiser et al., 2018), the pro-invasive role of formate was studied in a variety of GBM cell lines: BG5, BG7, GG16, LN-229, NCH601, and U87. The invasiveness of the corresponding cells was assessed by measuring their translocation into the lower part of an ECM-collagen-coated Boyden chamber. The basal invasive capacity of the different cell lines strongly diverged from each other (Schuster et al., 2020). BG7, GG16, LN-229, NCH601, and U87 cells were identified as highly invasive in comparison to the BG5 and GG6 cells.

Despite the different cell-type specific absolute invasive capacities, all tested cell lines showed an increase in invasiveness upon the addition of 500 µM Na-formate (**Figure 1.1**). On average, a 20 % increase was observed upon exogenous Na-formate supplementation. GG16, LN-229, NCH601, and U87 showed the most robust change.

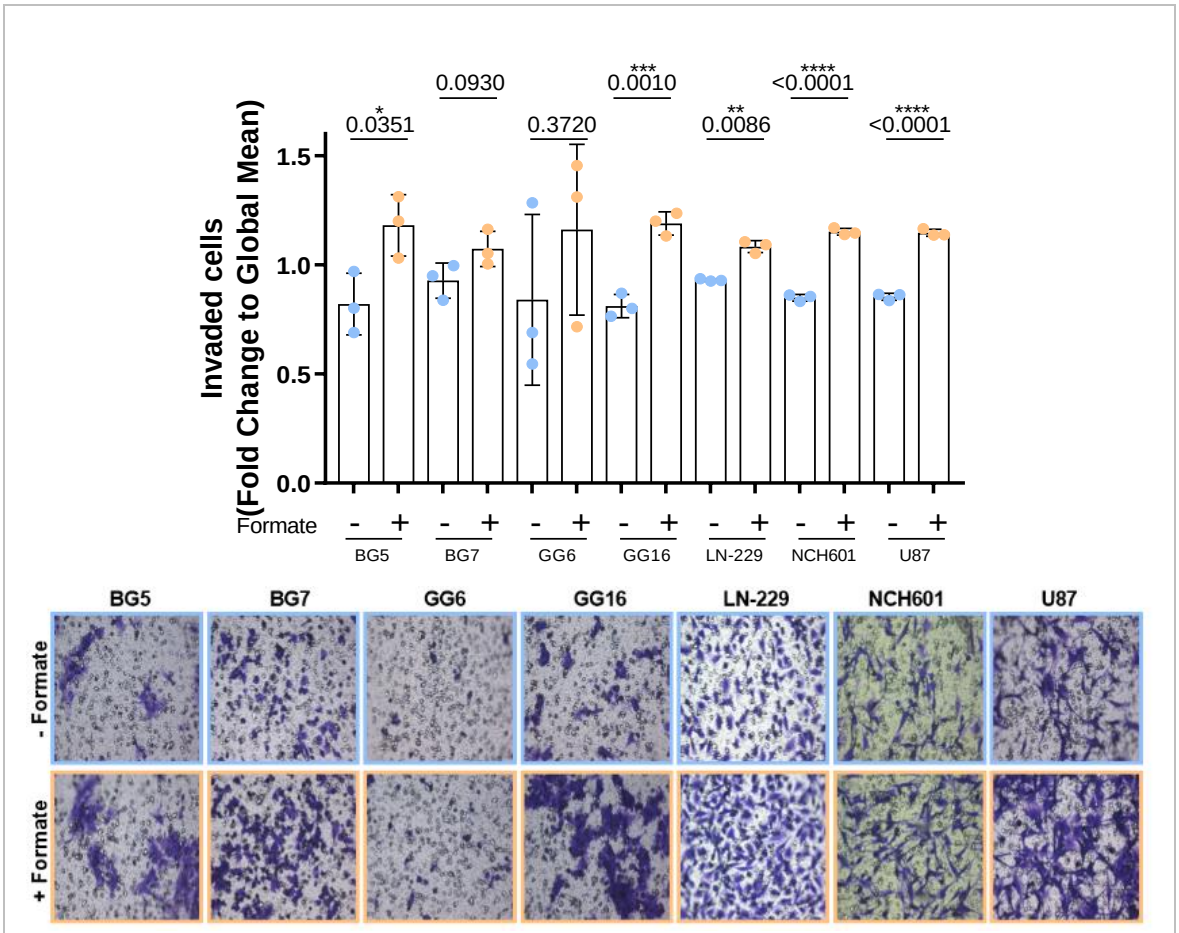

Figure 1.1: Formate Induces Invasion in Different GBM Cell Lines
Top: Invasion of a variety of GBM cells (BG5, BG7, GG6, GG16, LN-229, NCH601, and U87) was assessed using ECM-collagen-coated Boyden chambers. Minus (-) denotes the control group consisting of untreated cells and plus (+) denotes the comparison group consisting of cells treated with 500 µM Na-formate. Each dot represents an independent experiment, the bars represent the mean, and the error bars visualize the standard deviation (SD). The data was evaluated using an unpaired *t*-test with Welch's correction**.** Bottom: Representative images of the Boyden chambers.

1.2 The Specificity of Formate to Promote Invasion

To study the specificity of formate to induce invasion, we repeated the *in vitro* invasion assays of LN-229 cells using other metabolites (**Figure 1.2**). Acetate, which has a similar chemical structure than formate, did not induce any changes in the cells' invasiveness. Glycine, which is released in a 1:1 ratio with formate in the 1C cycle, did also not have an impact on the invasive capacity of LN-229 cells. Lactate, a known oncometabolite (de la Cruz-López et al., 2019; Sonveaux et al., 2008) served as a positive control. Whereas, 500 µM of Na-lactate only slightly increased cancer cell invasion ($p = 0.0518$), the addition of 2 mM Na-lactate induced a similar increase than the supplementation of 500 µM Na-formate. Remarkably, none of these metabolites impacted the cancer cells' proliferation within 24 hours of treatment (**Supplementary Figure 1.1**).

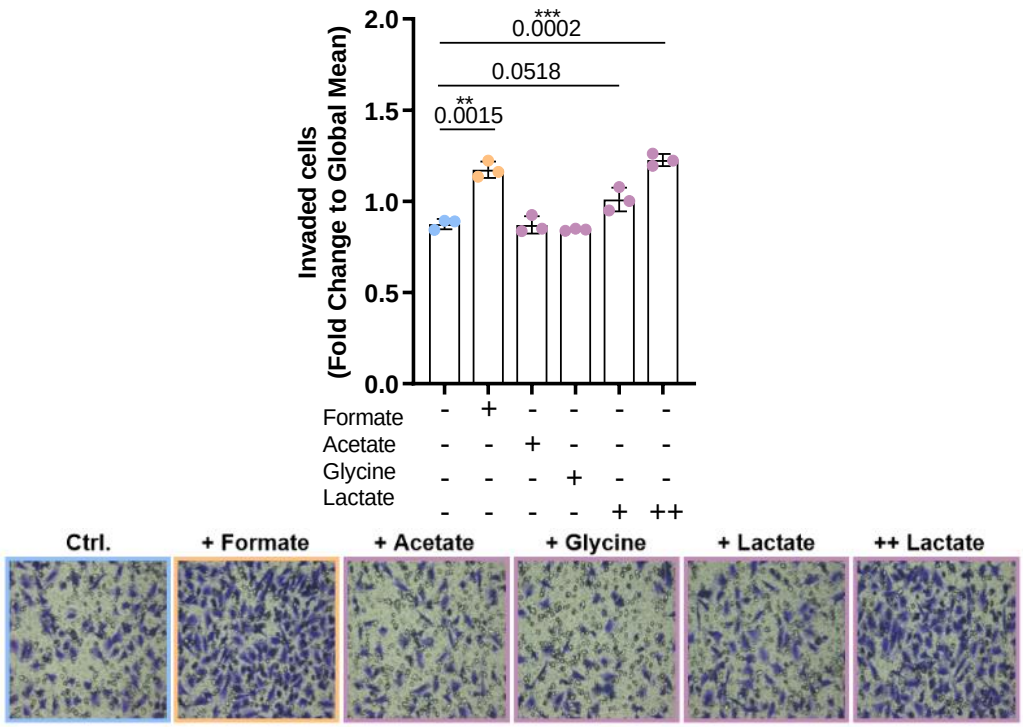

Figure 1.2: The Specificity of Formate to Promote Invasion
Top: Invasion of LN-229 cells, which were either untreated (control) or treated with 500 µM Na-formate, 500 µM Na-acetate, 500 µM glycine, 500 µM Na-lactate, or 2 mM Na-lactate. The fold change was assessed using ECM-collagen-coated Boyden chambers. Each dot represents an independent experiment, the bars represent the mean, and the error bars visualize the standard deviation (SD). The data was evaluated using an unpaired *t*-test with Welch's correction. Bottom: Representative images of the Boyden chambers.

Those results show the specificity of formate to promote an invasive phenotype.

1.3 Formate Promotes Invasion *In Vitro*, *Ex Vivo,* and *In Vivo*

After underlining the positive and specific effect of formate supplementation on GBM invasion *in vitro*, we further verified the physiological relevance of these findings in three distinct experimental approaches.

First, the *in vitro* invasion assay of LN-229 cells was repeated in a Plasmax medium, a medium that mimics the nutrient composition of human blood (Vande Voorde et al., 2019) (**Figure 1.3**). Currently, available cell culture media, including Dulbecco's modified Eagle's medium (DMEM) used in the previous experiments, are known to not fully reproduce the *in vivo* metabolic environment and may cause cell culture-specific metabolic phenotype on cancer cells. However, as the Plasmax experiment produced a similar increase as the original DMEM experiment, the pro-invasive phenotype seems to be medium-independent.

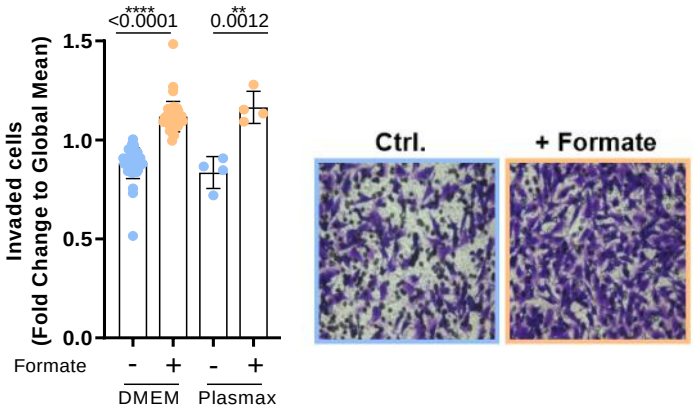

Figure 1.3: Formate Promotes GBM Invasion in the Plasmax Medium
On the left: The comparison of the invasive phenotype of LN-229 cells which were treated for 24 hours with 500 µM Na-formate and cultured in either Dulbecco's modified Eagle's medium (DMEM) or a self-made physiological medium (Plasmax). The invasion was assessed using ECM-collagen-coated Boyden chambers. Each dot represents an independent experiment; the bars represent the mean and the error bars visualize the standard deviation (SD). The data was evaluated using an unpaired *t*-test with Welch's correction. On the right: Representative images of the Boyden chambers performed in the Plasmax medium.

Second, to better mimic the microenvironment of the brain, the invasive capacity of different cell lines was assessed at the single-cell level in an organotypic brain slice culture (Schuster et al., 2020). In an *ex vivo* brain slice assay, the invasion of GBM cells was monitored for 24 hours by tracking cells expressing the green fluorescent protein (GFP) gene (**Illustration 27**). Concretely, mouse brains were dissected in the coronal plane into 400 µm thick slices using a tissue chopper. Subsequently, the brain slices were cultured in a specific medium allowing the survival and integrity of the tissue structure. Subsequently, 5 x 10^4 GFP-labelled cells were injected into the brain slices above the *corpus callosum*. 10 days post-injection, the velocity, implying the invasive capacity of the cells was recorded for 24 hours using a live imager.

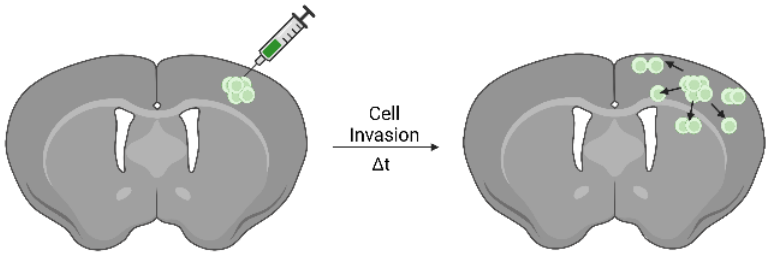

Illustration 27: *Ex Vivo* Brain Slice Culture
Schematic representation of the *ex vivo* brain slice assay. Invasion is monitored for 24 hours by tracking GFP-positive cancer cells that are manually injected above the *corpus callosum*. Illustration created with BioRender.com

The cell lines chosen for injection in the *ex vivo* brain slices were either LN-229 cells or highly invasive NCH601 cells. The velocity of both cell lines was measured in response to formate addition and in dependence of *MTHFD1L* expression using shRNA-mediated knockdown. The slices were maintained for 10 days in a culture that was either supplemented with 500 µM Na-formate or not (**Figure 1.4**). Aligned with our *in vitro* data, the addition of 500 µM Na-formate significantly increased the sh*Ctrl* cell's velocity. In comparison, the velocity of the sh*MTHFD1L* KD cells was significantly reduced. Formate supplementation rescued the reduced velocity of the sh*MTHFD1L* cells. Of note, neither sh*MTHFD1L* nor the addition of 500 µM formate affected the cells' proliferative capacity (Meiser et al., 2018).

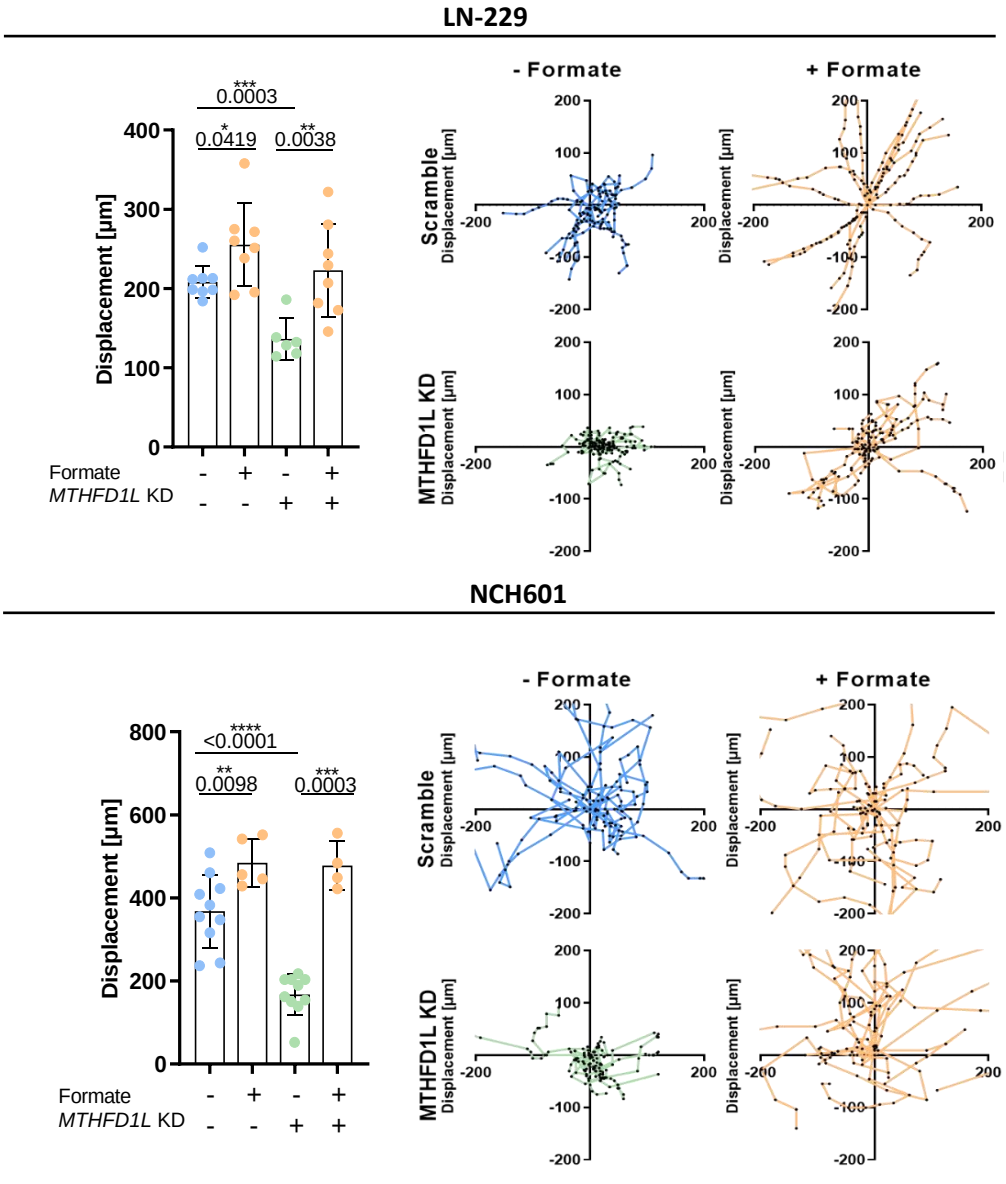

Figure 1.4: **Formate Promotes GBM Cell Invasion in an *Ex Vivo* Model**
Left: Displacement of LN-229 and NCH601 cells (sh*Ctrl* vs. *MTHFD1L* KD) injected in *ex vivo* brain slice cultures. The cells were cultured with 500 µM Na-formate for the entire experiment. Each dot in the bar graph represents the average displacement of 15 cells, the bars represent the mean, and the error bars visualize the standard deviation (SD). The data was evaluated using an unpaired *t*-test with Welch's correction. Right: Representative displacements of 10 cells. Dots and lines represent the trajectory of an individual cell.

Third, the formate-induced invasion was studied in an *in vivo* brain tumour model. The invasion was assessed by injecting GFP-positive cells into one brain hemisphere and counting the number of cells that disseminated into the contralateral hemisphere (**Illustration 28**).

More precisely, either 3 x 10^5 NCH601 sh*Ctrl* or sh*MTHFD1L* cells were implanted into the right brain hemisphere of NU/NU Nude mice. Two or four months post-implantation, the brains were harvested and invasion into the left brain hemisphere was monitored. The intracranial distribution of GFP-positive cells was analysed using an ImageJ plugin written by Dr Aymeric Fouquier d'Hérouël from the University of Luxembourg. The plugin evaluates the invasion as the logarithmic ratio of the number of cells in the left hemisphere divided by the number of cells in the right hemisphere. This procedure normalises the invasion with respect to the total number of cells (Fouquier d'Hérouël, 2021).

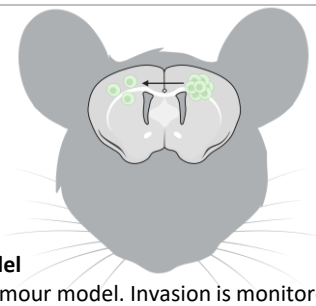

Illustration 28: *In vivo* Brain Tumour Model
Schematic representation of the *in vivo* tumour model. Invasion is monitored by counting the number of GFP-labelled cells that invaded the contralateral hemisphere of the brain. Illustration created with BioRender.com

Two months post-injection, no significant differences between the two groups were observed. These results indicate a similar survival and growth rate between the sh*Ctrl* and sh*MTHFD1L* KD *in vivo*. Yet, four months post-injection, the sh*MTHFD1L* KD cells presented a statistically lower rate ($p = 0.0336$) of dissemination to the contralateral hemisphere than the sh*Ctrl* cells (**Figure 1.5**). This underlines that the inhibition of formate overflow also reduces the invasive capacity of GBM cells *in vivo*.

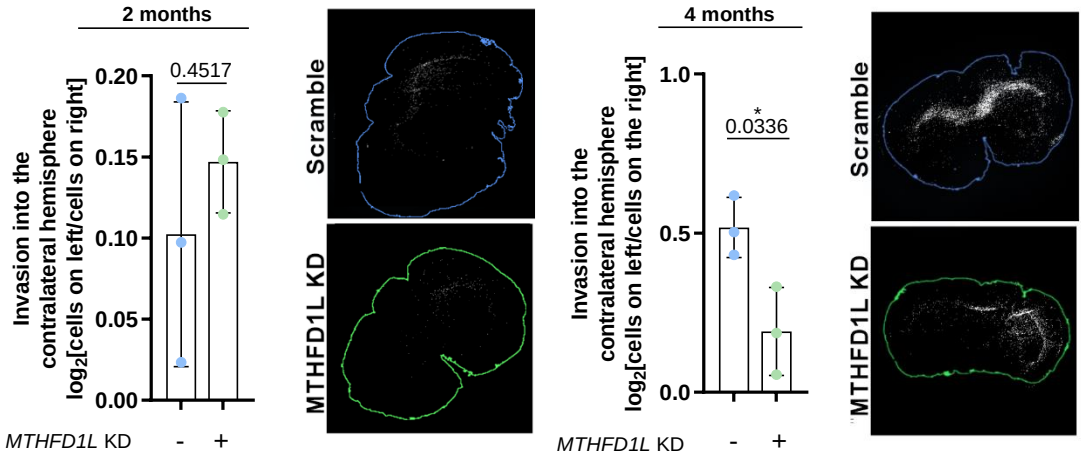

Figure 1.5: Formate Promotes GBM Cell Invasion in an *In Vivo* Model
Invasion of NCH601 (sh*Ctrl vs*. *MTHFD1L* KD) cells into the contralateral hemisphere of NU/NU Nude female mice after 2 and 4 months. Each dot represents the result for a single mouse, the bars represent the mean, and the error bars visualize the standard deviation (SD). The data was evaluated using an unpaired *t*-test with Welch's correction.

These findings highlight the physiological relevance of formate concentration in the microenvironment for the metabolic phenotype of cancer cells. More specifically, the results of those three experimental approaches show that increased extracellular formate concentrations promote cancer cell invasion *in vitro*, *ex vivo,* and *in vivo.* Furthermore, the inhibition of formate overflow using an *MTHFD1L* KD led to a significant reduction of the invasive capacity of GBM cell lines.

2. Formate Primes Cancer Cells into an Invasive Phenotype

As formate was uncovered as a pro-invasive metabolite, the natural question arose whether it also promotes a long-lasting pro-invasive effect. To study this question, GBM cells were pre-treated for different time spans (0, 0.5, 1, 2, 3, 24, and 72 hours) with 500 µM Na-formate and then examined for invasion in Boyden chamber assays (**Figure 2.1**).

Whereas no change in the invasive capacity was noted after 0.5, 1, or 2 hours of pre-treatment (**Supplementary Figure 2.1**), a significant increase in invasion was observed starting from 3 hours of 500 µM Na-formate supplementation (**Figure 2.1**). Interestingly, a positive correlation between cancer cell invasion and pre-treatment duration was observed in U87 cells. Indeed, the highest invasion was observed in U87 cells that were pre-treated for 72 hours. This positive correlation was not monitored in the LN-229 cells, in which the highest invasion was observed after 24 hours of pre-treatment and not after 72 hours.

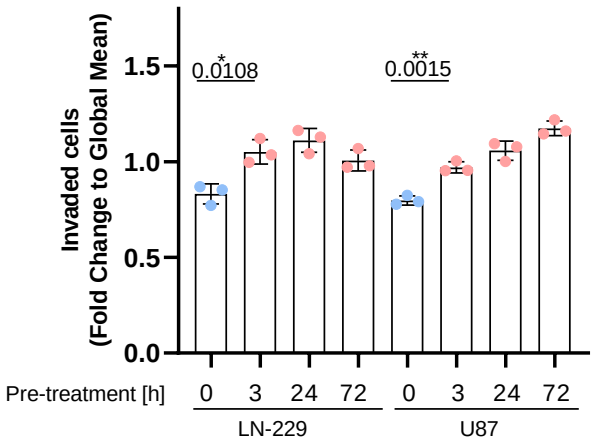

Figure 2.1: Formate Primes GBM Cells to an Invasive Phenotype
Invasion of LN-229 and U87 cells pre-treated for 0, 3, 24, or 72 hours with 500 µM Na-formate. The invasion was assessed using ECM-collagen-coated Boyden chambers. Each dot represents an independent experiment, the bars represent the mean, and the error bars visualize the standard deviation (SD). The data was evaluated using an unpaired *t*-test with Welch's correction.

After having identified that 3 hours of formate pre-treatment were enough to provoke an invasive phenotype in cancer cells, the stability of the pro-invasive signal was investigated. To test the stability of the signal, cancer cells were pre-treated for 24 hours with formate. Then, the treatment was removed and the cells were cultured for different time spans without formate. Finally, the invasive capacity of the cells was investigated using Boyden chambers (**Figure 2.2**). We opted to treat the cells for 24 hours, as it yielded the best pro-invasive signal in the LN-229 cells (**Figure 2.1**)**.** The formate pre-treatment resulted in a transient signal.

The pro-invasive signal in LN-229 cells persisted for 1 hour post-removal. However, this pro-invasive signal in LN-229 cells was lost 3 hours after formate removal. In contrast, in U87 cells, the signal was more stable, persisting even 3 hours post-removal (**Figure 2.2**).

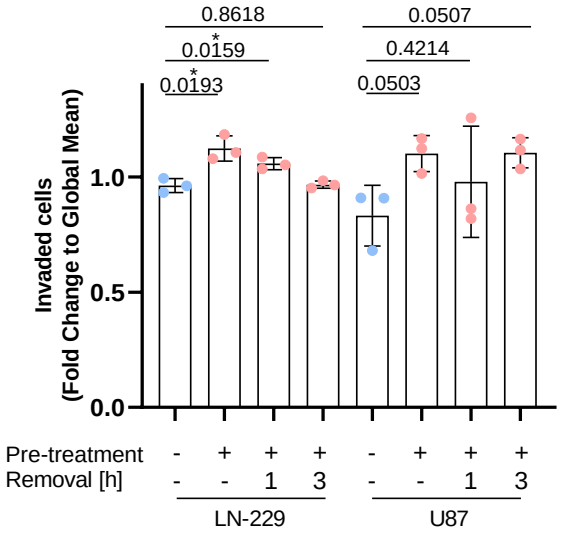

Figure 2.2: Formate's Pro-Invasive Signal in GBM Cells Remains Stable for Several Hours
Invasion of LN-229 and U87 cells, which were pre-treated for 24 hours with formate and then cultured for 1 or 3 hours in a neutral medium. The invasion was assessed using ECM-collagen-coated Boyden chambers. Each dot represents an independent experiment, the bars represent the mean, and the error bars visualize the standard deviation (SD). The data was evaluated using an unpaired *t*-test with Welch's correction.

In conclusion, already after 3 hours of treatment, formate induces an invasive phenotype in cancer cells. Furthermore, this pro-invasive signal persisted for 1 to 3 hours post-removal, which indicates that the induced pro-invasive signal is stable for a short time span.

3. Formate Promotes Metastasis Formation in Breast Cancer

3.1 Formate Induces Invasion in Breast Cancer Cells

After uncovering that formate promotes a transiently stable pro-invasive signal in GBM cells, the role of formate in metastasis formation was analysed. However, as malignant gliomas only rarely metastasize from the central nervous system to other systemic sites (Liwnicz and Rubinstein, 1979; Pasquier et al., 1980), the metastasis-promoting capacity of formate treatment was studied in the context of breast cancer.

First, the pro-invasive effect of formate treatment was verified in breast cancer cells. Therefore, the invasion of three commercially available breast cancer cell lines (BT20, 4T1, and MDA-MB-468) was assessed by *in vitro* Boyden chamber assays. The breast cancer cells displayed different basal invasive capacities. For example, a higher number of MDA-MB-468 cells was counted in the lower part of the Boyden chamber compared to 4T1 cells. Nonetheless, all three cell lines showed an increased invasion capacity after the addition of 500 µM Na-formate (**Figure 3.1**).

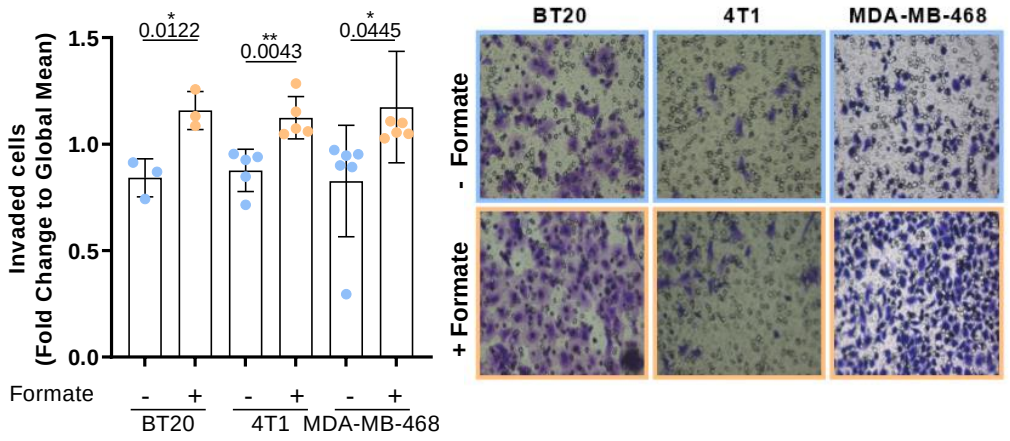

Figure 3.1: Formate Induces Invasion in Breast Cancer Cells
Left: Invasion of the breast cancer cell lines BT20, 4T1, and MDA-MB-468 was assessed using ECM-collagen-coated Boyden chambers. Minus (-) denotes the control group consisting of untreated cells and plus (+) denotes the comparison group consisting of cells treated with 500 µM Na-formate. Each dot represents an independent experiment, the bars represent the mean, and the error bars visualize the standard deviation (SD). The data was analysed using an unpaired *t*-test with Welch's correction. Right: Representative images of the Boyden chambers.

After highlighting that formate also promotes cancer cell invasion in breast cancer cells, the capacity of formate to prime cancer cells to an invasive phenotype was studied in further detail in MDA-MB-468 cells (**Figure 3.2**). Similar as observed in GBM models, formate pre-treated cells (pre-treatment for 24 hours before the Boyden chamber assays) had a comparable invasive potential as acutely treated cells (treatment during the Boyden chamber assays). The addition of extracellular formate during the Boyden chamber assay to pre-treated cells did not further increase the invasion rate.

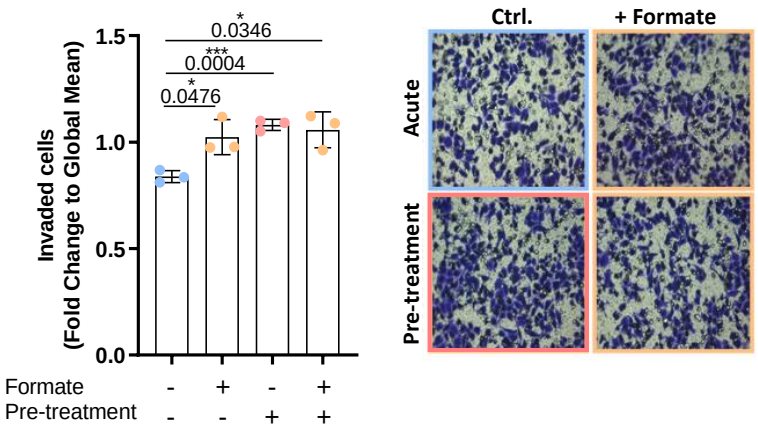

Figure 3.2: Formate Primes Breast Cancer Cells to an Invasive Phenotype
Left: Invasion of MDA-MB-468 cells which were either pre-treated for 24 hours or acutely treated with 500 µM Na-formate. The invasion was assessed using ECM-collagen-coated Boyden chambers. Each dot represents an independent experiment, the bars represent the mean, and the error bars visualize the standard deviation (SD). The data was evaluated using an unpaired *t*-test with Welch's correction. Right: Representative images of the Boyden chambers.

Thus, formate supplementation does not only promote an invasive capacity in GBM cells but also in breast cancer cells.

3.2 Formate Promotes Metastatic Seeding Capacity

To study the metastatic seeding capacity of breast cancer cells *in vivo*, 10^6 MDA-MB-468 cells were injected intravenously into the tail vein of NSG mice (**Illustration 29**). Six weeks post-injection, the number of macroscopic metastases in the lung and liver were blindly counted by eye and microscopic metastases were visualized by Hematoxylin & Eosin (H&E) staining.

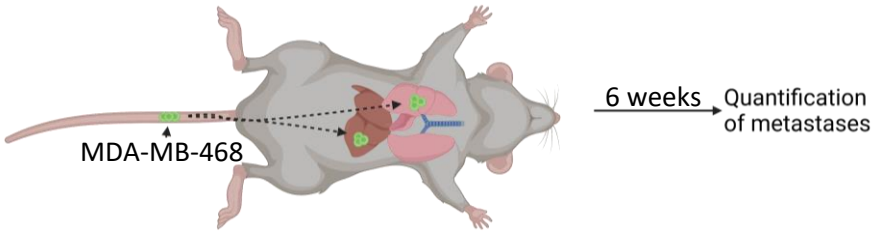

Illustration 29: Tail Vein Injection
To study their seeding capacity, MDA-MB-468 cells were injected into the tail of a mouse. Six weeks post-injection, metastases on the liver and lung were counted. Illustration created with BioRender.com

In the first experimental setup, the MDA-MB-468 cells were either pre-treated for 24 hours with formate or kept untreated before injection. Metastases were found in the liver but not in the lung. Mice that were injected with the formate-primed cells had on average 26 ± 12.51 macrometastases in the liver, whereas mice injected with the untreated control cells only harboured 10.33 ± 8.15 macrometastases on average (**Figure 3.3**). H&E staining confirmed these findings on the microscopic level (**Figure 3.3**).

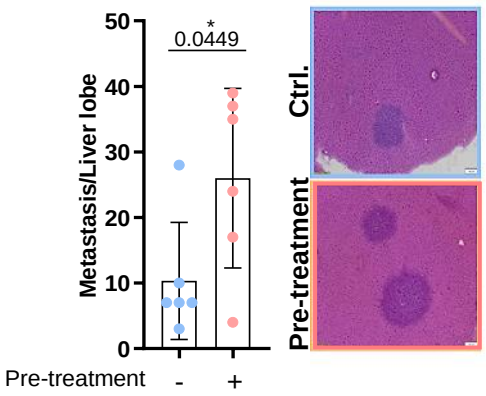

Figure 3.3: Formate Promotes the Seeding Capacity of Breast Cancer Cells *In Vivo*
Left: Macroscopic metastasis count in the livers after injecting either MDA-MB-468 control cells or 24 hours formate pre-treated cells into the tail vein of NSG mice. Each dot represents an independent experiment, the bars represent the mean, and the error bars visualize the standard deviation (SD). The data was evaluated using an unpaired *t*-test with Welch's correction. Right: Representative H&E staining of liver metastases.

To strengthen these findings, formate overflow negative *MTHFD1L* knock-out *(*KO) (Kiweler et al., 2022) and the corresponding wild-type cells (*WT.*) were injected into the tail vein. Six weeks post-injection, a significantly lower rate of liver metastases was observed in the mice that were injected with *MTHFD1L* KO cells (**Figure 3.4**). The mice injected with the control cells had on average 13.5 ± 7.27 metastases per liver. As a similar amount of metastases was found in previous independent experiments (**Figure 3.3**), this result underlines the robustness of our experimental approach. The mice, injected with the *MTHFD1L* KO MDA-MB-468 cells only presented an average of 4.16 ± 2.19 metastases per liver. H&E staining confirmed these findings on the microscopic level (**Figure 3.4**).

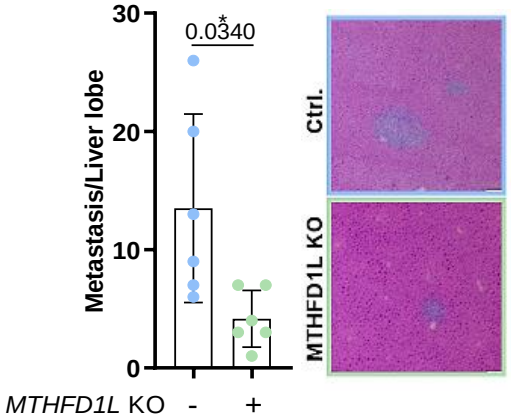

Figure 3.4: Inhibition of Formate Overflow Reduces the Seeding capacity *In Vivo*
On the left: Macroscopic metastasis count in livers after injecting either MDA-MB-468 control cells or *MTHFD1L* KO cells into the tail vein of NSG mice. Each dot represents an independent experiment, the bars represent the mean, and the error bars visualize the standard deviation (SD). The data was evaluated using an unpaired *t*-test with Welch's correction. Right: Representative H&E staining of liver metastases.

Hence, increased extracellular formate levels not only promote local cell invasion but also enhances cancer cell dissemination which is reflected by an increased metastatic seeding capacity.

3.3. Formate Promotes Metastasis Formation in Breast Cancer

Next, an orthotopic *in vivo* model was employed to evaluate the entire metastatic cascade in dependence of formate treatment. In brief, 2000 4T1 cells were injected into the left mammary fat pad of immune-competent female Balb/c mice with the objective to form orthotopic tumours. 6 weeks post-injection, metastases were counted in the liver and lung (**Illustration 30**).

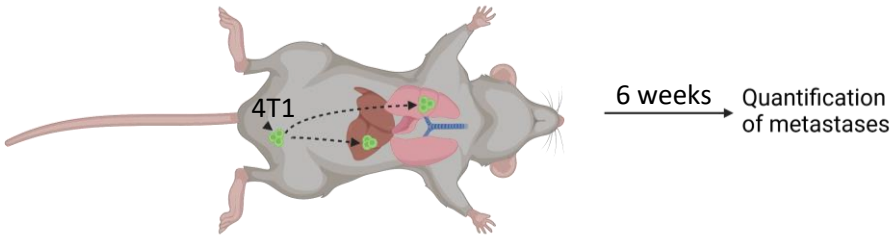

Illustration 30: Orthotopic Breast Cancer Model
To study the entire metastatic cascade, 4T1 cells were injected into the left mammary fat pad of mice. Six weeks post-injection, metastases on the liver and lung were counted. Illustration created with BioRender.com

Within this experiment, we profiled 4T1 sh*Ctrl* and sh*MTHFD1L* KD cells. No difference in the primary tumour weight at the end point was observed (**Figure 3.5**).

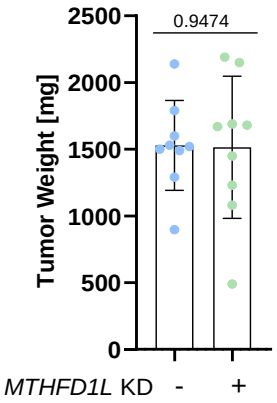

Figure 3.5: Tumour Weight Is Not Affected by *MTHFD1L* Loss
Weight of the primary tumours in mg at 6 weeks post-injection. Each dot represents a mouse, the bars represent the mean, and the error bars visualize the standard deviation (SD). The data was evaluated using an unpaired *t*-test with Welch's correction.

In accordance with our hypothesis, the number of macroscopic lung metastases was significantly reduced in mice that were injected with *MTHFD1L* KD cells (**Figure 3.6**). While all mice that were injected with sh*Ctrl* cells presented lung metastases, over 50% of mice injected with *MTHFD1L* KD cells did not show any macroscopic metastatic lesions. H&E staining yielded similar findings on the microscopic level (**Figure 3.6**). No mouse had detectable metastases in the livers.

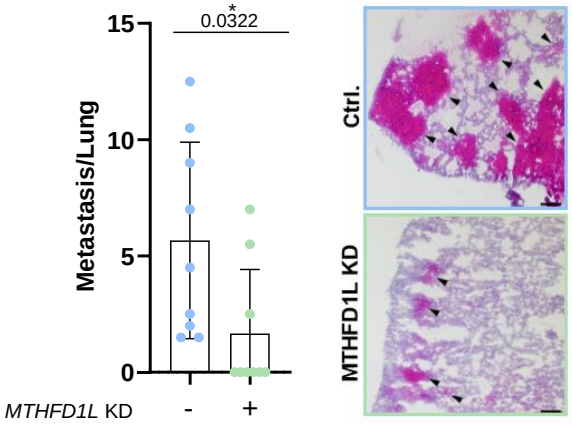

Figure 3.6: *MTHFD1L* KD Reduces Metastasis Formation in an Orthotopic Model
Left: Macroscopic metastasis count in the lungs after injecting 4T1 control or *MTHFD1L* KD cells in the mammary fat pad of Balb/c mice. Each dot represents an independent experiment, the bars represent the mean, and the error bars visualize the standard deviation (SD). The data was evaluated using an unpaired *t*-test with Welch's correction. Right: Representative H&E staining of lung metastases.

All in all, these *in vivo* findings confirm that formate is a key player in the promotion of cancer cell invasion and metastasis. Furthermore, we demonstrate that this effect is independent of the primary tumour growth.

4. Formate Promotes Invasion by Matrix Metalloproteases Release

4.1 Formate Promotes Proteolysis of the Extracellular Matrix

After identifying that formate promotes metastasis in different cancer entities, the next objective was to uncover the underlying mechanism. According to the "hallmarks of metastasis", invasion is important to initiate metastasis (Welch and Hurst, 2019). Invasion consists of three steps: attachment, proteolysis of the extracellular matrix (ECM) components, and migration (Liotta, 2016). Indeed, in the first step tumour cells attach from the ECM. Then, the ECM has to be degraded by proteolysis. At last, the tumour cells migrate through the remodelled matrix.

To explore how formate promotes cancer cell invasion, the impact of formate on each of these three features has been studied. To evaluate the impact of formate on the migratory potential of cancer cells, a migration assay on non-coated Boyden chambers was performed. No changes were noted in all tested cell lines (BG5, BG7, GG16, LN-229, U87, and MDA-MB-468 cells) (**Figure 4.1**). For some cell lines (BG7 and GG16), migration was even significantly reduced by the addition of formate (**Figure 4.1**). Of note, we hypothesised that the cells adhere similarly to the filter as to the coating, as a similar cell number was observed in both assays (invasion vs. migration). To validate these results, we performed an auxiliary wound healing (scratch) assay with LN-229 cells. Different formate concentrations ranging from 0 – 1000 µM did not influence the migration capacity of the cancer cells (**Supplementary Figure 4.1**).

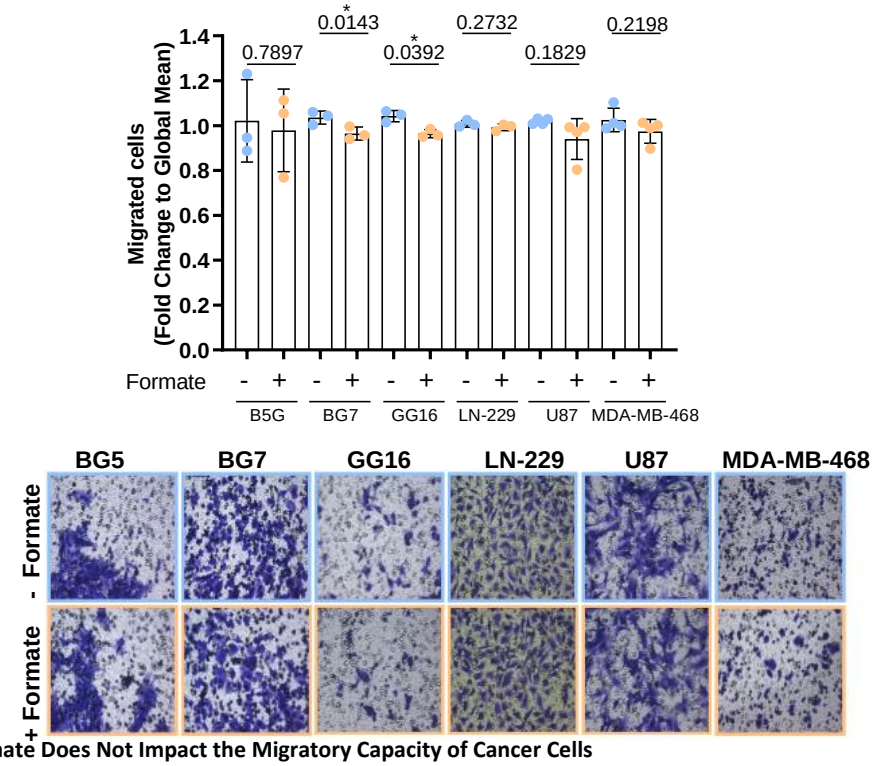

Figure 4.1: Formate Does Not Impact the Migratory Capacity of Cancer Cells
Migration of different cell lines (BG5, BG7, GG16, LN-229, U87, and MDA-MB-468) treated for 24 hours with 500 µM Na-formate was assessed using non-coated Boyden chambers. Minus (-) denotes the control group consisting of untreated cells and plus (+) denotes the comparison group consisting of cells treated with 500 µM Na-formate. Each dot represents an independent experiment, the bars represent the mean, and the error bars visualize the standard deviation (SD). The data was evaluated using an unpaired *t*-test with Welch's correction.

Next, the effect of formate on the cells' attachment capacity was analysed. The adhesion capacity was assessed by counting the number of cells that were fixed on an ECM-collagen layer 1 hour after seeding.

The number of attached cells on an ECM-collagen coated cover slip was significantly increased for formate pre-treated cells (LN-229, U87 and MDA-MB-468) when compared to their untreated equivalents (**Figure 4.2**).

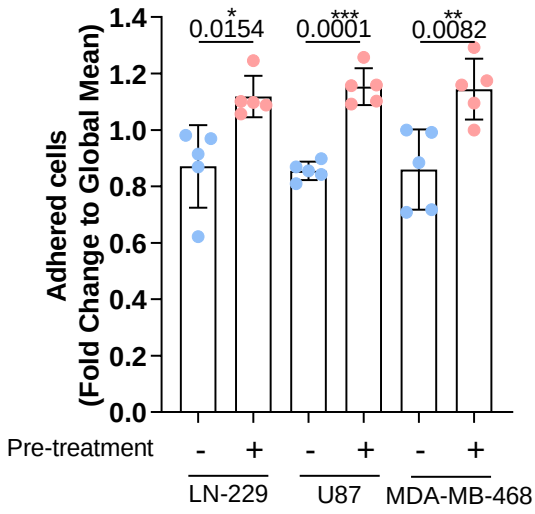

Figure 4.2: Formate Pre-Treatment Impacts the Adhesion Capacity of Cancer Cells
Adhesion of LN-229, U87, or MDA-MB-468 cells, which were either pre-treated for 24 hours with formate, or untreated assessed on ECM-collagen coated coverslips. Each dot represents an independent experiment, the bars represent the mean, and the error bars visualize the standard deviation (SD). The data was evaluated using an unpaired *t*-test with Welch's correction.

This shows that adhesion plays a role in formate-induced invasion. Yet, as formate also promotes metastasis formation, we hypothesised that formate could also impact the ECM proteolysis.

To evaluate whether formate increases the ECM degradation capacity of cancer cells, the cells were seeded in *in vitro* Boyden chambers, which were coated with six different matrices, namely collagen, ECM, fibronectin, laminin, PLL, and ECM-collagen. Therein a coating dependence of formate-induced invasion was observed (**Figure 4.3**). Indeed, cells that had to invade through collagen, ECM, or a collagen/ECM mix showed increased invasiveness after the addition of 500 µM Na-formate. Furthermore, cells invading through fibronectin or laminin showed a positive trend of invasiveness after formate supplementation. However, no difference was observed in Boyden chambers coated with PLL. Notably, PLL coating do not require active matrix proteolysis by the cells and this coating thus represents a migration-like assay. As formate had no effect at all on the invasion through this matrix, this confirms that formate does not impact the migratory capacity of cancer cells (**Figure 4.1**)**.**

Simultaneously, the positive effect observed on collagen and ECM matrices indicates that formate treatment increases the ECM degradation capacity of cancer cells.

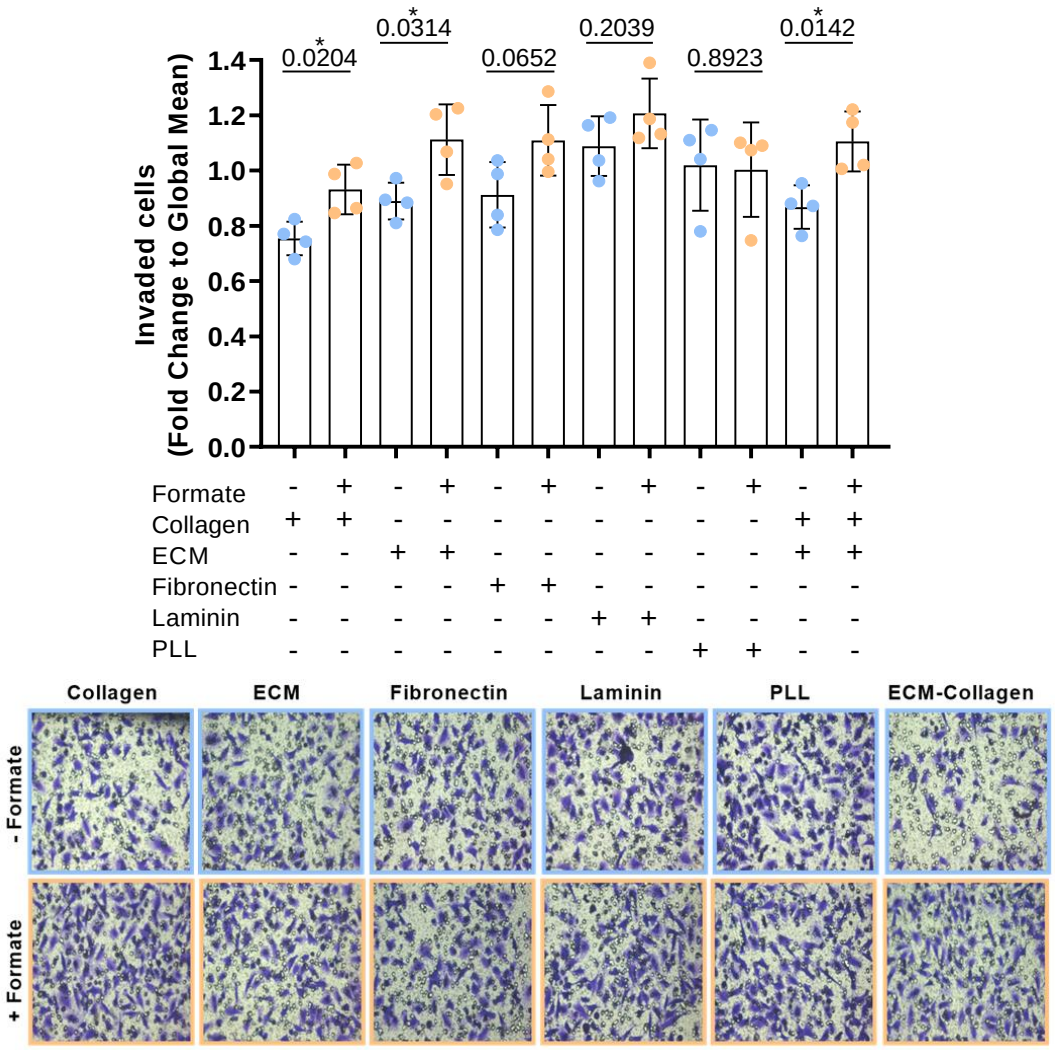

Figure 4.3: Formate-Induced Invasion Is Coating-Dependent
Top: Invasion of LN-229 cells treated for 24 hours with 500 µM Na-formate assessed on a variety of differentially coated Boyden chambers (collagen, ECM, fibronectin, laminin, PLL, and ECM-collagen). Each dot represents an independent experiment, the bars represent the mean, and the error bars visualize the standard deviation (SD). The data was evaluated using an unpaired *t*-test with Welch's correction. Bottom: Representative images of the Boyden chambers.

4.2 Formate Promotes Matrix Metalloproteinases

ECM proteolysis requires the activity of matrix metalloproteinases (MMPs), a group of enzymes that are known to facilitate cancer cell invasion. To substantiate the hypothesis that formate promotes ECM proteolysis, the gene expression of all MMPs was profiled through RNA sequencing. For this analysis, we treated LN-229 cells for 8 or 24 hours with 500 µM Na-formate prior to RNA extraction.

Among the 23 MMPs expressed in human tissues, 18 were detectable in the RNAseq analysis. 8 hours of formate treatment did not have a significant impact on MMP expression. However, 24 hours of formate treatment, significantly increased the expression of three MMPs, namely *MMP2*, *MMP11*, and *MMP16* (**Figure 4.4**).

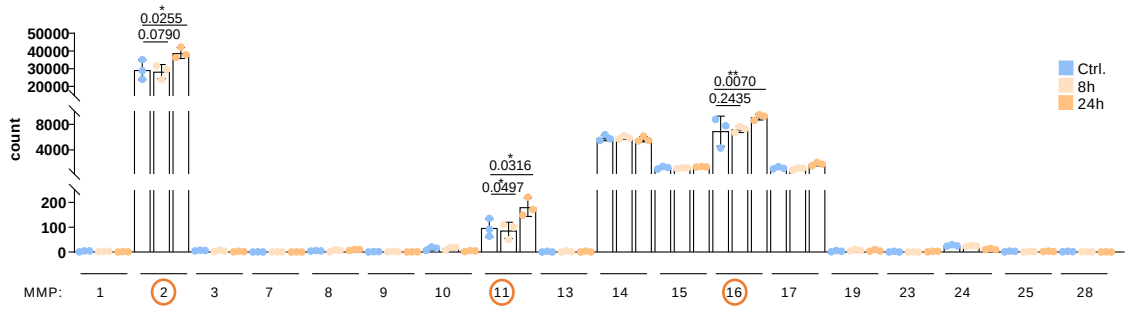

Figure 4.4: Formate Favours *MMP2*, *MMP11*, and *MMP16* Gene Expression
RNAseq results displaying the count of different MMP (*MMP1, MMP2, MMP3, MMP7, MMP8, MMP9, MMP10, MMP11, MMP13, MMP14, MMP15, MMP16, MMP17, MMP19, MMP23, MMP24, MMP25,* and *MMP28*) expressions in LN-229 cells which were either treated for 8 hours or 24 hours with 500 µM Na-formate. Each dot represents a biological replicate, the bars represent the mean, and the error bars visualize the standard deviation (SD). The data was evaluated using an unpaired *t*-test with Welch's correction.

To validate these observations, *MMP2*, *MMP9*, *MMP11*, and *MMP16* expression was monitored by an auxiliary RT-qPCR. We included *MMP9* as a negative control, as it forms with MMP2 the subfamily of gelatinases. Aligned with the RNAseq data, no effect on MMP expression was detected after 8 hours of formate treatment. However, the expression of *MMP2*, *MMP11*, and *MMP16* was increased after 24 hours of formate treatment (**Figure 4.5**).

When investigating MMP gene expression in other cell lines, we uncovered that formate-dependent MMP activation was cell line-dependent. Indeed, the expression of *MMP2*, *MMP11*, and *MMP16* was increased in LN-229 cells. However, *MMP9* was upregulated in U87 cells, and only *MMP11* was increased in MDA-MB-468 cells (**Figure 4.5**). These results highlight that in all tested cell lines, formate promotes MMP upregulation. Yet, the specific MMP expression pattern is cell line-dependent.

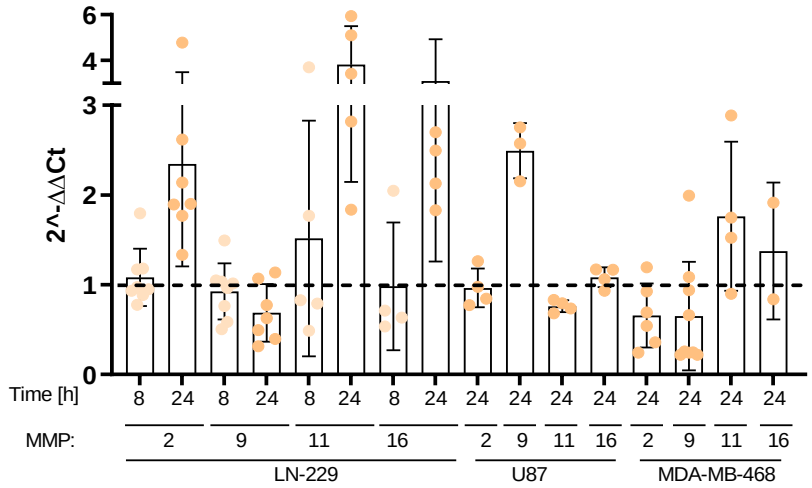

Figure 4.5: Formate-Dependent MMP Activation is Cell Line-Dependent
mRNA expression from *MMP2*, *MMP9*, *MMP11*, and *MMP16* in LN-229, U87, and MDA-MB-468 cells which were pre-treated for either 8 or 24 hours with 500 µM Na-formate. The results are presented as $2^{-\Delta\Delta Ct}$, representing the relative fold gene expression with respect to untreated cells. Each dot represents a biological replicate, the bars represent the mean and the error bars visualize the standard deviation (SD). The fold change of 1, which indicated that there is 100 % as much gene expression as in the control group is represented by a black dotted line.

To further support this data, we measured the release of MMP2 and MMP9 protein by LN-229 cells into the cell culture medium after 500 µM Na-formate treatment (**Figure 4.6**). Interestingly, MMP2 release was coating-dependent, as MMP2 protein could only be detected in the medium when the cancer cells were cultured on an ECM-collagen coating. On the contrary, MMP9 release was coating-independent.

The change in MMP2 release in the cell culture medium was subtle between treatment conditions and difficult to visualize in Western Blot. Nevertheless, the quantification of four independent experiments revealed a significant decrease in MMP2 release in *MTHFD1L* KD cells compared to sh*Ctrl*. Additionally, formate supplementation could partially rescue the reduced MMP2 release in sh*MTHFD1L* KD cells. Aligned with the previous gene expression data, no major changes in MMP9 release were observed (**Figure 4.6**).

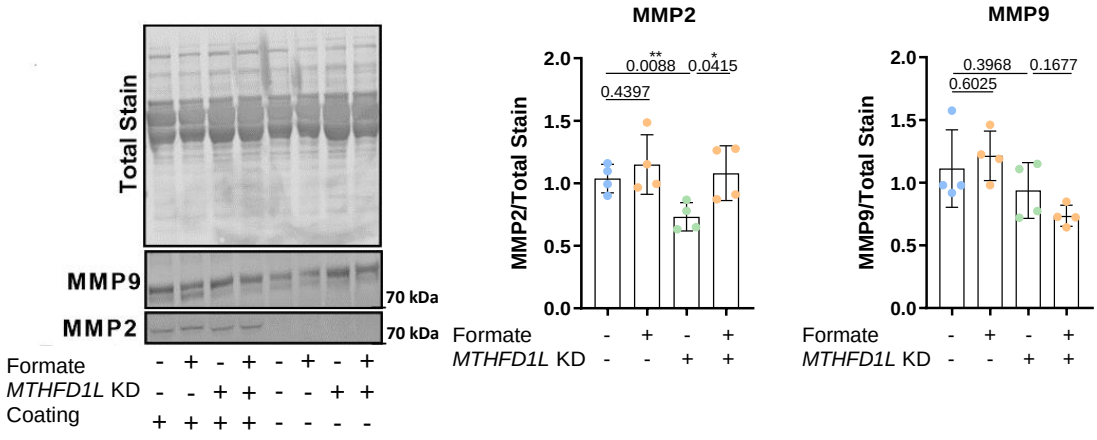

Figure 4.6: Formate Promotes MMP2 Release

Expression of MMP2 or MMP9 in the cell culture medium. The total stain served as a loading control. The signal intensity of MMP has been quantified with respect to the signal intensity of the total stain. Each dot represents an independent experiment, the bars represent the mean, and the error bars visualize the standard deviation (SD). The data was evaluated using an unpaired *t*-test with Welch's correction.

To monitor the enzymatic MMP activity, we applied a gelatin zymography assay. MMP2 and MMP9 are representative of the distinct subclass of gelatinases within the MMP family. To assess their activity, their capacity to degrade a gel composed of gelatin was determined. We identified an increased MMP activity in the cell culture medium of LN-229 cells, which were treated with 500 µM Na-formate. In contrast, stable sh*MTHFD1L* KD cells showed a significant reduction of MMP2 activity compared to sh*Ctrl* cells. The addition of exogenous formate partially rescued the MMP2 activity of sh*MTHFD1L* cells. No changes were noted in MMP9 activity (**Figure 4.7**).

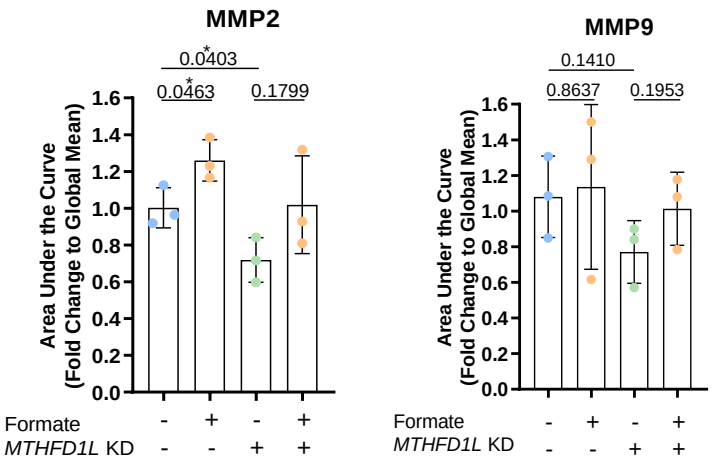

Figure 4.7: MMP2 Activity Is Increased in LN-229 Cells After Formate Treatment
MMP2 and MMP9 activity of LN-229 sh*Ctrl* or *MTHFD1L* KD cells treated for 72 hours with 500 µM formate assessed using a gelatin zymography assay. Each dot represents an independent experiment, the bars represent the mean, and the error bars visualize the standard deviation (SD). The data was evaluated using an unpaired *t*-test with Welch's correction.

To further validate MMP involvement in formate-induced invasion, the impact of a calcium quencher on formate-induced invasion was studied. MMPs are Ca^{2+}-dependent endopeptidases that degrade the ECM and its connective tissue (Visse and Nagase, 2003). Theoretically, in the absence of calcium, MMPs remain inactive and do not degrade the ECM. Accordingly, Bapta-AM, a Ca^{2+} chelator was successful in preventing formate-induced invasion of LN-229 cells (**Figure 4.8**). The used concentration of Bapta-AM did not impact cancer cell proliferation (**Supplementary Figure 4.2**).

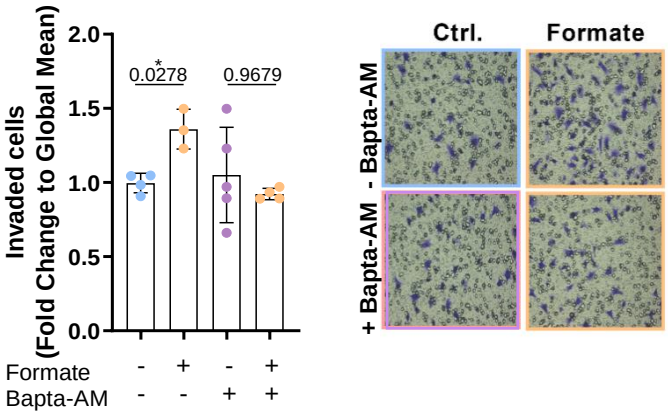

Figure 4.8: Bapta-AM Prevents Formate-Induced Invasion Upon Formate Treatment
Left: Invasion of LN-229 cells treated for 24 hours with either 500 µM formate or 1 µM Bapta-AM assessed on ECM-collagen coated Boyden chambers. Each dot represents an independent experiment, the bars represent the mean, and the error bars visualize the standard deviation (SD). The data was evaluated using an unpaired *t*-test with Welch's correction. Right: Representative images of the Boyden chambers.

The above experiments underline the important role of MMPs in formate-induced invasion.

4.3 Formate-Induced Invasion Relies on MMPs *In Vitro* and *Ex Vivo*

After discovering a link between formate and MMP expression/activity, the causal relationship between both was investigated by testing the invasive capacity of cancer cells after formate addition and MMP inhibition (MMPi).

Aligned with our gene expression analysis, MMP2i (ARP-100) prevented formate-induced invasion while MMP9i (MMP-9 Inhibitor I) had no repressive effect on the invasion of LN-229 cells (**Figure 4.9**). Consequently, in U87 cells, the complementary phenotype was observed: MMP9i showed a repressive effect, while MMP2i did not (**Figure 4.9**). The proliferation rates were not impacted by the concentrations of MMPi, which excludes that the decreased invasiveness is a result of a decreased proliferation (**Supplementary Figure 4.3**).

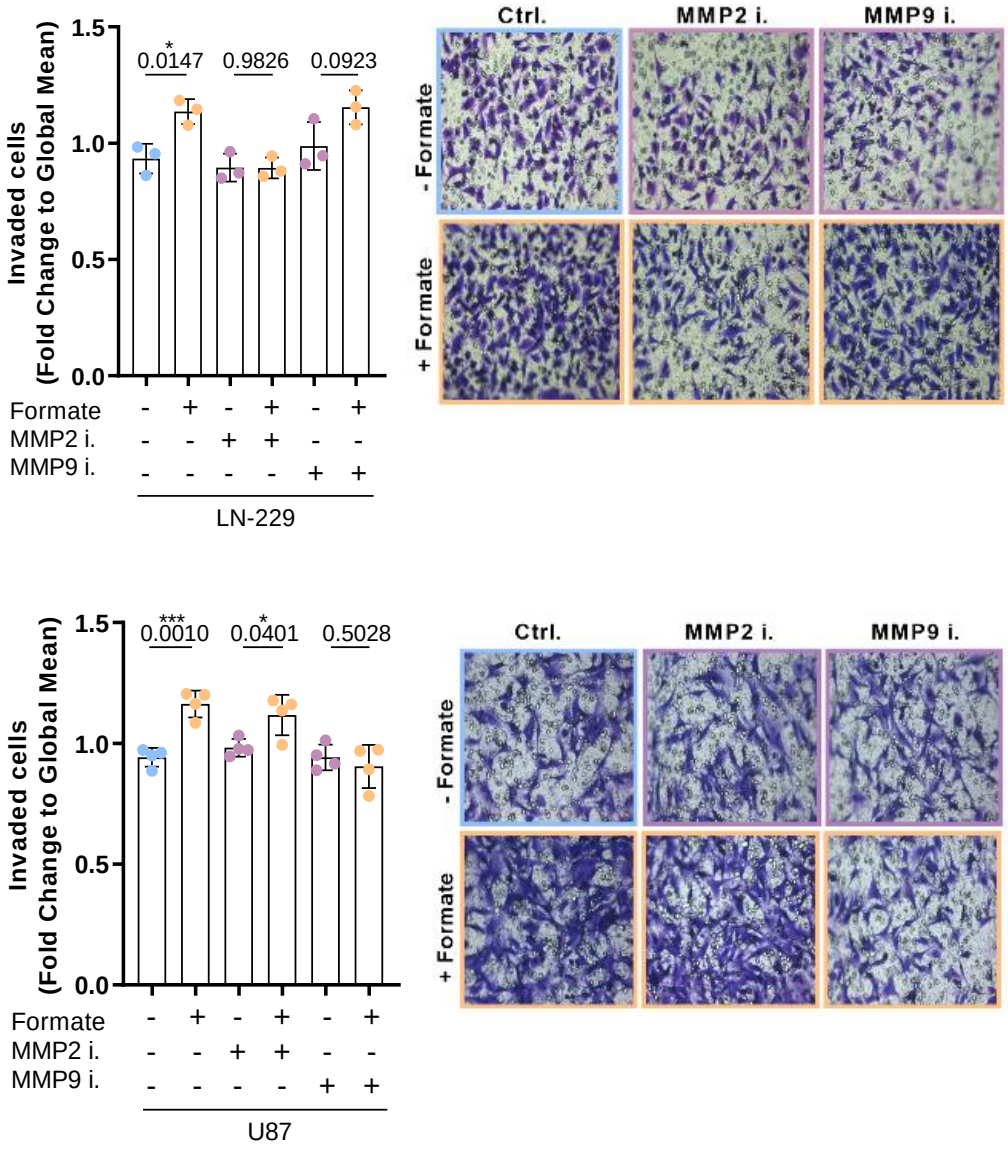

Figure 4.9: MMPi Prevents Formate-Induced Invasion
Left: Invasion of LN-229 or U87 cells treated for 24 hours with 500 µM Na-formate and 5 µM MMPi (MMP2 inhibitor or MMP9 inhibitor) assessed using ECM-collagen coated Boyden chambers. Each dot represents an independent experiment, the bars represent the mean, and the error bars visualize the standard deviation (SD). The data was evaluated using an unpaired *t*-test with Welch's correction. Right: Representative images of the Boyden chambers.

To study the physiological relevance of these findings, the invasion of LN-229 cells was assessed in an *ex vivo* brain slice assay upon simultaneous treatment with formate and MMP2i (**Figure 4.10**).

500 µM Na-formate significantly increased the cells' velocity. MMP2i alone did not affect the cancer cell velocity when compared to the untreated control cells. However, MMP2i prevented formate-induced invasion (**Figure 4.10**).

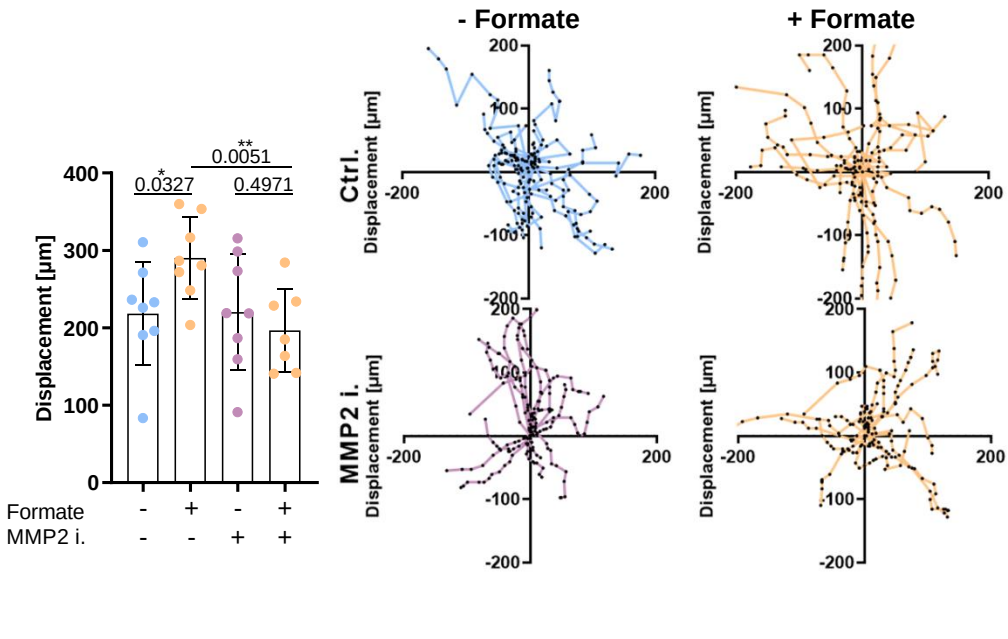

Figure 4.10: MMPi Prevents Formate-Induced Invasion in *Ex Vivo* Brain Slice Assays
Left: Displacement of LN-229 cells injected in *ex vivo* brain slice cultures. The cells were cultured during the entire experiment with either 500 µM Na-formate, 5 µM ARP100, or a combination of both. Each dot in the bar graph represents the average displacement of 15 cells, the bars represent the mean and the error bars visualize the standard deviation (SD). The data was evaluated using an unpaired *t*-test with Welch's correction. Right: Representative displacements of 10 cells. Dots and lines represent the trajectory of an individual cell.

These analyses demonstrate that formate promotes cancer cell invasion through active ECM degradation via MMP activation *in vitro* and *ex vivo*.

5 Targeting Fatty Acid Synthesis Inhibits Formate-Dependent Invasion

5.1 ROS, a Possible Intermediate in Formate-Induced Invasion

After discovering the role of MMP in formate-dependent invasion, the upstream signalling cascade of MMPs was studied.

It has previously been demonstrated that physiological levels of formate promote the release of mitochondrial ROS from mouse liver mitochondria (Young et al., 2017). Furthermore, the literature states that a mild increase in mitochondrial ROS promotes the invasiveness of cancer cells (Cheung et al., 2020; Porporato et al., 2014). Thus, we hypothesized that formate triggers a moderate increase in mitochondrial ROS, which in turn initiates a pro-invasive phenotype. This hypothesis was verified by performing *in vitro* Boyden chamber assays attempting to rescue formate-induced invasion through ROS scavenger supplementation. Three ROS scavengers (MitoTEMPO, Trolox and N-acetyl-l-cysteine (NAC)) were used and all of them successfully prevented the formate-dependent increase in invasion (**Figure 5.1**). The application of a ROS scavenger to untreated cells did not have an impact on invasion or proliferation (**Supplementary Figure 5.1**). This indicates that ROS scavenging specifically inhibits formate-induced invasion.

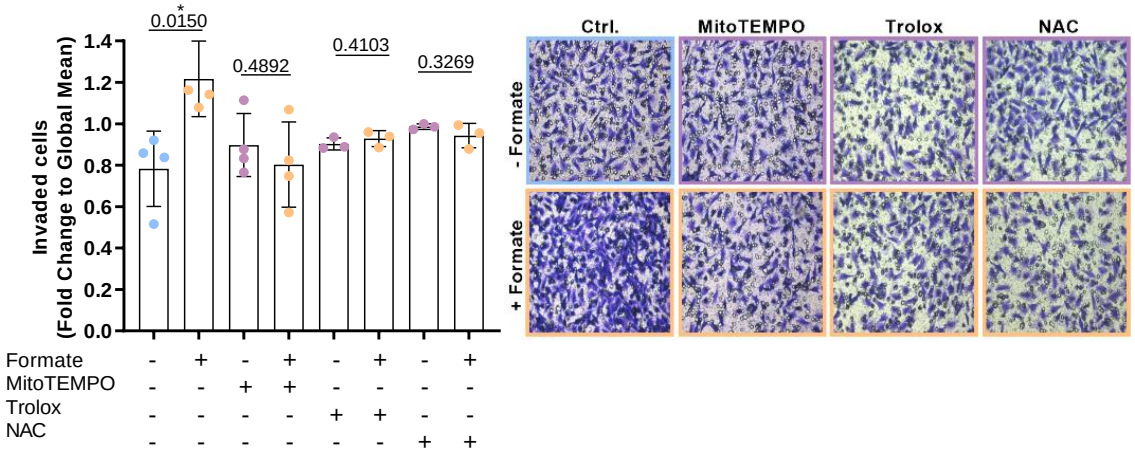

Figure 5.1: ROS Scavengers Prevent Formate-Induced Invasion
Left: Invasion of LN-229 cells treated for 24 hours with 500 µM Na-formate or a ROS scavenger (10 µM MitoTEMPO, 5 µM Trolox or 3 mM NAC) assessed using ECM-collagen coated Boyden chambers. Each dot represents an independent experiment, the bars represent the mean, and the error bars visualize the standard deviation (SD). The data was evaluated using an unpaired *t*-test with Welch's correction. Right: Representative images of the Boyden chambers.

Next, ROS levels were directly measured in the cell using three distinct fluorescent dyes (MitoSOX Red, 2',7'-dichlorofluorescein diacetate (DCFDA), and Amplex UltraRed) (**data not shown**). MitoSOX Red reagent, a novel mitochondrial fluorogenic dye, resulted in contradictory data across independent repeated experiments. Experiments using the cell-permeable ROS indicator DCFDA were also non-conclusive. Amplex UltraRed reagent, a sensitive and robust tool to detect cellular hydrogen peroxide, did not measure any changes probably due to the low variations of cellular ROS.

Thus, due to technical limitations, this line of research could not be followed up further. We concluded that ROS might be one factor that is involved in the signalling cascade of formate-induced invasion, but since we could not detect substantial changes in dependence of formate treatment, we aimed at identifying another direct molecular regulator by other unbiased approaches.

5.2 Formate Does Not Affect the Central Carbon Metabolism

To explore an alternative aspect of the formate-activated signalling cascade, the impact of formate on the central carbon metabolism was analysed. To study the central carbon metabolism, we performed stable isotope tracing experiments and inspected the oxygen consumption rate (OCR) through Seahorse Assays. However, no significant changes in metabolite steady-state levels, metabolic fluxes, or cellular respiration rate were detected (**Figure 5.2**).

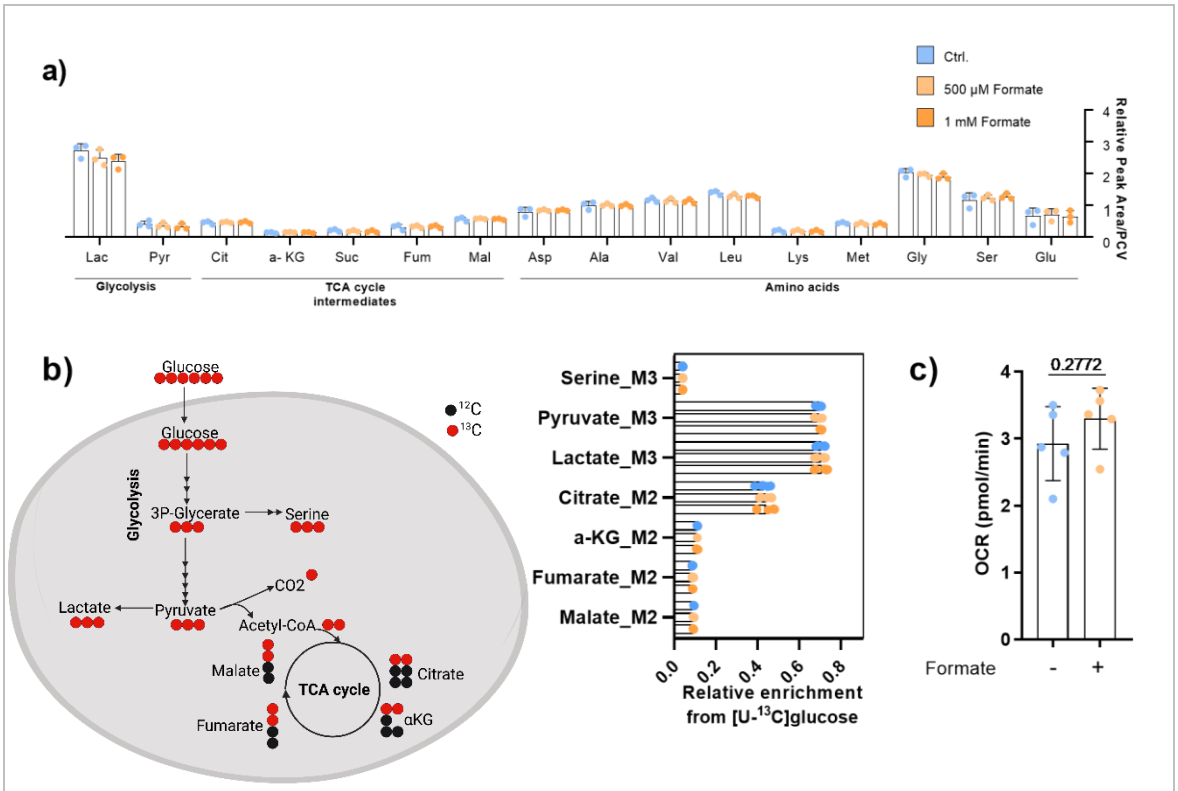

Figure 5.2: Formate Treatment Does Not Affect The Central Carbon Metabolism
a) Relative Peak Area normalised with respect to the packed cell volume (PCV) of different metabolites in LN-229 cells treated for 24 hours with either 500 µM or 1000 µM Na-formate. Each dot represents the mean of 3 independent experiments in triplicate wells. The error bars visualize the standard deviation (SD). The data was evaluated using an unpaired *t*-test with Welch's correction. b) On the left: Expected metabolic ^{13}C label pattern from [U-^{13}C]glucose tracer. On the right: Enrichment of representative isotopologues of serine, pyruvate, lactate, citrate, α-KG, fumarate, and malate upon [U-^{13}C]glucose tracer addition in response to 24 hours of 500 µM or 1000 µM formate treatment in LN-229 cells. Each dot represents the mean of 3 independent experiments in triplicate wells. The error bars visualize the standard deviation (SD). c) Basal cellular respiration of LN-229 cells in response to 24 hours of 500 µM formate treatment. Each dot represents an independent experiment composed of six technical replicates, the bars represent the mean, and the error bars visualize the standard deviation (SD).

5.3 Formate Promotes a Lipid Signature

As no direct changes were identified in previous experiments, potential signalling pathways were profiled by analysing the RNAseq dataset.

The gene set enrichment analysis (GSEA) pinpointed several specific subsets of the transcriptome that were highly affected by formate supplementation, namely “cholesterol homeostasis”, “androgen response”, “estrogen early response” and “estrogen late response” (**Figure 5.3**). As androgens and estrogens are made from cholesterol they all route back to the acetyl-CoA metabolism and the mevalonate pathway. The complete GSEA analysis can be found in the “Supplementary Figure Section” (**Supplementary Figure 5.2**).

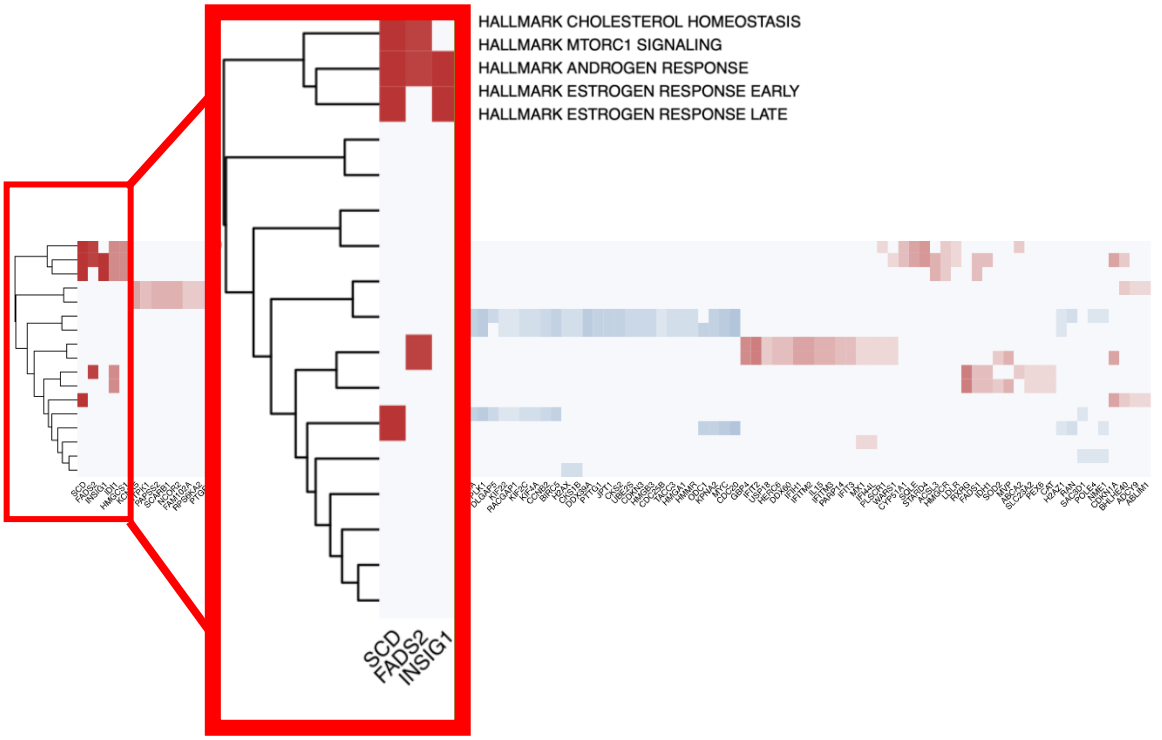

Figure 5.3: Fatty Acid and Cholesterol Genes are Increased After Formate Supplementation
Gene set enrichment analysis (GSEA) representing LN-229 cells treated for 24 hours with 500 µM formate compared to LN-229 control cells measured using RNAseq data.

Whereas 8 hours of formate treatment had only a minor impact on the cells’ transcriptome (**data not shown**), 24 hours of formate profoundly altered the gene expression levels. When depicting the RNAseq data as a volcano blot, several highly expressed genes sharing common biological functions were identified in response to formate treatment: fatty acid desaturase 2 (*FADS2*), stearoyl-CoA desaturase-1 (*SCD*), insulin-induced gene 1 (*INSIG1*), fatty acid synthase (*FASN*), and sterol regulatory-element binding 1 & 2 (*SREBP 1/2*). Notably, all of these genes play an important role in lipid metabolism (**Figure 5.4**).

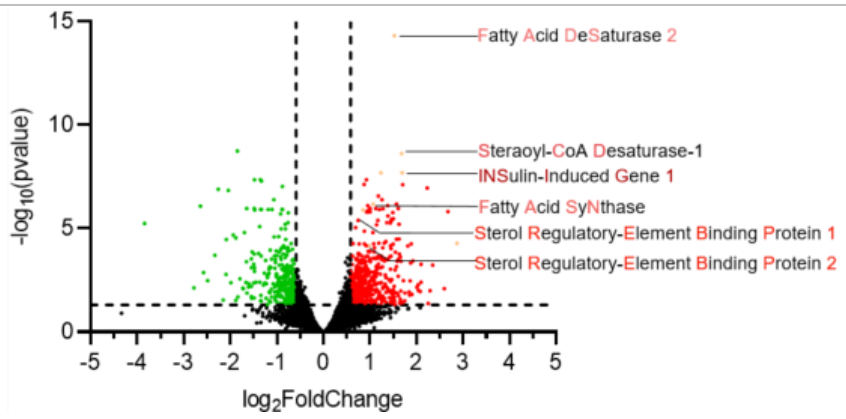

Figure 5.4: *FADS2*, *SCD*, *INSIG1* and *FASN* are Upregulated after Formate Treatment
Volcano Blot representing LN-229 cells treated for 8 or 24 hours with 500 µM formate compared to LN-229 control cells measured using RNAseq data.

In summary, the RNAseq data analysis revealed a relationship between formate supplementation and lipid synthesis.

5.4 Formate Promotes Fatty Acid Synthesis *In Vitro*

To analyse the effect of formate on the lipid metabolism, the expression levels of the genes related to fatty acid synthesis were measured by an RT-qPCR (**Figure 5.5**). Formate increased the gene expression of *SCD*, *SREBP1/2*, *INSIG1*, *FADS2*, *FFAR1 (*free fatty acid receptor 1*)* and *FASN* in LN-229 cells after 24 hours of formate treatment. *SCD*, *SREBF*, *INSIG* were also highly upregulated after formate treatment in the MDA-MB-468 cells. No changes were detected in the U87 cells except for the *FFAR1* gene, which was upregulated after formate supplementation. In line with the RNAseq data, no significant differences in the gene expression level were observed after 8 hours of formate treatment.

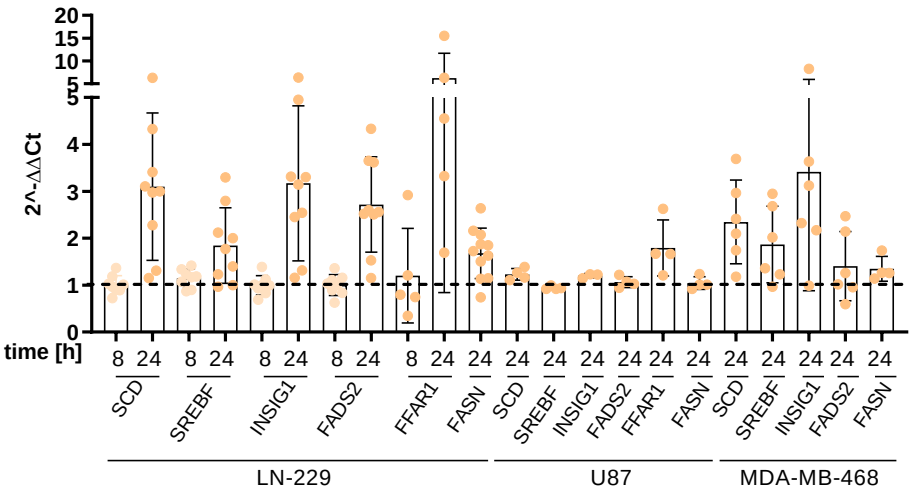

Figure 5.5: Formate Promotes Enhanced Expression of Lipid Metabolism Genes
mRNA expression from *SCD*, *SREBF, INSIG1*, *FADS2*, *FFAR1, and FASN* in LN-229, U87, and MDA-MB-468 cells that were treated either for 8 or 24 hours with 500 µM formate. The results are shown as $2^{-\Delta\Delta Ct}$, representing the relative fold gene expression with respect to untreated cells. Each dot represents a biological replicate, the bars represent the mean, and the error bars visualize the standard deviation (SD). The fold change of 1, which represents that there is 100 % as much gene expression as in the control is represented by a black dotted line.

To further validate the assumption that formate promotes fatty acid synthesis, we measured the protein level of the fatty acid synthase (FASN) in the LN-229 cells. FASN, a key enzyme involved in lipogenesis, has been described to be overexpressed in many cancers. Interestingly a dynamic fluctuation of FASN after 500 µM of Na-formate treatment was measured. Upon 30 minutes of treatment, a significant increase (*p=0.0134*) in FASN level was detected. Yet, no changes were measured after 1 hour of treatment. An increase could again be measured after 24 hours of formate treatment (*p=0.0040*) (**Figure 5.6**). All in all, formate treatment impacts the dynamic nature of FASN.

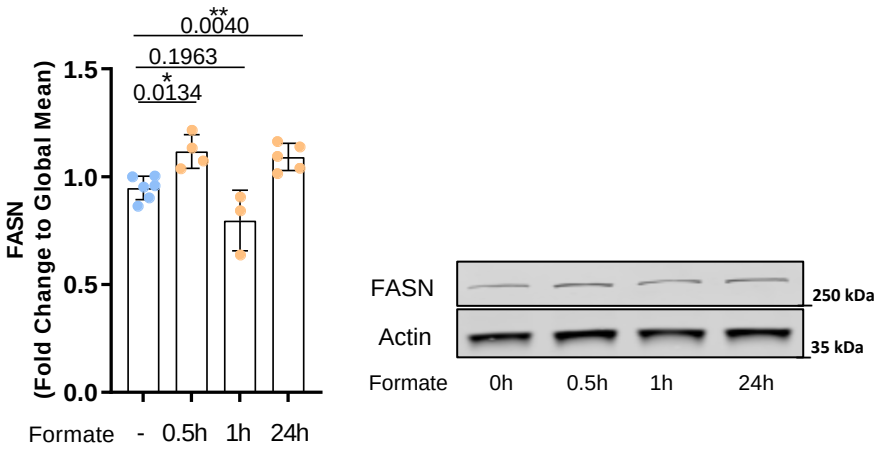

Figure 5.6: Formate Impacts the Dynamic Nature of FASN
Expression of FASN in LN-229 cells treated with 500 µM formate for different durations (0, 0.5, 1, and 24 hours). The signal intensity of FASN was quantified with respect to the signal intensity of β-actin. Each dot represents an independent experiment, the bars represent the mean, and the error bars visualize the standard deviation (SD). The data was evaluated using an unpaired *t*-test with Welch's correction.

To explore the formate-induced fatty acid synthesis in a direct approach, stable-isotope-assisted metabolic flux analysis was used. Although, the expression of genes implicated in cholesterol synthesis was identified to be highly upregulated after formate addition (**Figure 5.3**), cholesterol biosynthesis was negligible (~5%) in our tracing experiment (**Figure 5.7**). Albeit, LN-229 cells were cultured using charcoal-stripped FBS to enforce lipid synthesis and were incubated simultaneously with [U-^{13}C]glucose and [U-^{13}C]glutamine to increase overall labelling, no meaningful cholesterol labelling was obtained. Even though the slight right shift of the curve indicates increased labelling, the overall labelling remains very little (**Figure 5.7**).

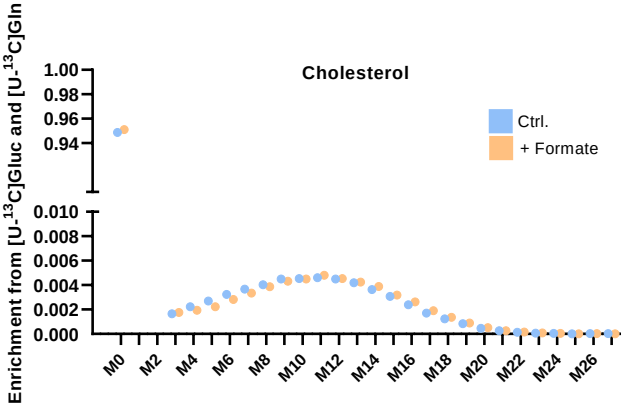

Figure 5.7: Cholesterol Biosynthesis was Negligible after Formate Treatment
Representative graph of isotopologue enrichment of cholesterol after [U-^{13}C]Gluc and [U-^{13}C]Gln tracer addition in response to 72 hours of 500 µM formate treatment in LN-229 cells. The experiment was repeated three times with triplicate wells.

As a direct measurement of cholesterol biosynthesis was infeasible, the phenotypic role of cholesterol synthesis in formate-induced invasion was studied indirectly using Boyden chamber assays. The impact of two commercially available statins (Simvastatin and Fatostatin) on formate-induced invasion was evaluated. Statins, also known as β-hydroxy β-methylglutaryl-CoA *(*HMG-CoA*)* reductase inhibitors, present a class of cholesterol-lowering medications that inhibit the mevalonate pathway (**Illustration 31**).

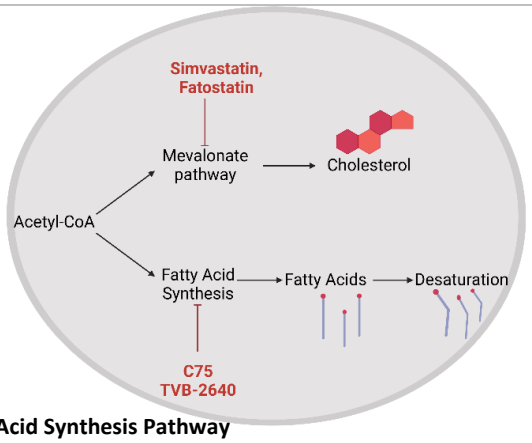

Illustration 31: Cholesterol and Fatty Acid Synthesis Pathway
Schematic representation of the mevalonate and fatty acid synthesis pathway. Illustration created with BioRender.com

Both cholesterol biosynthesis inhibitors, Simvastatin and Fatostatin prevented formate-induced invasion in LN-229 cells (**Figure 5.8**). Of note, both inhibitors affected the basal invasion capacity of LN-299 cells. This suggests that cholesterol synthesis plays a general role in invasion and formate-induced invasion. However, as a direct assessment of cholesterol *de novo* biosynthesis was not feasible, this hypothesis was not examined in further detail.

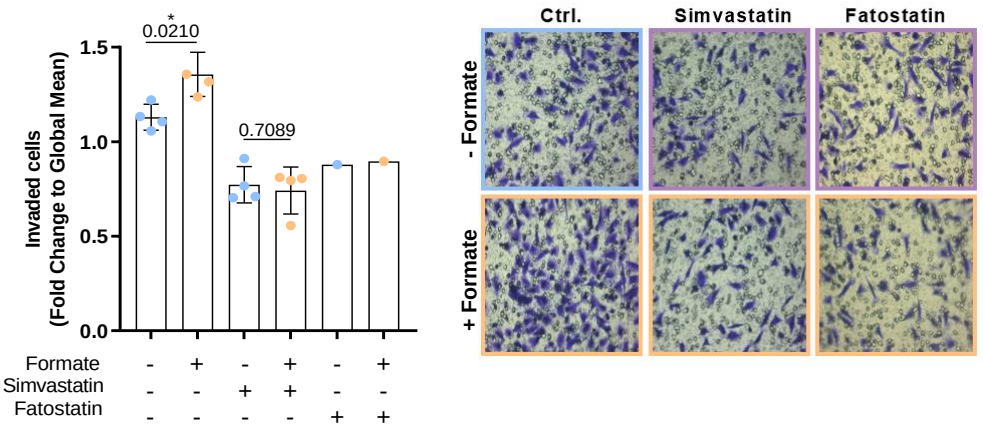

Figure 5.8: Cholesterol Biosynthesis Inhibitors Prevent (Formate-Induced) Invasion
Left: Invasion of LN-229 cells treated for 24 hours with 500 µM formate and/or a cholesterol biosynthesis inhibitor (1 µM Simvastatin or 2 µM Fatostatin) assessed using ECM-collagen coated Boyden chambers. Each dot represents an independent experiment, the bars represent the mean, and the error bars visualize the standard deviation (SD). The data was evaluated using an unpaired *t*-test with Welch's correction. Right: Representative images of the Boyden chambers.

Next, we analysed the impact of formate on fatty acid synthesis through a stable-isotope-assisted metabolic flux analysis.

Palmitate, a saturated fatty acid containing 16 carbons, is the end product of fatty acid synthesis. Other fatty acids of various lengths and saturations are derived from palmitate by elongation, oxidation, or desaturation (Yao et al., 2016). Given its central position in fatty acid metabolism, the analysis of palmitate by mass spectrometry was expected to provide some important insights into formate-induced fatty acid synthesis. However, mass spectrometry overestimates unlabelled palmitate levels in cells due to high background contamination of palmitate in plastic lab equipment. Saturated fatty acids are often used as lubricants during plastic production which can lead to a six-fold palmitate overestimation (Yao et al., 2016). Due to this unfortunate experimental limitation, the impact of formate on fatty acid synthesis was thus measured based on the monounsaturated form of palmitate: palmitoleic acid (hexadecenoic acid).

A significant increase in labelled palmitoleic acid was noted after 72 hours of formate treatment for different cancer cell lines (LN-229, U87, and MDA-MB-468) (**Figure 5.9**) (**Supplementary Figure 5.3**). In all cell lines, a decrease of unlabelled M0 palmitoleic acid after formate treatment implies an increased ^{13}C incorporation as a result of an increase in the relative flux from ^{13}C labelled glucose into fatty acids.

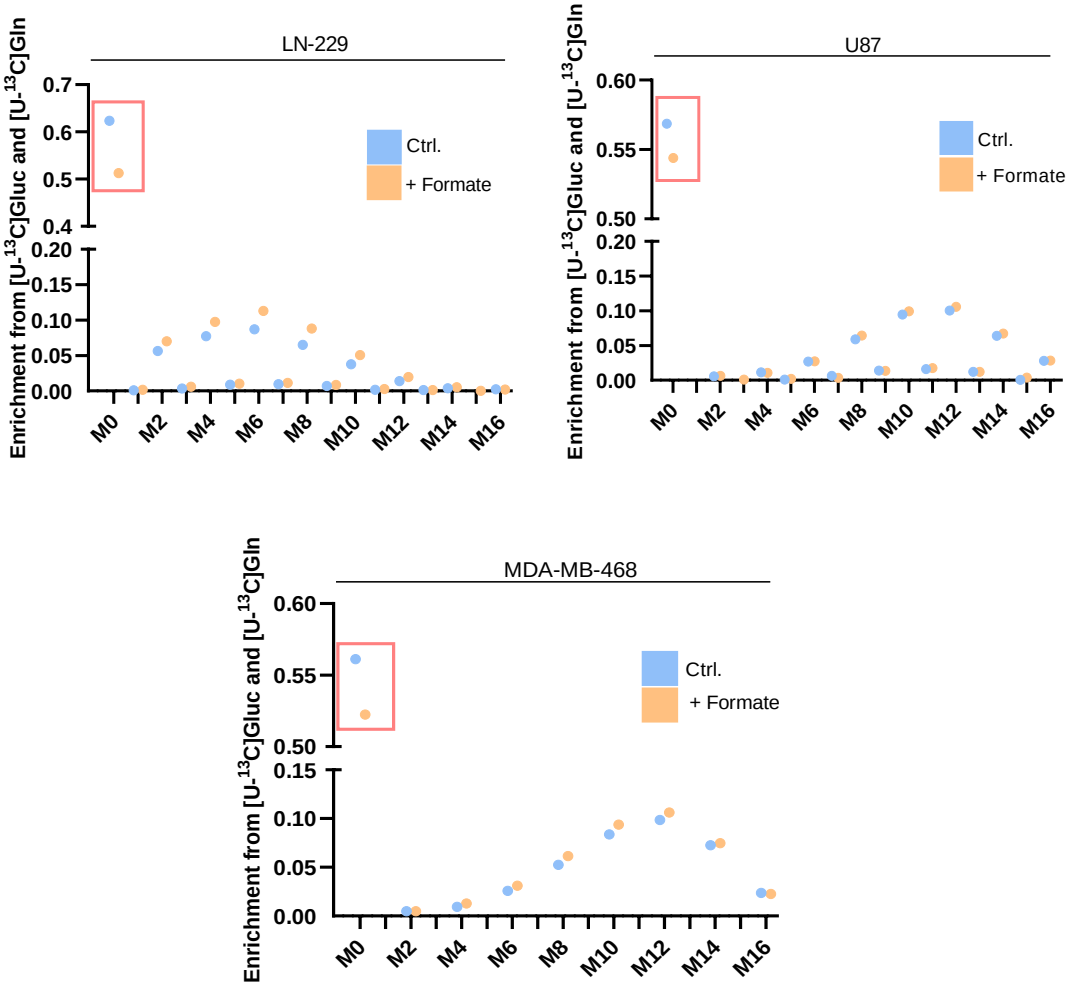

Figure 5.9: Formate Promotes Fatty Acid Synthesis
Representative graph of isotopologue enrichment of hexadecenoic acid after [U-^{13}C]glucose and [U-^{13}C]glutamine tracer supplementation in response to 72 hours of 500 µM formate treatment in LN-229, U87, and MDA-MB-468 cells. The experiment was repeated eight times with triplicate wells.

Hence, these results show that formate treatment promotes fatty acid synthesis *in vitro*.

5.5 Targeting FAS Inhibits Formate-Dependent Invasion

To determine the functional relevance of the previous measurement, the effect of fatty acid synthesis (FAS) inhibition on formate-induced invasion was assessed in Boyden chamber assays (**Figure 5.10**). Two FASN inhibitors (C75 and TVB-2640) successfully prevented formate-dependent invasion. Notably, the application of C75 to untreated cells significantly decreased the basal invasive capacity of the studied cancer cells. The application of TVB-2640, which is currently used in phase 2 clinical trials for non-small cell lung carcinomas (Gerber, 2019) and GBM (W. Kelly et al., 2020), did not cause a decrease in the basal invasion rate. Furthermore, the proliferation rate was not affected by the used concentrations of C75 and TVB-2640, indicating that the observed decrease in invasiveness is not the result of a decreased proliferation (**Supplementary Figure 5.4**).

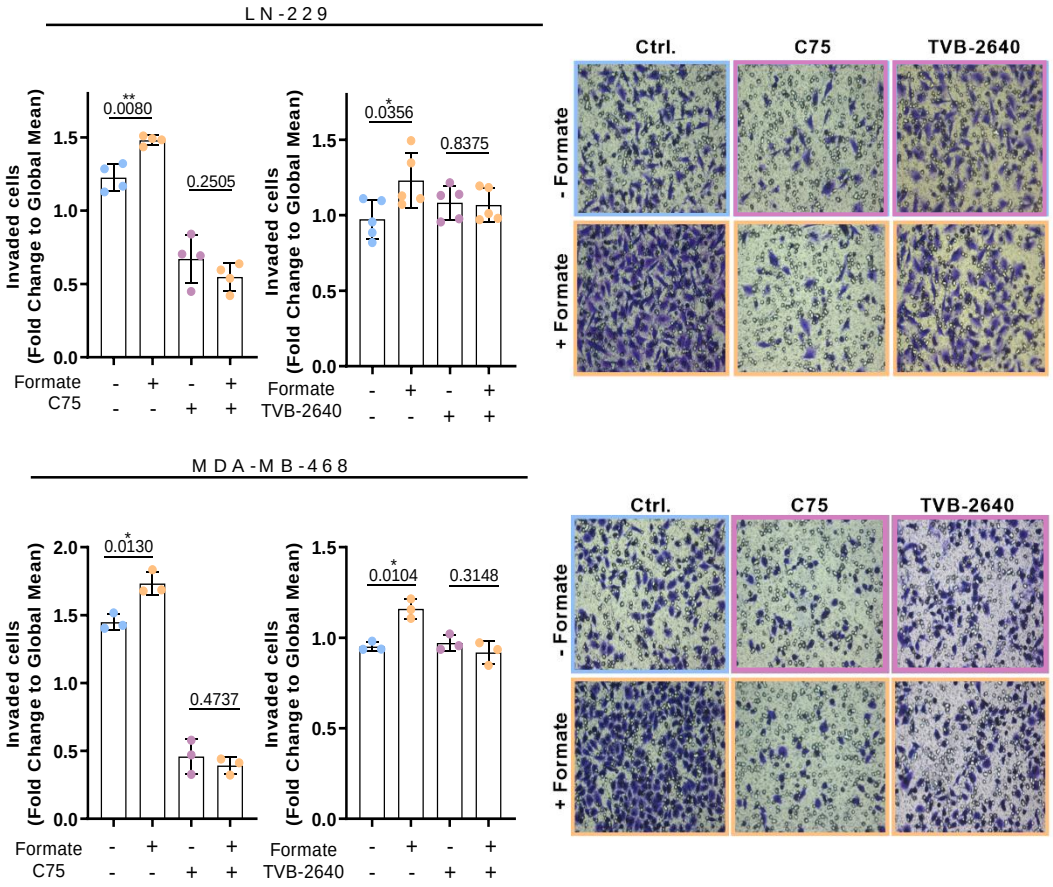

Figure 5.10: Targeting FAS Inhibits Formate-Dependent Invasion *In Vitro*
Left: Invasion of LN-229 and MDA-MB-468 cells treated for 24 hours with 500 µM Na-formate and a FASN inhibitor (10 µM C75 and 10 µM TVB-2640) assessed using ECM-collagen coated Boyden chambers. Each dot represents an independent experiment, the bars represent the mean, and the error bars visualize the standard deviation (SD). The data was evaluated using an unpaired *t*-test with Welch's correction. Right: Representative images of the Boyden chambers.

To strengthen the hypothesis that TVB-2640 prevents formate-induced invasion through FASN inhibition, we analysed the impact of the simultaneous treatment of formate and TVB-2640 on the palmitoleic acid synthesis using a stable-isotope-assisted metabolic flux analysis (**Figure 5.11**). The addition of TVB-2640 significantly inhibited palmitoleic acid synthesis. Compared to untreated cells, where almost 60% of palmitoleic acid were labelled after 72 hours, no labelling could be measured after TVB-2640 treatment even in the presence of formate (**Figure 5.11**).

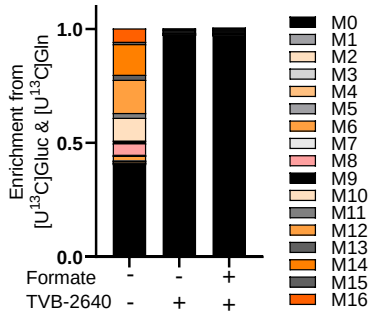

Figure 5.11: TVB-2640 Prevents Formate-Induced Fatty Acid Synthesis
Representative graph of isotopologue enrichment of hexadecenoic acid after [U-^{13}C]glucose and [U-^{13}C]glutamine tracer supplementation in response to 72 hours of 500 µM formate and 10 µM TVB-2640 treatment in LN-229 cells.

All in all, our experiments confirmed that TVB-2640 inhibits fatty acid synthesis in the LN-229 cells. Furthermore, we showed that TVB-2640 simultaneously prevents formate-induced invasion through FASN inhibition.

De novo fatty acid synthesis is associated with membrane biosynthesis and fluidity. Using a commercially available kit, the membrane fluidity of LN-229 cells was assessed by investigating the short-range lateral diffusion of lipophilic pyrene probes (**Figure 5.12**). However, no change in the fluidity or rigidity of the cancer cells was measured after formate treatment. In addition, cholesterol supplementation did not induce any changes, which calls the sensitivity of the used kit into question.

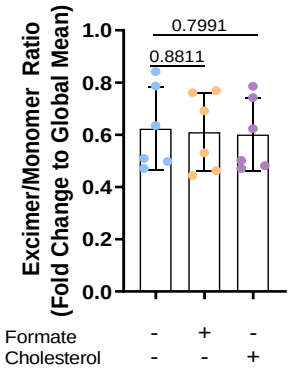

Figure 5.12: Membrane Fluidity is Not Impacted by Formate
Membrane fluidity measured based on the excited dimer formation (excimer) of lipophilic pyrenes. The LN-229 cells were treated for 24 hours with either 500 µM Na-formate or 259 ng/ml cholesterol. The assessment was performed using the abcam fluidity kit. Each dot represents an independent experiment, the bars represent the mean, and the error bars visualize the standard deviation (SD).

To investigate whether fatty acid synthesis activity is an upstream regulator of MMP expression, the *MMP2* gene expression in LN-229 cells was analysed by RT-qPCR after a 24 hours TVB-2640 treatment. TVB-2640 treatment did prevent the increased *MMP2* expression after formate supplementation (**Figure 5.13**). This indicates that *FASN* is involved in transmitting the formate-dependent signal towards an increased *MMP2* expression. *MMP9*, which takes the role of a negative control in LN-229 cells, remained unaffected by either treatment condition.

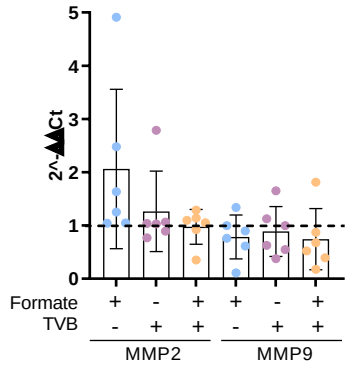

Figure 5.13: FASN Inhibition Prevents Formate-Dependent MMP2 Upregulation
mRNA expression from *MMP2* and *MMP9* in LN-229 cells which were treated for 24 hours with 500 µM formate and 10 µM TVB-2640. The results are presented as $2^{-\Delta\Delta Ct}$, representing the relative fold gene expression with respect to untreated cells. Each dot represents a biological replicate, the bars represent the mean, and the error bars visualize the standard deviation (SD). The fold change of 1, which represents the gene expression of the control cells, is represented by a black dotted line.

Finally, the interplay between formate-induced invasion and fatty acid synthesis inhibition was studied in a physiologically relevant e*x vivo* brain slice culture using the LN-229 cells (**Figure 5.14**). Formate supplementation significantly (p=0.0327) increased the velocity of LN-229 cells in the *ex vivo* brain slices. Aligned with the *in vitro* observations, the exclusive treatment with TVB-2640 did not impact the velocity of untreated cells, but it prevented formate-induced invasion (**Figure 5.14**).

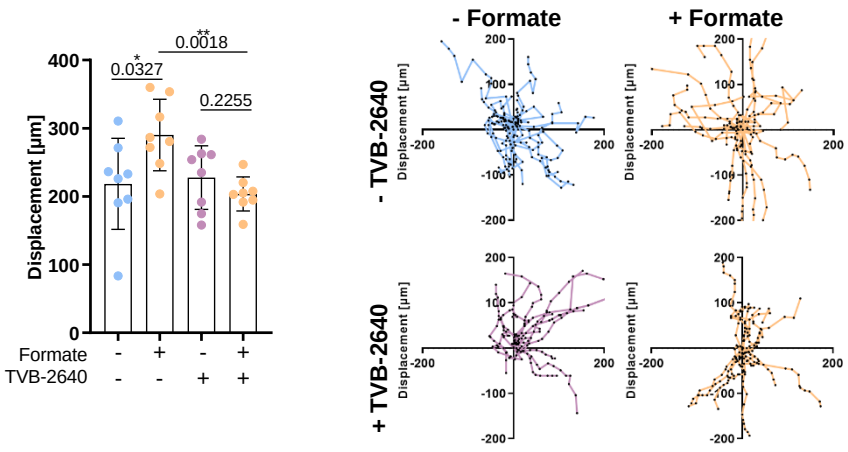

Figure 5.14: Targeting FAS Inhibits Formate-Dependent Invasion *Ex Vivo*
Left: Displacement of LN-229 cells injected into an *ex vivo* brain slice culture. The cells were cultured during the entire experiment with either 500 µM formate, 10 µM TVB-2640, or a combination of both. Each dot in the bar graph represents the average displacement of 15 cells, the bars represent the mean, and the error bars visualize the standard deviation (SD). The data was evaluated using an unpaired *t*-test with Welch's correction. Right: Representative displacements of 10 cells. Dots and lines represent the trajectory of an individual cell.

The obtained results indicate that formate promotes fatty acid synthesis which in turn induces a pro-invasive cellular phenotype.

6 AMPK Supports Formate-Dependent Invasion

6.1 Formate is a Potential Activator of AMPK

Although fatty acid synthesis (FAS) was uncovered as an important mechanistic player in formate-dependent invasion, the question, of how extracellular formate promotes FAS remained open. mTORC1, a known upstream regulator of cholesterol and lipid metabolism (Laplante and Sabatini, 2009; Porstmann et al., 2009), was identified as the top hit in our GSEA analysis (**Figure 5.3**). To study the protein complex mTORC1, we investigated the protein expression and phosphorylation of mTOR, a catalytic subunit of mTORC1 (**Figure 6.1**). However, the resulting Western Blots did not show any significant changes in mTOR expression or phosphorylation.

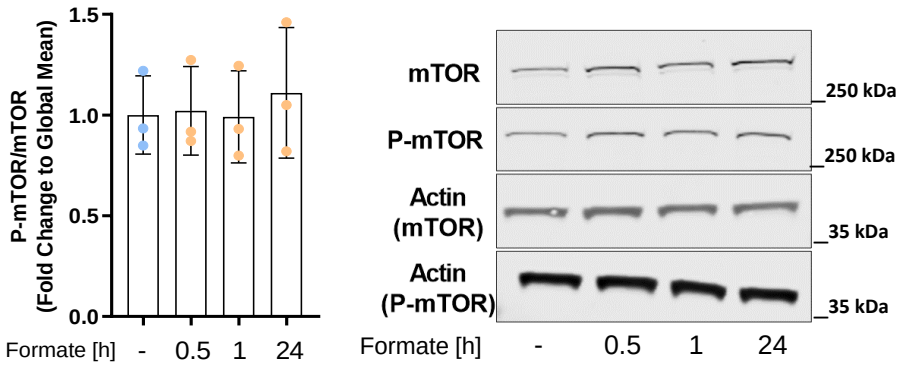

Figure 6.1: mTOR Expression and Phosphorylation are Unaffected by Formate
Expression of mTOR and the corresponding phosphorylated protein in LN-229 cells treated with 500 µM Na-formate for different durations (0, 0.5, 1, and 24 hours). The signal intensity of P-mTOR/mTOR has been quantified with respect to the signal intensity of β-actin. Each dot represents an independent experiment, the bars represent the mean, and the error bars visualize the standard deviation (SD).

As mTORC1 was not affected by formate, the phosphorylation status of acetyl-CoA carboxylase (ACC), a downstream target of mTORC1, was assessed at different time points. ACC is a key regulatory enzyme, which catalyses the irreversible carboxylation of acetyl-CoA to malonyl-CoA, the key substrate for fatty acid biosynthesis (Hardie and Pan, 2002) (**Illustration 32**).

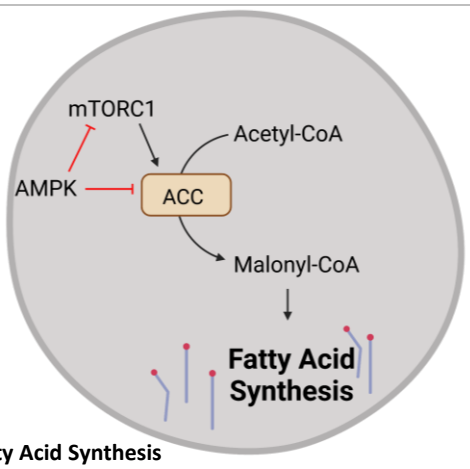

Illustration 32: ACC Regulates Fatty Acid Synthesis
ACC is a key regulatory enzyme that catalyses the irreversible carboxylation of acetyl-CoA to malonyl-CoA, the key substrate for fatty acid biosynthesis. Illustration created with BioRender.com

No differences in ACC expression and phosphorylation were noted after formate treatment of LN-229 cells. 2-deoxy-D-glucose (2DG), which indirectly induces phosphorylation of ACC, served as a positive control (**Figure 6.2**). Similar results were obtained for U87 and MDA-MB-468 cells (**Supplementary Figure 6.1**).

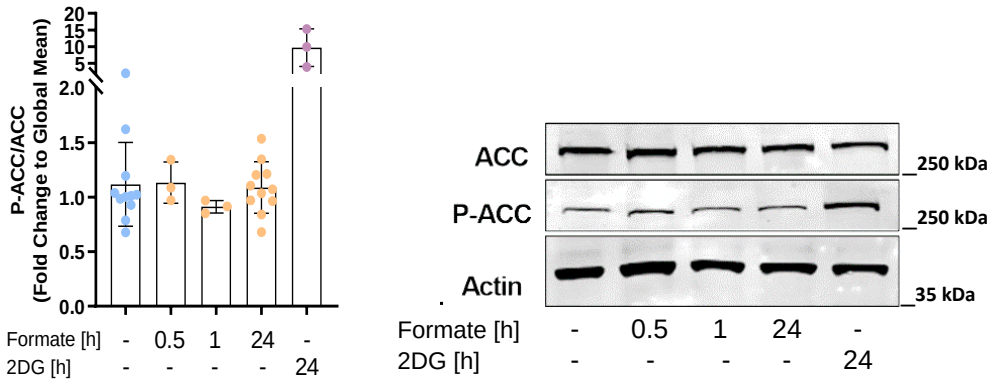

Figure 6.2: ACC Expression and Phosphorylation are Not Affected by Formate
Expression of ACC and the corresponding phosphorylated protein in LN-229 cells treated with 500 µM formate for different durations (0, 0.5, 1, and 24 hours). The signal intensity of P-ACC and ACC was quantified with respect to the signal intensity of β-actin. Each dot represents an independent experiment, the bars represent the mean, and the error bars visualize the standard deviation (SD).

Interestingly, the phosphorylation of the negative upstream regulator of ACC, namely the AMP-activated protein kinase (AMPK) (**Illustration 32**), was slightly increased in LN-229 and MDA-MB-468 cells after 24 hours of formate treatment (**Figure 6.3**). No major changes were noticed in U87 cells. 2DG served as a positive control.

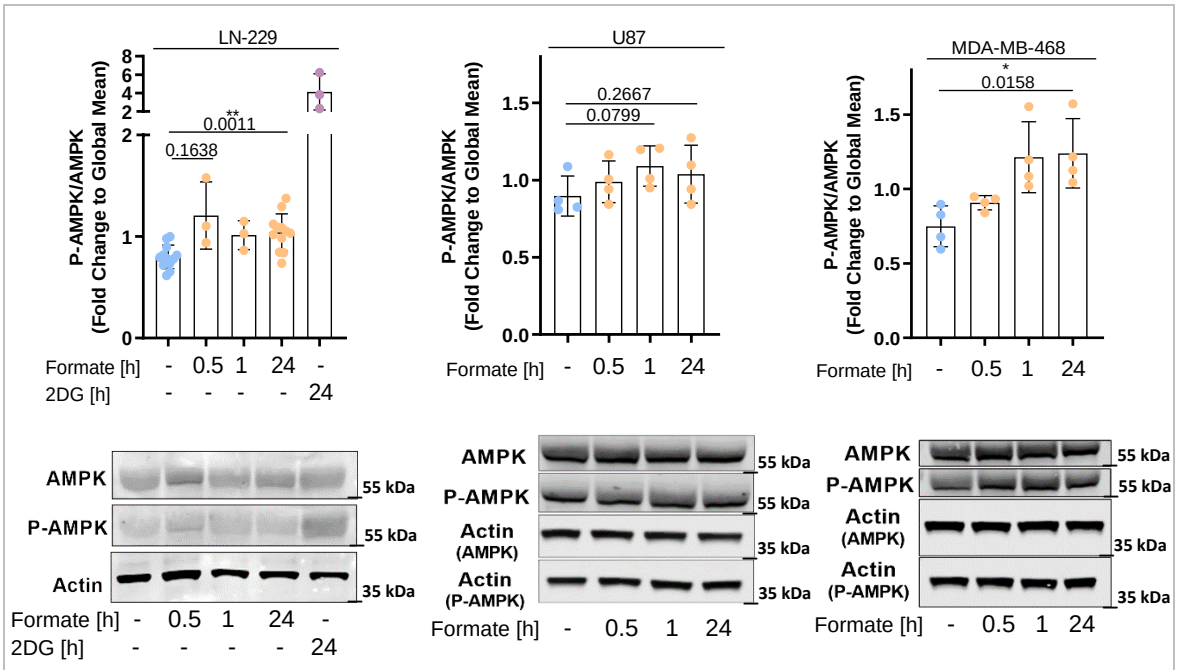

Figure 6.3: AMPK Phosphorylation is Slightly Impacted after Formate Treatment
Expression of AMPK and the corresponding phosphorylated protein in LN-229, U87, and MDA-MB-468 cells treated with 500 µM formate for different durations (0, 0.5, 1, and 24 hours). The signal intensity of P-AMPK and AMPK was quantified with respect to the signal intensity of β-actin. Each dot represents an independent experiment, the bars represent the mean, and the error bars visualize the standard deviation (SD). The data was evaluated using an unpaired *t*-test with Welch's correction.

6.2 AMP Synthesis Is Supported by Exogenous Formate

Due to the subtle increase of AMPK phosphorylation, a possible mechanistic link between formate and AMPK has been analysed. The carbon backbone of adenosine monophosphate (AMP), a strong physiological activator of AMPK (Gowans et al., 2013), originates from two molecules of formate, one molecule of glycine, and one molecule of CO_2 (**Illustration 33**) (Brosnan and Brosnan, 2016). This leads to the hypothesis that formate supplementation enhances purine *de novo* synthesis and so indirectly affects the equilibrium of purine bases and purine nucleotides.

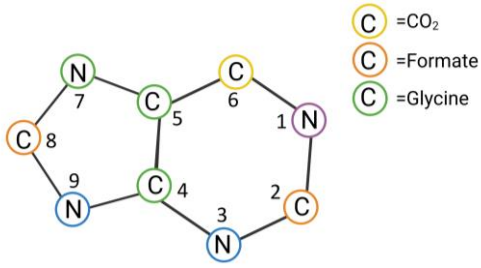

Illustration 33: Purine Backbone
N1 arises from the amino group of aspartate; C2 and C8 originate from formate; N3 and N9 come from the amide (NH_2) group of glutamine; C4, C5, and N7 are contributed from glycine; and C6 comes from CO_2. Illustration created with BioRender.com.

To characterize purine *de novo* flux, an [U-^{13}C]glucose tracing was performed after the addition of unlabelled exogenous formate (**Illustration 34**). Ribose flux from the pentose phosphate pathway (PPP) into nucleotides results in an M+5 labelling in AMP. Furthermore, adenine (purine ring lacking the ribose residue) labelling sheds light on the origin of the incorporated formate. The carbons of adenine derive from one molecule of glycine, two molecules of formate, and one molecule of CO_2. As glucose-derived serine *de novo* synthesis gives rise to labelled 1C units, this experimental approach allowed to monitor the relative flux of endogenous ^{13}C labelled 1C units with the relative flux of unlabelled formate.

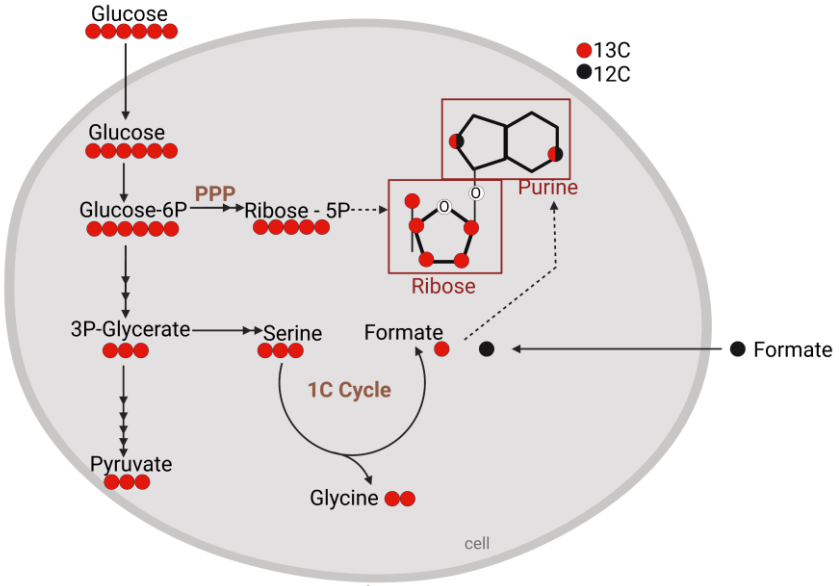

Illustration 34: *De Novo* Purine Synthesis from a [U-^{13}C]Glucose Tracer
Schematic depiction of the interdependence of metabolic pathways (Glycolysis, Pentose Phosphate Pathway, and 1C Cycle), as well as the expected metabolic ^{13}C label pattern from the [U-^{13}C]glucose tracer. Illustration created with BioRender.com.

A time-dependent increase in M+5 labelling in AMP was monitored after formate treatment. Within 24 hours, MDA-MB-468 cells showed a significant increase (p=0.0176) and LN-229 cells a slight increase (p=0.077) in M+5 labelling. However, the purine biosynthesis in U87 cells was not affected by the formate supplementation (**Figure 6.4**). Nonetheless, these results suggest that exogenous formate promotes purine biosynthesis from glucose.

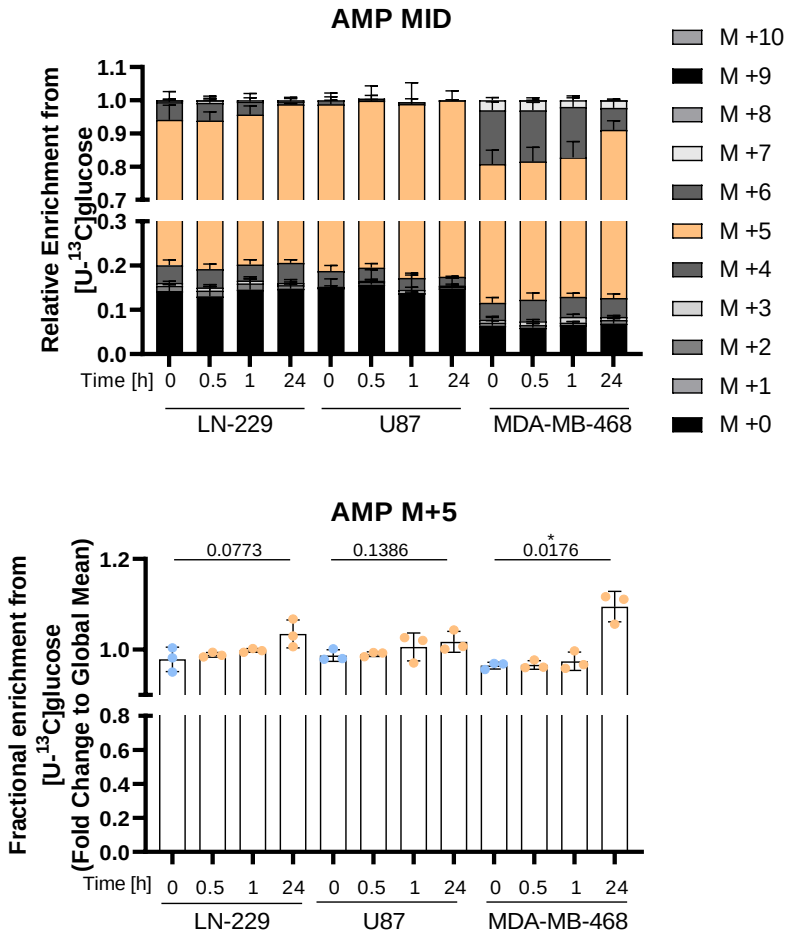

Figure 6.4: Formate Promotes AMP *De Novo* Biosynthesis
Top: Mass Isotopologue Distribution (MID) of intracellular AMP after the addition of [U-^{13}C]glucose tracer in LN-229, U87, and MDA-MB-468 cells in response to different durations (0, 0.5, 1, and 24 hours) of 500 µM formate treatment. Each bar represents the mean of 3 independent experiments in triplicate wells. The error bars visualize the standard error of the mean (SEM). Low: Enrichment of M+5 isotopologues of AMP after the addition of [U-^{13}C]glucose tracer in LN-229, U87, and MDA-MB-468 cells in response to 0, 0.5, 1, or 24 hours of 500 µM formate treatment. Each dot represents the mean of 3 independent experiments in triplicate wells. The error bars visualize the standard error of the mean (SEM). The data was evaluated using an unpaired *t*-test with Welch's correction.

As AMP, ADP, and ATP are closely related, it was not surprising that a similar labelling pattern was observed in all three nucleotides (**Supplementary Figure 6.2**).

To investigate if the unlabelled formate (^{12}C formate) was incorporated into the nucleotides, the labelling pattern of adenine was evaluated. An increase of M+0 labelling (corresponding to a decreased labelled fraction) hints at the incorporation of exogenous unlabelled formate into purine nucleotides. No difference in the labelling pattern was noted after 0.5 or 1 hour of formate treatment, but a significant increase of M+0 was measured in all three tested cell lines (LN-229, U87, and MDA-MB-468) after 24 hours of formate treatment (**Figure 6.5**).

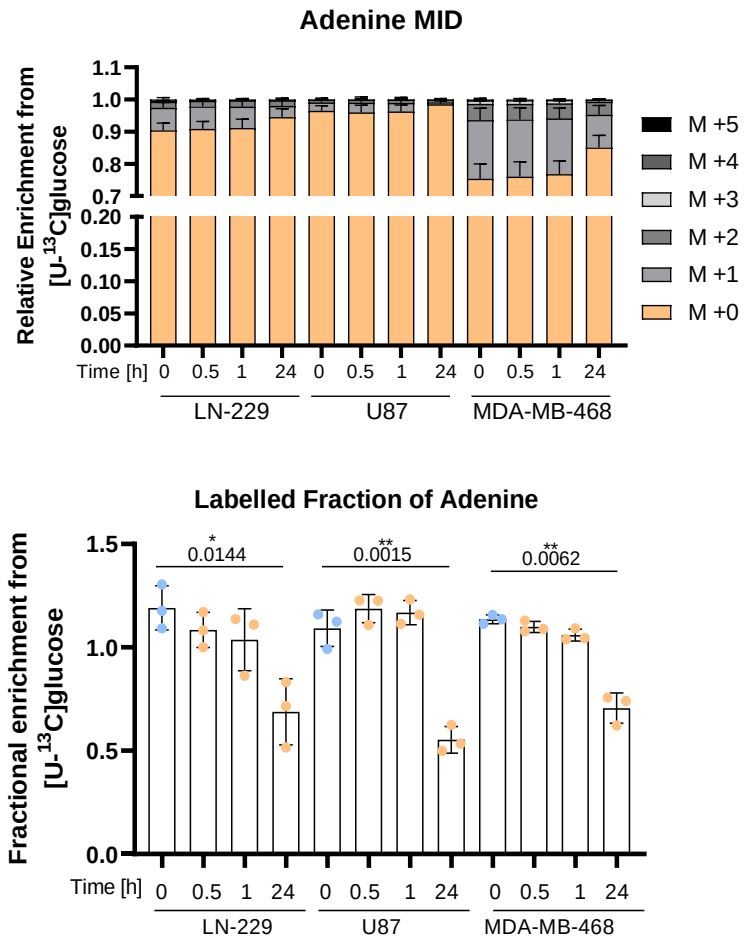

Figure 6.5: Exogenous Formate is Integrated into Purines
Top: Mass Isotopologue Distribution (MID) of intracellular adenine after the addition of [U-^{13}C]glucose tracer in LN-229, U87, and MDA-MB-468 cells in response to different durations (0, 0.5, 1, and 24 hours) of 500 µM formate treatment. Each bar represents the mean of 3 independent experiments in triplicate wells. The error bars visualize the standard error of the mean (SEM). Low: Labelled fraction of adenine upon [U-^{13}C]glucose tracer in LN-229, U87, and MDA-MB-468 cells in response to 0, 0.5, 1, or 24 hours of 500 µM formate treatment. Each dot represents the mean of 3 independent experiments in triplicate wells. The error bars visualize the standard error of the mean (SEM). The data was evaluated using an unpaired *t*-test with Welch's correction**.**

To directly measure the extracellular formate incorporation into purines, the previous experiment was repeated with inverted tracer supplementation. This time, the cells were cultured in DMEM with unlabelled glucose and treated for varying durations with 500 µM [U-^{13}C]formate (**Illustration 35**). An M+1 and M+2 increase in AMP MID indicates the incorporation of exogenous formate. No labelling indicates that all 1C units originate from the intracellular 1C metabolism.

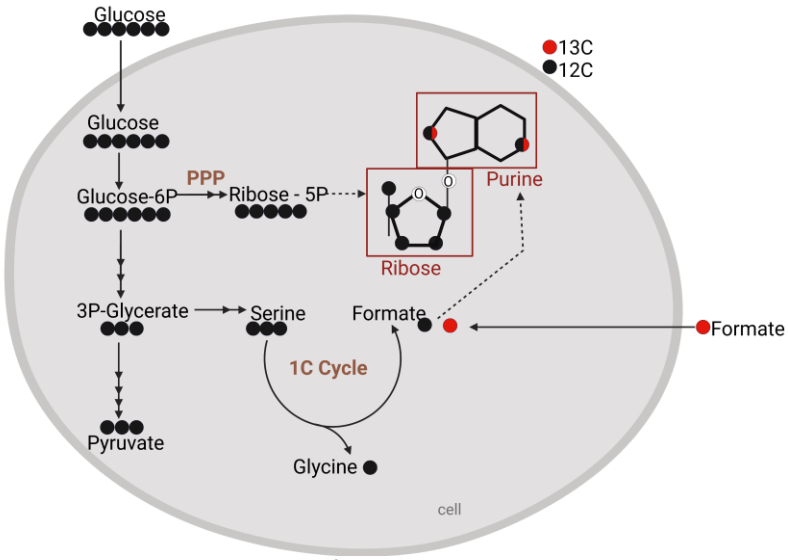

Illustration 35: *De Novo* Purine Synthesis from a [U-^{13}C]Formate Tracer
Schematic depiction of the interdependence of metabolic pathways and the expected metabolic ^{13}C label pattern from a [U-^{13}C]formate tracer. Illustration created with BioRender.com.

A significant increase in M+1 and M+2 was observed for all the tested cell lines after 24 hours of formate treatment. These results validate that exogenous formate is incorporated into purines (**Figure 6.6**).

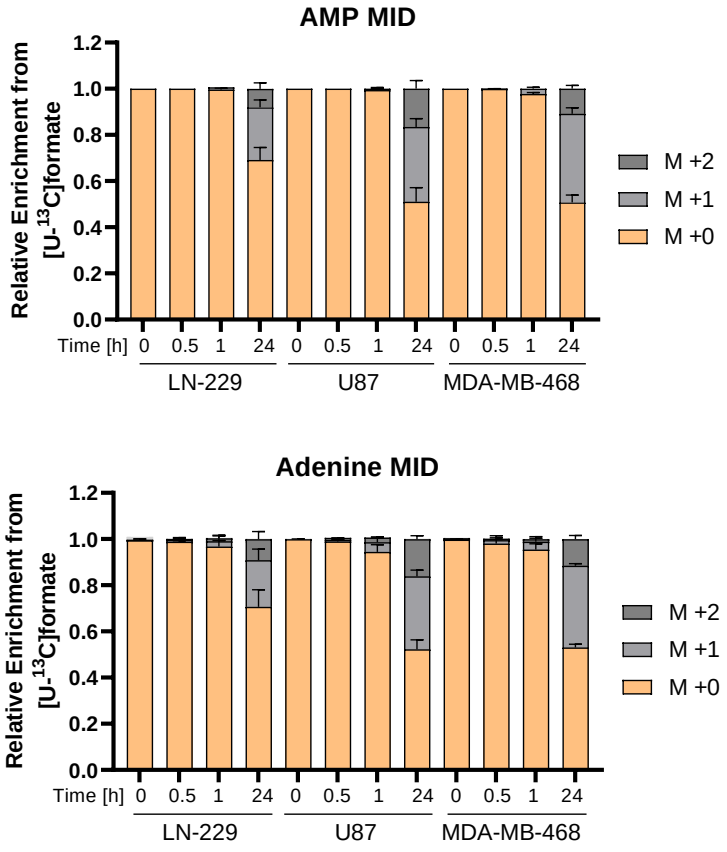

Figure 6.6: Exogenous Formate is Integrated Into Purines
Mass Isotopologue Distribution (MID) of intracellular AMP and adenine after the addition of [U-^{13}C]formate tracer in LN-229, U87, and MDA-MB-468 cells in response to different durations (0, 0.5, 1, and 24 hours) of 500 µM formate treatment. Each bar represents the mean of 3 independent experiments in triplicate wells. The error bars visualize the standard error of the mean (SEM).

To investigate if exogenous formate also contributes to the serine pool in the cell via the cytosolic 1C metabolism, we analysed the serine labelling after [U-^{13}C]formate treatment (**Illustration 36**).

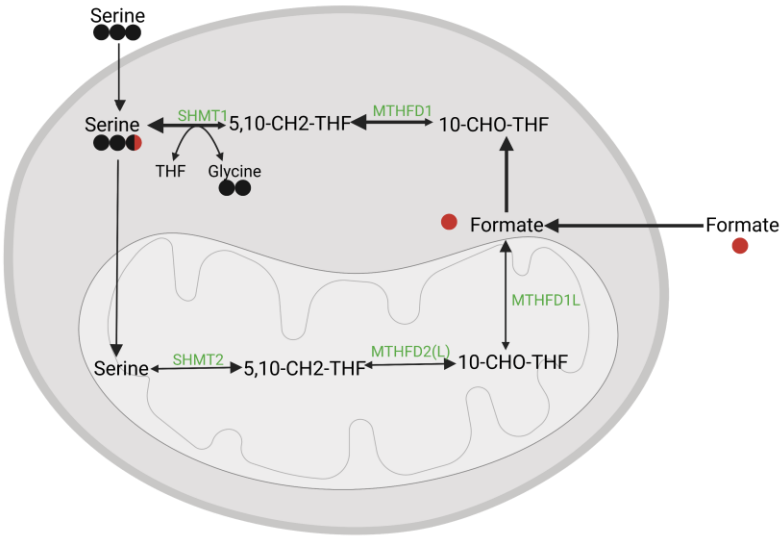

Illustration 36: *De Novo* Serine Synthesis from a [U-^{13}C]Formate Tracer
Schematic depiction of the 1C metabolism and the expected serine label pattern from a [U-^{13}C]formate tracer. Illustration created with BioRender.com.

Unexpectedly, ^{13}C labelled exogenous formate did not significantly contribute to serine synthesis through cytosolic 1C metabolism as there was no significant increase of M+1 serine measured. This indicates that exogenous formate predominantly feeds into the purine synthesis (**Figure 6.7**).

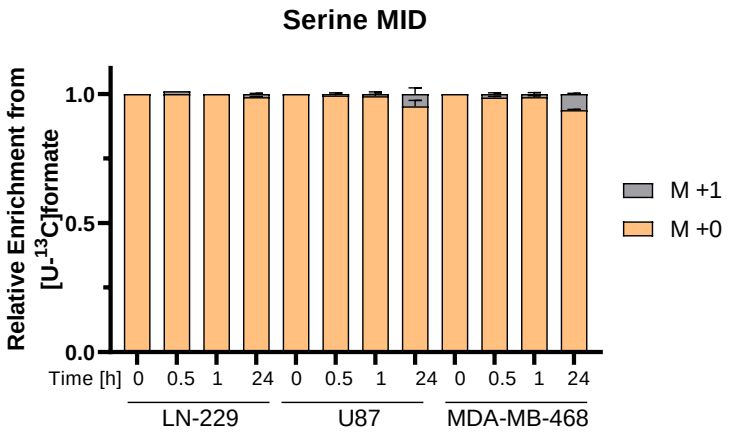

Figure 6.7: Exogenous Formate does Not Contribute to Serine Synthesis
Mass Isotopologue Distribution (MID) of intracellular serine after the addition of [U-^{13}C]formate tracer in LN-229, U87, and MDA-MB-468 cells in response to different durations (0, 0.5, 1, and 24 hours) of 500 µM formate treatment. Each bar represents the mean of 3 independent experiments in triplicate wells. The error bars visualize the standard error of the mean (SEM).

These results suggest a relation between formate and AMPK activation. As previously reported by Gowans *et al.*, (Gowans et al., 2013), AMPK gets activated by rising AMP and ADP levels.

Remarkably, MDA-MB-468 cells, which stood out because of their high AMP synthesis after 24 hours of formate treatment (**Figure 6.4**), also showed the highest AMPK activation (**Figure 6.3**). However, despite our experimental verification of formate-promoted AMP synthesis, the absolute levels of AMP in the different cancer cell lines were unaffected after exogenous formate supplementation (**Figure 6.8**).

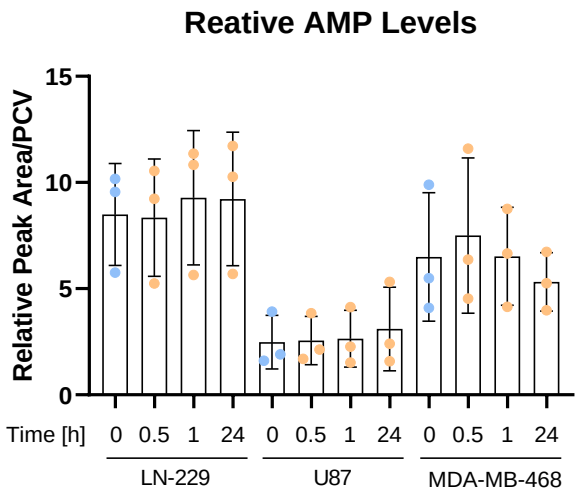

Figure 6.8: Formate does not affect AMP levels
Relative Peak Area normalised with respect to the packed cell volume (PCV) of AMP in LN-229, U87 and MDA-MB-468 cells treated for different durations (0, 0.5, 1, and 24 hours) with 500 µM Na-formate. Each dot represents the mean of 3 independent experiments in triplicate wells. The error bars visualize the standard deviation (SD). The data was evaluated using an unpaired *t*-test with Welch's correction.

Overall, our results suggest that formate triggers AMPK activation through enhanced AMP synthesis. Yet, as the relative levels of AMP were unaffected by formate supplementation, the mechanistic details how formate impacts the AMPK activity remains unsolved.

It should also be mentioned that the described changes in AMPK signalling were subtle and difficult to measure with the applied experimental techniques. The small changes in AMPK activity could result from subcellular AMPK localisation and activity. For example, AMPK activity could be locally restricted in close proximity to the purinosomes. Purinosomes are presumed purine synthesis complexes located at the outer mitochondrial membrane (French et al., 2016; Pareek et al., 2020). More generally, other results in the literature highlighted already the role of AMPK in cancer cell invasion and metastasis (Cai et al., 2020; Cao et al., 2019; Saxena et al., 2018). Furthermore, AMPK has already been shown to act in restricted, subcellular regions such as the invadopodia (Cunniff et al., 2016). Consequently, whole-cell protein extracts may limit the possibility to capture strong formate-dependent differences in AMPK activation.

6.3 AMPK Is Involved in Formate-Induced Invasion

The identified potential functional relevance of AMPK activation was validated by employing CRISPR/CAS9-mediated *AMPK* KO in LN-229 cells. First, the KO was verified by Western Blots (**Figure 6.9**).

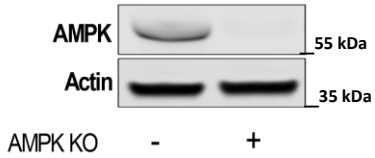

Figure 6.9: AMPK KO Validation
Representative Western Blot of LN-229 Control and *AMPK* KO cells.

Then, the invasive capacity of *AMPK* KO cells compared to control cells was characterized in Boyden chamber assays (**Figure 6.10**). The importance of AMPK for cell invasion was shown by the reduced basal invasion rate of the *AMPK* KO cells. To be precise, 30-50% fewer *AMPK* KO cells invaded the lower part of the Boyden chamber when compared to the control cells (**data not shown**). The finding that formate supplementation of the *AMPK* KO cells did not increase the total number of invaded cells shows that AMPK is an important intermediate in the formate-induced invasion signalling cascade (**Figure 6.10**).

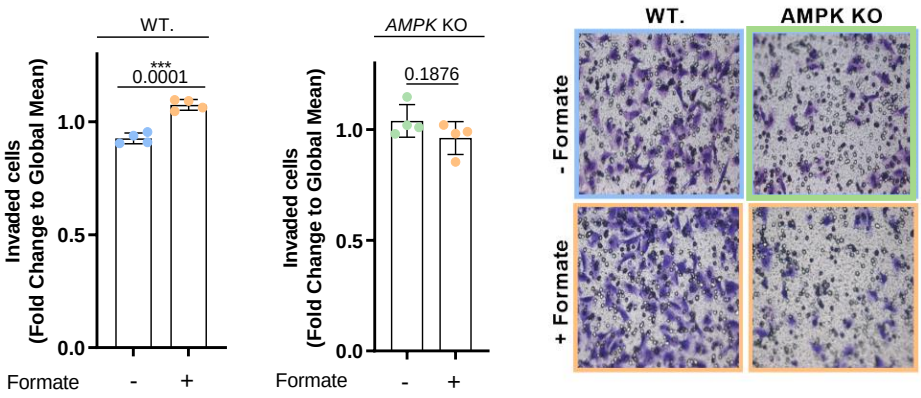

Figure 6.10: AMPK KO Prevents Formate-Induced Invasion
Left: Invasion of LN-229 control or *AMPK* KO cells either treated for 24 hours with 500 µM formate or not. The invasion was assessed using ECM-collagen-coated Boyden chambers. Each dot represents an independent experiment, the bars represent the mean, and the error bars visualize the standard deviation (SD). The data was evaluated using an unpaired *t*-test with Welch's correction. Right: Representative images of the Boyden chambers.

Finally, to investigate if AMPK acts upstream of FAS and MMP signalling, the expression levels of FAS-related genes and MMP were examined by an RT-qPCR in LN-229 *AMPK* KO cells (**Figure 6.11**). Formate promoted *MMP2*, *SCD*, *SREBF1*, *INSIG1*, and *FADS2* gene expression in the LN-229 control cells, but it did not affect the gene expression level in the cells lacking functional AMPK.

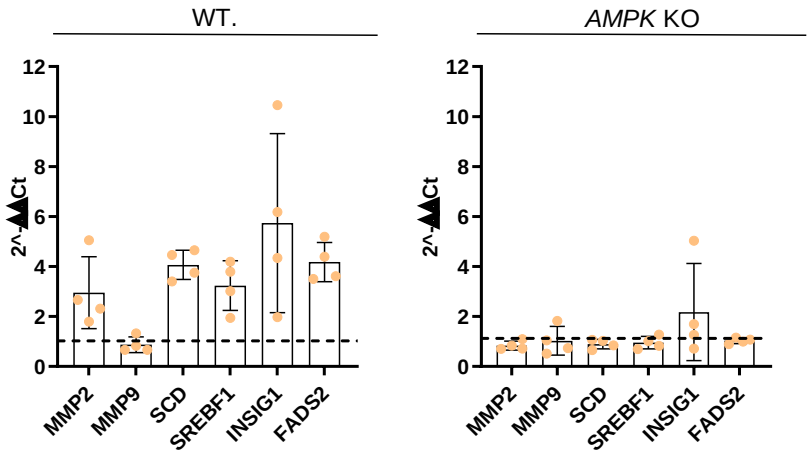

Figure 6.11: *AMPK* KO Prevents *MMP2* and *FAS* Gene Upregulation
mRNA expression from *MMP2, MMP9, SCD, SREBF1, INSIG1*, and *FADS2* in LN-229 control or *AMPK* KO cells that were treated either for 24 hours with 500 µM formate or not. The results are presented as $2^{-\Delta\Delta Ct}$, representing the relative fold gene expression with respect to untreated cells. Each dot represents a biological replicate, the bars represent the mean, and the error bars visualize the standard deviation (SD). The fold change of 1, which represents the gene expression of the control cells, is represented by a black dotted line.

Taken together, these results indicate a potential role for AMPK in formate-induced invasion. Further investigations are now required to define the mechanistic details of the interplay between AMPK and formate and its implication in cancer cell invasion.

7. Working Model

Based on the structured implications described in the previous sections, a plausible model for formate's role in cancer cell invasion can be summarized (**Illustration 37**). We hypothesize that the extracellular formate, which is taken up by the cells, enhances *de novo* purine biosynthesis. Potentially, this alteration in formate flux promotes fatty acid metabolism through AMPK activation. Finally, increased FAS promotes invasion by MMP activation and secretion. Further research is required to validate this mechanistic process and to understand the relationship between the signalling intermediates.

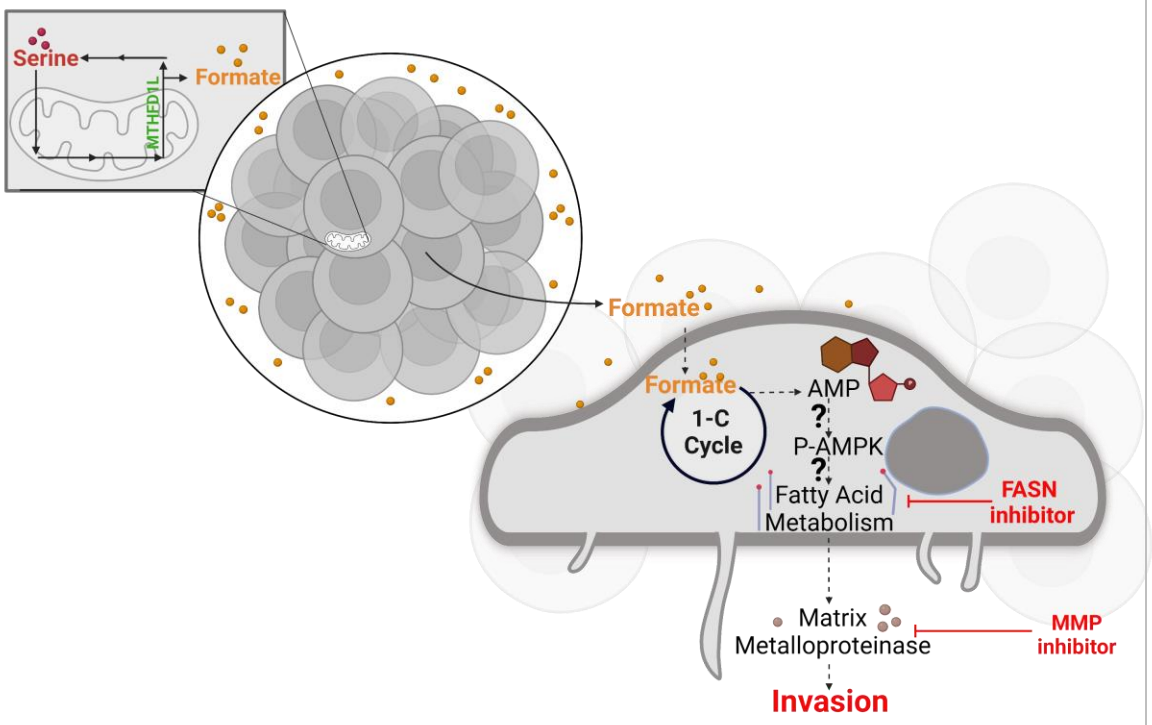

Illustration 37: Working Model
Schematic representation of a hypothetical mechanistic model for the role of formate in cancer cell invasion. Illustration created with BioRender.com.

Discussion

A novel function of formate: The *ex vivo* and *in vivo* experiments reported in this thesis, combined with previous works from our laboratory (Meiser et al., 2018) describe a novel physiological function of formate overflow, which is related to the invasiveness of cancer cells and their ability to form metastases. Already prior to our studies, it was demonstrated that the anabolic function of the mitochondrial 1C metabolism is dispensable for cancer cell proliferation as the cytosolic part of the 1C metabolism can compensate for mitochondrial 1C cycle inhibition (Ducker and Rabinowitz, 2017). We confirm these results as we did not observe a reduction in proliferation after the loss of MTHFD1L protein expression. However, the knockdown of *MTHFD1L*, which specifically inhibits formate overflow, was shown to affect cancer cell invasion (Kiweler et al., 2022; Meiser et al., 2018; Meiser et al., 2016). This suggests that formate, in addition to its anabolic function, has a non-anabolic role. We hypothesized formate to act as a signalling molecule that triggers cancer cell invasion. Declaring formate as a signalling molecule, could also explain the unidentified relation between *MTHFD1L* loss and neural tube defects during embryogenesis (Momb et al., 2013). Successful neural tube formation requires first the proliferation of cells with the correct cell polarity and second their migration to the neural tube (Copp and Greene, 2013). As formate triggers invasion, it may also serves as a signalling molecule in the migration step of the neural tube formation. However, this hypothesis remains to be verified. This thesis provides, some mechanistic insights in how formate triggers a pro-invasive signalling cascade.

Using an RNAseq analysis, we identified the fatty acid metabolism and the release of specific matrix metalloproteinases (MMP) to be essential to mediate the formate-induced pro-invasive phenotype. The inhibition of either MMP or fatty acid synthesis activity successfully blocked the formate-dependent pro-invasive behaviour *in vitro* and *ex vivo*. Furthermore, our experiments indicate that AMPK activation is involved in this process. AMPK activation hereby seems to be caused by a purine flux imbalance in response to increased formate levels. The resulting mechanistic model underlines the selective advantage of the compartmentalization of the 1C metabolism into one cytoplasmic and one mitochondrial part and provides a rationale for the evolutionarily conserved formate overflow phenotype. Additionally, it pinpoints an entry point for targeted therapeutics against cancer cell invasion. Until now, only the cytosolic 1C metabolism was targeted as foreseen by the antifolates (Dekhne et al., 2020; Osborn et al., 1958). Yet, recent research from our laboratory highlighted that even after the inhibition of the cytosolic 1C metabolism, the mitochondrial pathway sustains an autarkic 1C metabolism characterized by formate overflow (Kiweler et al., 2022). Thus, formate overflow inhibition can only be achieved through genetic interventions or the use of special inhibitors that specifically target the mitochondrial 1C cycle. Although no specific MTHFD1L inhibitor was discovered yet, specific mitochondrial 1C inhibitors exist. For example, carolacton, a naturally occurring

molecule, was shown to inhibit MTHFD2 in a low nanomolar range (Fu et al., 2017). Moreover, DS44960156, a structure-based designed drug, was identified to specifically inhibit MTHFD2 (Kawai et al., 2019). Interestingly, when administered orally, DS44960156 demonstrated a remarkable anti-tumour effect in mice with minimal treatment-related toxicity (Kawai et al., 2019). Accounting for the metabolic flexibility, it will be important in future applications to combine mitochondrial 1C-metabolism-targeting drugs with inhibitors of other targets. As cancer cells are dependent on *de novo* serine synthesis from the glycolic intermediate 3PG, it might be of interest to combine mitochondrial 1C inhibitors with SSP inhibitors to completely block purine synthesis as well as formate overflow (Dekhne et al., 2020).

Formate, an oncometabolite: The experiments in this thesis underline that formate acts as an oncometabolite. Formate overflow and particularly high formate levels were identified in multiple cancers and the TME (Meiser et al., 2018; Meiser et al., 2016; Ternes et al., 2022). Similarly to formate, high levels of lactate were repeatedly measured in tumour microenvironments. Already Otto Warburg noticed that tumour cells consume high levels of glucose and release large volumes of lactate even in the presence of oxygen (Warburg, 1956; Warburg et al., 1927). In the tumour microenvironment, lactate can be used as an energetic source, an immune suppressor, and a signalling molecule: (1) Lactate can be used by the cells as an energetic source due to its conversion to pyruvate, which in turn enters into the TCA cycle (Fantin et al., 2006; Mayer et al., 2014; Wang et al., 2014; Wong et al., 2015). (2) Lactate can also be used as an important immune suppressor as the secretion of lactate by tumour cells acidifies the tumour microenvironment. This acidification reduces the intracellular pH of immune cells affecting important signalling pathways (García-Cañaveras et al., 2019). (3) Lactate can also be used as a signalling molecule. For example, it was experimentally shown that lactate initiates invasion through the activation of the TGF-β1/p38/MAPK/MMP2/9 signalling pathway (Sun et al., 2019). Using different *in vitro*, *ex vivo,* and *in vivo* models, this thesis demonstrates that high levels of formate promote cancer cell invasion and metastasis in multiple cancer types and under various physiological conditions. This conclusion substantiates previous findings of our laboratory which indicated that formate promotes GBM cell invasion *in vitro* (Meiser et al., 2018*)*. Given its role as an oncometabolite, we hypothesised that formate could act analogue to lactate in the tumour microenvironment. (1) We excluded the hypothesis that formate could act as an energetic source supplying the central carbon metabolism through the reversibility of the serine synthesis pathway, as only little serine was synthesised from exogenous formate. (2) Yet, similar to lactate, we expect that formic acid acidifies the tumour microenvironment and impacts so the surrounding cells. Using fluorogenic pH indicators, a possible

acidification of the tumour environment could be measured. (3) We experimentally tested if formate acts as a signalling molecule triggering a pro-invasive phenotype.

A priori, formate could be an extrinsic or intrinsic signalling molecule. The extrinsic model yields that formate is secreted into the cells' local environment, where it activates through transmembrane acceptors an invasion triggering signaling cascade. The intrinsic model conjectures that formate operates in a cell-autonomous manner. Independent of the considered model, the formyl-peptide receptors (FPRs) are promising candidates to detect formate-induced signals. FPRs are G-protein coupled receptors that are involved in chemotaxis. They are known to sense bacterial or host-derived formyl-peptides and to regulate inflammatory responses (Ye et al., 2009). FPR activation can induce cytoskeleton rearrangements and increase the migration potential of cancer cells (Ye et al., 2009), both being important features in invasion. Interestingly, based on the data from "The Cancer Genome Atlas", the expression of *FPR1* is increased in GBM. Additionally, FPRs were associated with increased invasiveness of glioma cells (Huang et al., 2010). Yet, we were not able to experimentally verify the implication of FPRs' in formate-induced invasion. Although *FPR1* KD prevented formate-induced invasion in the GBM cell line LN-229, the KD didn't prevent fatty acid synthesis after exogenous formate addition.

Physiological concentration of formate: To genetically link the pro-invasive phenotype to the formate-synthesizing activity of MTHFD1L, the invasion of *MTHFD1L* KD cells was studied in *ex vivo* and *in vivo* models. 100 µM of Na-formate in the extracellular medium was sufficient to rescue the invasion upon *MTHFD1L* silencing (Meiser et al., 2018). It can be assumed that such concentrations are within the physiological range of the tumour microenvironment as higher concentrations have been measured in previous studies: While standard formate levels in the blood of murines and humans were found in the range of 10-100 µM (Pietzke et al., 2020), recent formate measurements in tumour interstitial fluid (TIF) suggest that formate concentration can be significantly above 100 µM (Ternes et al., 2022). Unfortunately, our laboratory was not able to confirm these intra-tumoral concentrations (Kiweler et al., 2022), as we could not isolate sufficient TIF for the formate analysis due to technical limitations. More quantitative insights on standard formate concentrations within the tumour environment need to be gained to validate the physiological relevance of the findings of this thesis.

Recent works in the context of colorectal cancer (CRC) revealed that microbiome-derived formate and the related high formate concentrations in the gut (10 mM) exacerbate CRC progression via AHR signalling (Ternes et al., 2022). The experiments in this thesis, provide evidence that significantly lower formate concentrations can already impact cancer cell invasion through different mechanisms. For example, in contrast to the observations made in CRC, the transcriptome analysis of GBM cells treated with 500 µM of formate did not

reveal the activation of AHR signaling while invasion was nevertheless promoted at these comparatively low formate concentrations.
Thus, a context-dependent and mechanistic understanding of the processes that underlie formate-dependent invasion is important to design cancer-type specific and effective intervention strategies.

Difference between endogenous and exogenous formate on cellular migration: While formate supplementation promoted cancer cell invasion, it did not affect cancer cell migration. This observation supports the assumption that enhanced cellular migration is not a phenotypic requirement of cancer cell invasion (Schaeffer et al., 2014). Surprisingly, our laboratory uncovered that low doses of Mtx promote formate overflow, and, simultaneously, that perturbations of the mitochondrial serine catabolism reduce the migration capacity of Mtx-treated cells (Kiweler et al., 2022). However, as formate supplementation does not affect the cells' potential to migrate, these results may suggest that the sustained migration potential upon Mtx depends on endogenous serine catabolism and its associated biochemical outputs. Probably two very different mechanisms are in action. Indeed, we expect that the sustained Mtx-dependent migration only occurs in non-proliferating cells. Hence, we conjecture that the motility phenotype associated with the mitochondrial serine catabolism might be impacted by two individual effects: (1) serine catabolism itself and (2) local concentrations of formate in the tumour microenvironment. The latter depend on the rate of formate overflow and the fate of formyl-THF. An increased expression of ALDH1L2 can lower the formate overflow and vice versa. Similarly, the oxidation of 10-CHO-THF to CO_2 via ALDH1L2 or the hydrolysis of 10-CHO-THF to formate via MTHFD1L generates mitochondrial NADPH or ATP, respectively. These two different functional outlets of mitochondrial 1C metabolism illustrate the plasticity of serine catabolism and underline the ability of cancer cells to adapt to changes within the local tumour microenvironment and to satisfy their metabolic needs along the metastatic cascade (Benzarti et al., 2020; Fendt et al., 2020).

The difficulty to study the underlying mechanism: Apart from highlighting that formate promotes invasion, the experiments in this thesis investigated the mechanism of formate-induced invasion. Although several signalling intermediates were uncovered, further investigations are still required to deepen the current understanding of their causal relationship. The study of the mechanistic aspects was technically challenging, as the measurable molecular changes triggered by formate supplementation are subtle. Furthermore, the experimental study of the cellular signalling cascade in the context of formate-induced invasion is difficult in general as: (1) Cellular signalling is a dynamic process that involves a large variety of molecules and many experiments can only

document a particular snapshot of the involved events. Thereby the correct time-point allowing to detect formate-dependent differences needs to be identified, which requires a large number of trial-and-error experiments. (2) Cellular signalling can be locally restricted to subcellular regions. Consequently, whole-cell extracts might cloud small formate-dependent changes. As it is believed that the formate-induced pro-invasive signalling cascade is restricted within the invadopodia (Cunniff et al., 2016), our laboratory tried to isolate proteins specifically from this cellular structure (Howe et al., 2005). Unfortunately, our experimental attempts did not lead to reproducible results. (3) Weak cellular signals are difficult to catch using the available technology. For example, fluorophores used to monitor intracellular changes in ROS showed only weak signal intensity and very low signal-to-noise ratios. Therefore, no formate induced changes in ROS were detected. Although physiological formate concentrations were described to promote the release of mitochondrial ROS from mouse liver mitochondria (Young et al., 2017), our experiments could not confirm this observation as the changes in ROS level were not significant. The cellular Redox state represents a double-edged sword as it can be beneficial at physiological doses but deleterious at higher doses. Indeed, Redox biology involves a small increase in ROS levels that activates signalling pathways to initiate biological processes (Finkel, 2011), while oxidative stress denotes high levels of ROS that damage DNA, proteins, and lipids (Nogueira et al., 2008; Trachootham et al., 2006). An example of a well-studied mechanism of Redox signalling involves the H_2O_2-mediated oxidation of cysteine residues within proteins, causing alterations in the protein function (Rhee, 2006). Live cell imaging in combination with improved reporter fluorophores could improve the fluorescent sensitivity, which in turn could reveal more insights into our hypothesised intracellular signalling cascades.

Formate and MMP: A considerable amount of publications confirms our observations by describing the implication of MMPs in cancer spreading. For example, a positive correlation between MMP expression and cancer cell invasion and metastasis was observed in colon, lung, head and neck, breast, thyroid, prostate, ovarian, and gastric carcinomas (Westermarck and Kähäri, 1999). The matrix metalloproteinase MMP2 was associated with invasion and angiogenic properties in gliomas and is a marker of poor prognosis (Du et al., 2008; Sincevičiūtė et al., 2018; Wang et al., 2003). MMP16 was shown to act by activating proMMP2 into its active form (Nakada et al., 1999; Wang et al., 2015). Our data confirms the proteolytic activity of MMPs as an important key factor in invasion and formate-dependent invasion. Our data indicates that MMP16-dependent MMP2 activation is crucial for formate-induced LN-229 cell invasion as targeting the MMP activity through specific MMP inhibitors (MMPi) successfully inhibited formate-dependent invasion *in vitro* and in *ex vivo* brain slices. However, counter-intuitively, clinical trials with MMP inhibitors were not

successful in reducing tumour burden or improving the overall survival of cancer patients (Coussens et al., 2002; Overall and López-Otín, 2002; Winer et al., 2018).

Two main causes have been hypothesised that could explain MMP inhibitions failure in clinical trials. (1) The MMPis may not be specific enough for clinical treatments. MMPis, such as batimastat, are unspecific and inhibit different MMPs. Yet, while most MMPs are pro-tumorigenic, some MMP family members like MMP8 were shown to have anti-tumour effects (Balbín et al., 2003). Consequently, the simultaneous inhibition of different MMPs might as well block the anti-tumorigenic MMPs and results in tumour development and progression (Winer et al., 2018). (2) The treatment was potentially administered at the wrong stage of tumour progression. Clinical trials were only performed in patients with advanced disease status, whereas MMPs are known to act in principle in the earliest stage of tumour development (Winer et al., 2018). All in all, valuable lessons were learned from prior trial failures and the hope for MMPi as an anti-tumour drug is not lost yet.

The experiments in this thesis also reveal that the enhanced expression and release of MMPs are cell-type-specific. Whereas in the GBM cell line LN-229, formate-induced invasion was promoted by MMP2 release, the invasion of U87 cells was promoted by MMP9 release.

Formate and fatty acid synthesis: The experiments in this thesis also uncover that high formate levels promote fatty acid synthesis. Furthermore, increased fatty acid synthesis was revealed to act as an upstream regulator of MMP activation and expression. This result is supported by previous findings stating that high levels of fatty acids promote the degradation of the extracellular matrix via MMP activation (Boden and Song, 2008; Soto-Guzman et al., 2010). In 2010, Soto-Guzman *et al.* showed that the addition of 200 µM of oleic acid (a monounsaturated C18 fatty acid) significantly increased MMP9 activity in the MDA-MB-468 breast cancer cell line. Furthermore, they showed that oleic acid induces MMP9 secretion through a PKC-Src-EGFR-dependent signalling pathway (Soto-Guzman et al., 2010). As, in our experimental set-up, formate did not induce MMP9 in the MDA-MB-468 cells, we hypothesise that in this cell line, formate triggers MMP release via an alternative signalling pathway.

De novo fatty acid synthesis is an important component of tumour malignancy and an attractive target for clinical interventions (Menendez and Lupu, 2007). It was shown that normal cells derive fatty acids exogenously while tumour cells derive fatty acids both exogenously and by *de novo* synthesis (Medes et al., 1953). Thereby, fatty acid synthesis upregulation is a hallmark of a cancerous phenotype. For example, the fatty acid synthesis genes *ACC* and *FASN* were both demonstrated to be highly expressed in glioblastoma and were associated with poor patient outcomes (Taïb et al., 2019). Furthermore, breast

cancers that are capable of metastasizing to the brain presented an altered lipid metabolism (Ferraro et al., 2021; Jin et al., 2020).

Ferraro *et al.* hypothesised that the low-free-lipid-containing environment of the brain promotes fatty acid synthesis by *SREBP1* and *FASN* upregulation (Ferraro et al., 2021). Interestingly, the deletion of *FASN* impaired the ability of the cells to proliferate when injected into brain tissue (Ferraro et al., 2021).

These results show the interest to develop potent and selective FASN inhibitors, which are expected to inhibit cancer growth in the brain microenvironment (Vogel and Schulze, 2021). However, the clinical development of FASN inhibitors encounters several challenges such as the blood-brain barrier. To inhibit FASN in the brain, the inhibitors need to cross not only the blood-brain barrier, but also the blood-tumour barrier (Vogel and Schulze, 2021). An objective of an approved clinical trial is to determine the extent by which the FASN inhibitor TVB-2640 can penetrate the blood-brain barrier where it might have the opportunity to affect tumour tissue metabolism (W. Kelly et al., 2020).

As some fatty acids were uncovered to support tumorigenesis and cancer progression, they became a target of interest to inhibit GBM invasion and its metastasis into the brain. The data in this thesis pinpoints formate as an upstream regulator of fatty acid synthesis promoting thereby invasion and metastasis. Furthermore, these observations underline that targeting fatty acid synthesis using two specific FASN inhibitors (TVB-2640 and C75) successfully prevents formate-induced invasion. Remarkably, TVB-2640 did not impact invasion at the basal level but specifically prevented the formate-dependent increase in invasion *in vitro* and *ex vivo.* This suggests that fatty acid synthesis is a key factor in formate-induced invasion. TVB-2640 is already in clinical development for the treatment of CRC and a very encouraging results with a 66.7% overall response rate has been reported from phase 1 trials of TVB-2640 in combination with bevacizumab in recurrent astrocytoma (W. Kelly et al., 2020).

Interestingly, fatty acid synthesis is also essential for embryogenesis. FASN KO embryos die *in utero* and the number of FASN heterozygous pups is 70% lower than predicted by Mendelian Inheritance (Chirala et al., 2003). Furthermore, fatty acid supplementation was shown to effectively protect NTDs in mice (Li et al., 2021).

Formate and AMPK: After having identified MMPs and fatty acid synthesis as molecular processes acting downstream of formate, the identification of a molecular regulator acting as a mediator between formate and fatty acid synthesis was attempted. Although biochemical textbooks describe AMPK to inhibit *de novo* lipogenesis through ACC inhibition (Hardie and Pan, 2002), we observed higher fatty acid synthesis without any effect on ACC phosphorylation. No similar observations were described in the literature. We hypothesised

that minor changes in AMPK phosphorylation act differently than major changes, which would explain why no changes in the ACC phosphorylation were observed.
Furthermore, non-detectable subcellular effects might play a substantial role in invasion. Nevertheless, the observations in this thesis indicate that formate-dependent AMPK activation could be an upstream event preceding the activation of fatty acid synthesis.
We speculate that weak AMPK phosphorylation, as observed upon formate supplementation, does not inhibit but promote fatty acid synthesis. Yet, as indicated, ACC phosphorylation and levels remained unchanged in our experiments.

The importance to study formate induced invasion: Overall, our results point to two therapeutic entry points to oppose formate-dependent invasion and limit so the pro-metastatic behaviour of cancer cells. The MMP and the FASN inhibitors successfully prevented formate-induced invasion *in vitro* as well as *ex vivo*. Such interventions could be promising in the context of tumours that show high levels of formate overflow and high intra-tumoral formate concentrations. Interestingly, recent experiments demonstrated in multiple genetically engineered mouse models (GEMMs), that the rate of formate release depends on the oxidative state of the tumour (Meiser et al., 2018). Compared to the control group, plasma levels of formate were strongly increased in GEMMs for intestinal adenoma, breast cancer, and lymphoma, but not for pancreatic cancer. Pancreatic cancer was described as poorly oxidative and formate overflow negative (Meiser et al., 2018) as opposed to the other class of cancer, like intestinal adenoma, breast cancer, and lymphoma that are active in oxidative metabolism and formate overflow positive (Meiser et al., 2018). It is thus tempting to speculate that formate acts as an upstream regulator of fatty acid synthesis especially, in oxidative tumours.

Formate a post-translational modificator: Further research is needed to increase the mechanistic depth of the outlined mechanistic model and to explore its therapeutic uses. Although the importance of fatty acid synthesis and MMP release in formate-induced invasion was demonstrated, the experiments in this thesis are not sufficient to uncover the full mechanism of how formate triggers the phenotypic changes of cancer cells. Unfortunately, we were not able to fully understand the entire signalling cascade that triggers formate-induced invasion. We are lacking information on how formate triggers fatty acid synthesis in cancer cells. Our most recent hypothesis postulates that formate promotes post-translational modifications that are involved in cancer cell invasion. More precisely, the methylation and acetylation of lysine residues of histones and other proteins accounts for the most frequent post-translational modification in eukaryotic cells and dictates the chromatin conformation as well as its corresponding gene activity. As previously described, formate plays a dual role in the methylation processes: (1) It provides 5,10-CH_2-THF, which

is transformed by methylene tetrahydrofolate reductase (MTHFR) into 5-methyl-THF, which in turn is required for the re-methylation of homocysteine.
Yet, independent experiments underlined that this substrate supply plays only a minor role in the re-methylation process (Bhatia et al., 2020; Maddocks et al., 2016). (2) The major contribution of the 1C metabolism in the methylation process is through the *de novo* synthesis of ATP, which is required for SAM synthesis (Maddocks et al., 2016). For example, serine starvation was shown to decrease the methylation ratio of DNA and RNA, as well as the ATP levels in CRC cells (Kottakis et al., 2016). Thus, high formate levels could promote protein methylations that favour cancer cell invasion.

Furthermore, recent research linked formylations at lysine residues of histones and other nuclear proteins (Wisniewski et al., 2008). Aligned with this observation, we conjecture that high levels of formate initiate the formylations of specific proteins, which, in turn, promote invasion. This hypothesis is supported by the fact that the formate-induced invasion signal persists for several hours. On the one hand, formylation could directly impact protein functions by affecting (1) the protein folding efficiency, (2) the conformational stability, (3) the catalytic function and (4) the fate of the protein localisation by directing it to distinct cellular compartments. If so, formylations on histones residues could dictate the gene activity. Moreover, formylations on non-histone proteins could also impact their function. For example, direct formylations on FASN could trigger fatty acid synthesis without an upstream signalling pathway. On the other hand, formylation could indirectly promote invasion by acting as steric bulks hindering other post-translational modifications (Tolsma and Hansen, 2019).

Future studies are needed to expand the mechanistic insights on formate-induced invasion and to further define the therapeutic use of the corresponding mechanistic model. Efficient strategies to overcome cancer cell dissemination are hereby of utmost clinical importance!

Future Perspectives

This doctoral thesis consolidates formate as a pro-invasive metabolite. It underlines the physiological relevance and the cancer type independence of formate-induced invasion. Additionally, it uncovers different aspects of formate-induced invasion and proposes a motivated mechanistic model of formate in cancer metastasis. Further studies are required to increase the mechanistic depth and to find corresponding therapeutic uses. Some relevant prospective research directions are listed below:

1) The Free Fatty Acid Receptor (FFAR) was identified as one of the most upregulated genes in our RNAseq analysis. Yet, the role of FFAR in formate-induced invasion remains unknown. To study the mechanistic link between formate and FFAR a collaboration between our group and the group of Dr Andy Chevigné (Immunopharmacology and Interactomics group, Luxembourg Institute of Health) was created. The research goal of this collaboration is to monitor FFAR activation upon formate treatment using a nanoluciferase complementation-based assay (NanoBit, **Promega**).
2) How formate triggers the invasive cascade, in general, should be studied in further detail. We expect protein formylation at lysine residues to be a plausible molecular link between formate and invasion, but we are currently missing the necessary experimental verification of this hypothesis. Identifying formylated proteins and the signalling functions of such post-translational modifications in the metastatic cascade could help to reveal this molecular link. Immunoprecipitation (IP) using an anti-formylation antibody followed by an LC-MS-based high-resolution measurements can be used to identify the implicated formylated targets. LC-MS analysis of such IP experiments is currently carried out.
3) Motivated by the effect of formate on ECM degradation, it could be of interest to study the underlying signalling mechanism of how fatty acid synthesis impacts the matrix metalloproteinases release in further detail.
4) The potential therapeutic interventions to target FAS should be evaluated in a physiologically relevant *in vivo* model. For example, cancer cells that were simultaneously pre-treated with formate and TVB-2640 could be injected into the tail vein of NSG mice to investigate if TVB-2640 can prevent the formate-dependent seeding capacity *in vivo.*
5) To confirm again the physiological relevance of our experiments, it should be validated that the formate concentrations described in this thesis are within the physiological range of the tumour microenvironment. In particular, formate levels in the tumour interstitial fluid of different cancer entities should be measured.

References

Agarwal, S., Behring, M., Hale, K., Al Diffalha, S., Wang, K., Manne, U., and Varambally, S. (2019). MTHFD1L, A Folate Cycle Enzyme, Is Involved in Progression of Colorectal Cancer. Transl Oncol *12*, 1461-1467.

Allegra, C.J., Hoang, K., Yeh, G.C., Drake, J.C., and Baram, J. (1987). Evidence for direct inhibition of de novo purine synthesis in human MCF-7 breast cells as a principal mode of metabolic inhibition by methotrexate. J Biol Chem *262*, 13520-13526.

Amelio, I., Cutruzzolá, F., Antonov, A., Agostini, M., and Melino, G. (2014). Serine and glycine metabolism in cancer. Trends Biochem Sci *39*, 191-198.

Antoniewicz, M.R. (2021). A guide to metabolic flux analysis in metabolic engineering: Methods, tools and applications. Metab Eng *63*, 2-12.

Apte, S.S. (2009). A disintegrin-like and metalloprotease (reprolysin-type) with thrombospondin type 1 motif (ADAMTS) superfamily: functions and mechanisms. J Biol Chem *284*, 31493-31497.

Aseervatham, J. (2020). Cytoskeletal Remodeling in Cancer. Biology (Basel) *9*.

Balbín, M., Fueyo, A., Tester, A.M., Pendás, A.M., Pitiot, A.S., Astudillo, A., Overall, C.M., Shapiro, S.D., and López-Otín, C. (2003). Loss of collagenase-2 confers increased skin tumor susceptibility to male mice. Nat Genet *35*, 252-257.

Bannai, S., and Ishii, T. (1988). A novel function of glutamine in cell culture: utilization of glutamine for the uptake of cystine in human fibroblasts. J Cell Physiol *137*, 360-366.

Benzarti, M., Delbrouck, C., Neises, L., Kiweler, N., and Meiser, J. (2020). Metabolic Potential of Cancer Cells in Context of the Metastatic Cascade. Cells *9*.

Bhatia, M., Thakur, J., Suyal, S., Oniel, R., Chakraborty, R., Pradhan, S., Sharma, M., Sengupta, S., Laxman, S., Masakapalli, S.K.*, et al.* (2020). Allosteric inhibition of MTHFR prevents futile SAM cycling and maintains nucleotide pools in one-carbon metabolism. J Biol Chem *295*, 16037-16057.

Blacher, S., Erpicum, C., Lenoir, B., Paupert, J., Moraes, G., Ormenese, S., Bullinger, E., and Noel, A. (2014). Cell invasion in the spheroid sprouting assay: a spatial organisation analysis adaptable to cell behaviour. PLoS One *9*, e97019.

Blount, B.C., Mack, M.M., Wehr, C.M., MacGregor, J.T., Hiatt, R.A., Wang, G., Wickramasinghe, S.N., Everson, R.B., and Ames, B.N. (1997). Folate deficiency causes uracil misincorporation into human DNA and chromosome breakage: implications for cancer and neuronal damage. Proceedings of the National Academy of Sciences of the United States of America *94*, 3290-3295.

Boden, G., and Song, W.W. (2008). Effects of insulin and free fatty acids on matrix metalloproteinases. Curr Diab Rep *8*, 239-242.

Bolusani, S., Young, B.A., Cole, N.A., Tibbetts, A.S., Momb, J., Bryant, J.D., Solmonson, A., and Appling, D.R. (2011). Mammalian MTHFD2L encodes a mitochondrial methylenetetrahydrofolate dehydrogenase isozyme expressed in adult tissues. J Biol Chem *286*, 5166-5174.

Bonnans, C., Chou, J., and Werb, Z. (2014). Remodelling the extracellular matrix in development and disease. Nat Rev Mol Cell Biol *15*, 786-801.

Bressler, J., Folsom, A.R., Couper, D.J., Volcik, K.A., and Boerwinkle, E. (2010). Genetic variants identified in a European genome-wide association study that were found to predict incident coronary heart disease in the atherosclerosis risk in communities study. Am J Epidemiol *171*, 14-23.

Brosnan, M.E., and Brosnan, J.T. (2016). Formate: The Neglected Member of One-Carbon Metabolism. Annu Rev Nutr *36*, 369-388.

Bruce-Gregorios, J.H., Agarwal, R.P., Oracion, A., Ramirez, A., and Lin, L. (1991). Effects of methotrexate on RNA and purine synthesis of astrocytes in primary culture. J Neuropathol Exp Neurol *50*, 770-778.

Buescher, J.M., Antoniewicz, M.R., Boros, L.G., Burgess, S.C., Brunengraber, H., Clish, C.B., DeBerardinis, R.J., Feron, O., Frezza, C., Ghesquiere, B.*, et al.* (2015). A roadmap for interpreting (13)C metabolite labeling patterns from cells. Curr Opin Biotechnol *34*, 189-201.

Bussemakers, M.J., and Schalken, J.A. (1996). The role of cell adhesion molecules and proteases in tumor invasion and metastasis. World J Urol *14*, 151-156.

Cai, Z., Li, C.F., Han, F., Liu, C., Zhang, A., Hsu, C.C., Peng, D., Zhang, X., Jin, G., Rezaeian, A.H.*, et al.* (2020). Phosphorylation of PDHA by AMPK Drives TCA Cycle to Promote Cancer Metastasis. Mol Cell *80*, 263-278.e267.

Cantor, J.R., and Sabatini, D.M. (2012). Cancer cell metabolism: one hallmark, many faces. Cancer Discov *2*, 881-898.

Cao, W., Li, J., Hao, Q., Vadgama, J.V., and Wu, Y. (2019). AMP-activated protein kinase: a potential therapeutic target for triple-negative breast cancer. Breast Cancer Res *21*, 29.

Cawston, T.E., and Young, D.A. (2010). Proteinases involved in matrix turnover during cartilage and bone breakdown. Cell Tissue Res *339*, 221-235.

Chambers, A.F., Groom, A.C., and MacDonald, I.C. (2002). Dissemination and growth of cancer cells in metastatic sites. Nat Rev Cancer *2*, 563-572.

Cheung, E.C., DeNicola, G.M., Nixon, C., Blyth, K., Labuschagne, C.F., Tuveson, D.A., and Vousden, K.H. (2020). Dynamic ROS Control by TIGAR Regulates the Initiation and Progression of Pancreatic Cancer. Cancer Cell *37*, 168-182.e164.

Chirala, S.S., Chang, H., Matzuk, M., Abu-Elheiga, L., Mao, J., Mahon, K., Finegold, M., and Wakil, S.J. (2003). Fatty acid synthesis is essential in embryonic development: fatty acid synthase null mutants and most of the heterozygotes die in utero. Proceedings of the National Academy of Sciences of the United States of America *100*, 6358-6363.

Christensen, K.E., and Mackenzie, R.E. (2008). Mitochondrial methylenetetrahydrofolate dehydrogenase, methenyltetrahydrofolate cyclohydrolase, and formyltetrahydrofolate synthetases. Vitam Horm *79*, 393-410.

Cook, R.J., and Blair, J.A. (1979). The distribution and chemical nature of radioactive folates in rat liver cells and rat liver mitochondria. Biochem J *178*, 651-659.

Copp, A.J., and Greene, N.D. (2013). Neural tube defects--disorders of neurulation and related embryonic processes. Wiley Interdiscip Rev Dev Biol *2*, 213-227.

Coussens, L.M., Fingleton, B., and Matrisian, L.M. (2002). Matrix metalloproteinase inhibitors and cancer: trials and tribulations. Science *295*, 2387-2392.

Coussens, L.M., and Werb, Z. (1996). Matrix metalloproteinases and the development of cancer. Chem Biol *3*, 895-904.

Cunniff, B., McKenzie, A.J., Heintz, N.H., and Howe, A.K. (2016). AMPK activity regulates trafficking of mitochondria to the leading edge during cell migration and matrix invasion. Mol Biol Cell *27*, 2662-2674.

de la Cruz-López, K.G., Castro-Muñoz, L.J., Reyes-Hernández, D.O., García-Carrancá, A., and Manzo-Merino, J. (2019). Lactate in the Regulation of Tumor Microenvironment and Therapeutic Approaches. Frontiers in Oncology *9*.

DeBerardinis, R.J., and Chandel, N.S. (2016). Fundamentals of cancer metabolism. Science advances *2*, e1600200.

Dekhne, A.S., Hou, Z., Gangjee, A., and Matherly, L.H. (2020). Therapeutic Targeting of Mitochondrial One-Carbon Metabolism in Cancer. Mol Cancer Ther *19*, 2245-2255.

DeNicola, G.M., Chen, P.H., Mullarky, E., Sudderth, J.A., Hu, Z., Wu, D., Tang, H., Xie, Y., Asara, J.M., Huffman, K.E., *et al.* (2015). NRF2 regulates serine biosynthesis in non-small cell lung cancer. Nat Genet *47*, 1475-1481.

Dorokhov, Y.L., Shindyapina, A.V., Sheshukova, E.V., and Komarova, T.V. (2015). Metabolic methanol: molecular pathways and physiological roles. Physiol Rev *95*, 603-644.

Du, R., Petritsch, C., Lu, K., Liu, P., Haller, A., Ganss, R., Song, H., Vandenberg, S., and Bergers, G. (2008). Matrix metalloproteinase-2 regulates vascular patterning and growth affecting tumor cell survival and invasion in GBM. Neuro Oncol *10*, 254-264.

Ducker, G.S., Chen, L., Morscher, R.J., Ghergurovich, J.M., Esposito, M., Teng, X., Kang, Y., and Rabinowitz, J.D. (2016). Reversal of Cytosolic One-Carbon Flux Compensates for Loss of the Mitochondrial Folate Pathway. Cell metabolism *23*, 1140-1153.

Ducker, G.S., and Rabinowitz, J.D. (2017). One-Carbon Metabolism in Health and Disease. Cell metabolism *25*, 27-42.

Eichinger, L., Pachebat, J.A., Glöckner, G., Rajandream, M.A., Sucgang, R., Berriman, M., Song, J., Olsen, R., Szafranski, K., Xu, Q., *et al.* (2005). The genome of the social amoeba Dictyostelium discoideum. Nature *435*, 43-57.

Elkin, M., and Vlodavsky, I. (2001). Tail vein assay of cancer metastasis. Curr Protoc Cell Biol *Chapter 19*, 19.12.11-19.12.17.

Fan, J., Ye, J., Kamphorst, J.J., Shlomi, T., Thompson, C.B., and Rabinowitz, J.D. (2014). Quantitative flux analysis reveals folate-dependent NADPH production. Nature *510*, 298-302.

Fantin, V.R., St-Pierre, J., and Leder, P. (2006). Attenuation of LDH-A expression uncovers a link between glycolysis, mitochondrial physiology, and tumor maintenance. Cancer Cell *9*, 425-434.

Farber, S., and Diamond, L.K. (1948). Temporary remissions in acute leukemia in children produced by folic acid antagonist, 4-aminopteroyl-glutamic acid. N Engl J Med *238*, 787-793.

Fendt, S.M., Frezza, C., and Erez, A. (2020). Targeting Metabolic Plasticity and Flexibility Dynamics for Cancer Therapy. Cancer Discov *10*, 1797-1807.

Ferlay J, E.M., Lam F, Colombet M, Mery L, Piñeros M, Znaor A, Soerjomataram I, Bray F (2020). Global Cancer Observatory: Cancer Today. In International Agency for Research on Cancer (Lyon, France).

Ferraro, G.B., Ali, A., Luengo, A., Kodack, D.P., Deik, A., Abbott, K.L., Bezwada, D., Blanc, L., Prideaux, B., Jin, X., *et al.* (2021). FATTY ACID SYNTHESIS IS REQUIRED FOR BREAST CANCER BRAIN METASTASIS. Nat Cancer *2*, 414-428.

Finkel, T. (2011). Signal transduction by reactive oxygen species. J Cell Biol *194*, 7-15.

Fogar, P., Basso, D., Pasquali, C., De Paoli, M., Sperti, C., Roveroni, G., Pedrazzoli, S., and Plebani, M. (1997). Neural cell adhesion molecule (N-CAM) in gastrointestinal neoplasias. Anticancer Res *17*, 1227-1230.

Fouquier d'Hérouël, A. (2021). monomeric/BrainSignalDistribution. (GitHub, Zenodo).

French, J.B., Jones, S.A., Deng, H., Pedley, A.M., Kim, D., Chan, C.Y., Hu, H., Pugh, R.J., Zhao, H., Zhang, Y., *et al.* (2016). Spatial colocalization and functional link of purinosomes with mitochondria. Science *351*, 733-737.

Fu, C., Sikandar, A., Donner, J., Zaburannyi, N., Herrmann, J., Reck, M., Wagner-Döbler, I., Koehnke, J., and Müller, R. (2017). The natural product carolacton inhibits folate-dependent C1 metabolism by targeting FolD/MTHFD. Nature communications *8*, 1529.

García-Cañaveras, J.C., Chen, L., and Rabinowitz, J.D. (2019). The Tumor Metabolic Microenvironment: Lessons from Lactate. Cancer Res *79*, 3155-3162.

Gerber, D.E. (2019). Phase 2 Study of TVB-2640 in KRAS Non-Small Cell Lung Carcinomas. (ClinicalTrials.gov), pp. This is a prospective one-arm, two-stage phase 2 trial of TVB-2640 in KRAS mutant NSCLC patients. 2613 patients will be treated with a minimum of 2641 cycle of TVB-2640 therapy over 2648 weeks.

Goulian, M., Bleile, B., and Tseng, B.Y. (1980). Methotrexate-induced misincorporation of uracil into DNA. Proceedings of the National Academy of Sciences of the United States of America *77*, 1956-1960.

Gowans, G.J., Hawley, S.A., Ross, F.A., and Hardie, D.G. (2013). AMP is a true physiological regulator of AMP-activated protein kinase by both allosteric activation and enhancing net phosphorylation. Cell metabolism *18*, 556-566.

Haeger, A., Wolf, K., Zegers, M.M., and Friedl, P. (2015). Collective cell migration: guidance principles and hierarchies. Trends in cell biology *25*, 556-566.

Hanahan, D. (2022). Hallmarks of Cancer: New Dimensions. Cancer Discov *12*, 31-46.

Hanahan, D., and Weinberg, R.A. (2000). The hallmarks of cancer. Cell *100*, 57-70.

Hanahan, D., and Weinberg, R.A. (2011). Hallmarks of cancer: the next generation. Cell *144*, 646-674.

Hardie, D.G., and Pan, D.A. (2002). Regulation of fatty acid synthesis and oxidation by the AMP-activated protein kinase. Biochem Soc Trans *30*, 1064-1070.

Hefetz, A., and Blum, M.S. (1978). Biosynthesis of formic acid by the poison glands of formicine ants. Biochim Biophys Acta *543*, 484-496.

Hiller, K., Hangebrauk, J., Jäger, C., Spura, J., Schreiber, K., and Schomburg, D. (2009). MetaboliteDetector: comprehensive analysis tool for targeted and nontargeted GC/MS based metabolome analysis. Anal Chem *81*, 3429-3439.

Hiller, K., Metallo, C., and Stephanopoulos, G. (2011). Elucidation of cellular metabolism via metabolomics and stable-isotope assisted metabolomics. Curr Pharm Biotechnol *12*, 1075-1086.

Hosios, A.M., Hecht, V.C., Danai, L.V., Johnson, M.O., Rathmell, J.C., Steinhauser, M.L., Manalis, S.R., and Vander Heiden, M.G. (2016). Amino Acids Rather than Glucose Account for the Majority of Cell Mass in Proliferating Mammalian Cells. Dev Cell *36*, 540-549.

Howe, A.K., Baldor, L.C., and Hogan, B.P. (2005). Spatial regulation of the cAMP-dependent protein kinase during chemotactic cell migration. Proceedings of the National Academy of Sciences of the United States of America *102*, 14320-14325.

Huang, J., Chen, K., Chen, J., Gong, W., Dunlop, N.M., Howard, O.M., Gao, Y., Bian, X.W., and Wang, J.M. (2010). The G-protein-coupled formylpeptide receptor FPR confers a more invasive phenotype on human glioblastoma cells. Br J Cancer *102*, 1052-1060.

Hughes, E.R., Winter, M.G., Duerkop, B.A., Spiga, L., Furtado de Carvalho, T., Zhu, W., Gillis, C.C., Büttner, L., Smoot, M.P., Behrendt, C.L.*, et al.* (2017). Microbial Respiration and Formate Oxidation as Metabolic Signatures of Inflammation-Associated Dysbiosis. Cell Host Microbe *21*, 208-219.

Hulkower, K.I., and Herber, R.L. (2011). Cell migration and invasion assays as tools for drug discovery. Pharmaceutics *3*, 107-124.

Hynes, R.O. (2009). The extracellular matrix: not just pretty fibrils. Science *326*, 1216-1219.

Ishay-Ronen, D., Diepenbruck, M., Kalathur, R.K.R., Sugiyama, N., Tiede, S., Ivanek, R., Bantug, G., Morini, M.F., Wang, J., Hess, C.*, et al.* (2019). Gain Fat-Lose Metastasis: Converting Invasive Breast Cancer Cells into Adipocytes Inhibits Cancer Metastasis. Cancer Cell *35*, 17-32.e16.

Jain, M., Nilsson, R., Sharma, S., Madhusudhan, N., Kitami, T., Souza, A.L., Kafri, R., Kirschner, M.W., Clish, C.B., and Mootha, V.K. (2012). Metabolite profiling identifies a key role for glycine in rapid cancer cell proliferation. Science *336*, 1040-1044.

Jin, X., Demere, Z., Nair, K., Ali, A., Ferraro, G.B., Natoli, T., Deik, A., Petronio, L., Tang, A.A., Zhu, C., *et al.* (2020). A metastasis map of human cancer cell lines. Nature *588*, 331-336.

Johnson, J.P. (1991). Cell adhesion molecules of the immunoglobulin supergene family and their role in malignant transformation and progression to metastatic disease. Cancer Metastasis Rev *10*, 11-22.

Kaiser, U., Auerbach, B., and Oldenburg, M. (1996). The neural cell adhesion molecule NCAM in multiple myeloma. Leuk Lymphoma *20*, 389-395.

Kalhan, S.C., and Hanson, R.W. (2012). Resurgence of serine: an often neglected but indispensable amino Acid. J Biol Chem *287*, 19786-19791.

Kapoore, R.V., and Vaidyanathan, S. (2016). Towards quantitative mass spectrometry-based metabolomics in microbial and mammalian systems. Philos Trans A Math Phys Eng Sci *374*.

Kapur, B.M., Vandenbroucke, A.C., Adamchik, Y., Lehotay, D.C., and Carlen, P.L. (2007). Formic acid, a novel metabolite of chronic ethanol abuse, causes neurotoxicity, which is prevented by folic acid. Alcohol Clin Exp Res *31*, 2114-2120.

Kawai, J., Toki, T., Ota, M., Inoue, H., Takata, Y., Asahi, T., Suzuki, M., Shimada, T., Ono, K., Suzuki, K., *et al.* (2019). Discovery of a Potent, Selective, and Orally Available MTHFD2 Inhibitor (DS18561882) with in Vivo Antitumor Activity. J Med Chem *62*, 10204-10220.

Keibler, M.A., Fendt, S.M., and Stephanopoulos, G. (2012). Expanding the concepts and tools of metabolic engineering to elucidate cancer metabolism. Biotechnol Prog *28*, 1409-1418.

Kersten, K., de Visser, K.E., van Miltenburg, M.H., and Jonkers, J. (2017). Genetically engineered mouse models in oncology research and cancer medicine. EMBO Mol Med *9*, 137-153.

Kiweler, N., Delbrouck, C., Pozdeev, V.I., Neises, L., Soriano-Baguet, L., Eiden, K., Xian, F., Benzarti, M., Haase, L., Koncina, E., *et al.* (2022). Mitochondria preserve an autarkic one-carbon cycle to confer growth-independent cancer cell migration and metastasis. Nature communications *13*, 2699.

Kocatürk, B., and Versteeg, H.H. (2015). Orthotopic injection of breast cancer cells into the mammary fat pad of mice to study tumor growth. J Vis Exp.

Kory, N., Wyant, G.A., Prakash, G., Uit de Bos, J., Bottanelli, F., Pacold, M.E., Chan, S.H., Lewis, C.A., Wang, T., Keys, H.R., *et al.* (2018). SFXN1 is a mitochondrial serine transporter required for one-carbon metabolism. Science *362*.

Kottakis, F., Nicolay, B.N., Roumane, A., Karnik, R., Gu, H., Nagle, J.M., Boukhali, M., Hayward, M.C., Li, Y.Y., Chen, T., *et al.* (2016). LKB1 loss links serine metabolism to DNA methylation and tumorigenesis. Nature *539*, 390-395.

Krakhmal, N.V., Zavyalova, M.V., Denisov, E.V., Vtorushin, S.V., and Perelmuter, V.M. (2015). Cancer Invasion: Patterns and Mechanisms. Acta Naturae *7*, 17-28.

Krupenko, S.A., and Krupenko, N.I. (2018). ALDH1L1 and ALDH1L2 Folate Regulatory Enzymes in Cancer. Adv Exp Med Biol *1032*, 127-143.

Kulis, M., and Esteller, M. (2010). DNA methylation and cancer. Adv Genet *70*, 27-56.

Labuschagne, C.F., van den Broek, N.J., Mackay, G.M., Vousden, K.H., and Maddocks, O.D. (2014). Serine, but not glycine, supports one-carbon metabolism and proliferation of cancer cells. Cell Rep *7*, 1248-1258.

Laplante, M., and Sabatini, D.M. (2009). An emerging role of mTOR in lipid biosynthesis. Curr Biol *19*, R1046-1052.

Lee, D., Xu, I.M., Chiu, D.K., Lai, R.K., Tse, A.P., Lan Li, L., Law, C.T., Tsang, F.H., Wei, L.L., Chan, C.Y., *et al.* (2017). Folate cycle enzyme MTHFD1L confers metabolic advantages in hepatocellular carcinoma. J Clin Invest *127*, 1856-1872.

Li, H., Fu, X., Yao, F., Tian, T., Wang, C., and Yang, A. (2019). MTHFD1L-Mediated Redox Homeostasis Promotes Tumor Progression in Tongue Squamous Cell Carcinoma. Front Oncol *9*, 1278.

Li, K., Shi, Y., Zhu, S., Shao, X., Li, H., Kuang, X., Li, S., Guo, X.F., and Li, D. (2021). N-3 polyunsaturated fatty acids effectively protect against neural tube defects in diabetic mice induced by streptozotocin. Food Funct *12*, 9188-9196.

Lin, B.F., and Shane, B. (1994). Expression of Escherichia coli folylpolyglutamate synthetase in the Chinese hamster ovary cell mitochondrion. J Biol Chem *269*, 9705-9713.

Liotta, L.A. (2016). Adhere, Degrade, and Move: The Three-Step Model of Invasion. Cancer Res *76*, 3115-3117.

Liou, G.Y., and Storz, P. (2010). Reactive oxygen species in cancer. Free Radic Res *44*, 479-496.

Liwnicz, B.H., and Rubinstein, L.J. (1979). The pathways of extraneural spread in metastasizing gliomas: a report of three cases and critical review of the literature. Hum Pathol *10*, 453-467.

Locasale, J.W., Grassian, A.R., Melman, T., Lyssiotis, C.A., Mattaini, K.R., Bass, A.J., Heffron, G., Metallo, C.M., Muranen, T., Sharfi, H.*, et al.* (2011). Phosphoglycerate dehydrogenase diverts glycolytic flux and contributes to oncogenesis. Nat Genet *43*, 869-874.

Loeb, L.A., and Harris, C.C. (2008). Advances in chemical carcinogenesis: a historical review and prospective. Cancer Res *68*, 6863-6872.

Lorenz, N.I., Sauer, B., Zeiner, P.S., Strecker, M.I., Luger, A.-L., Schulte, D., Mittelbronn, M., Alekseeva, T., Sevenich, L., Harter, P.N.*, et al.* (2022). AMP-kinase mediates adaptation of glioblastoma cells to conditions of the tumour microenvironment. bioRxiv, 2022.2003.2025.485624.

Lu, P., Takai, K., Weaver, V.M., and Werb, Z. (2011). Extracellular matrix degradation and remodeling in development and disease. Cold Spring Harb Perspect Biol *3*.

Luzzi, K.J., MacDonald, I.C., Schmidt, E.E., Kerkvliet, N., Morris, V.L., Chambers, A.F., and Groom, A.C. (1998). Multistep nature of metastatic inefficiency: dormancy of solitary cells after successful extravasation and limited survival of early micrometastases. Am J Pathol *153*, 865-873.

Ma, X.Y., Yu, J.T., Wu, Z.C., Zhang, Q., Liu, Q.Y., Wang, H.F., Wang, W., and Tan, L. (2012). Replication of the MTHFD1L gene association with late-onset Alzheimer's disease in a Northern Han Chinese population. J Alzheimers Dis *29*, 521-525.

Maddocks, O.D., Berkers, C.R., Mason, S.M., Zheng, L., Blyth, K., Gottlieb, E., and Vousden, K.H. (2013). Serine starvation induces stress and p53-dependent metabolic remodelling in cancer cells. Nature *493*, 542-546.

Maddocks, O.D., Labuschagne, C.F., Adams, P.D., and Vousden, K.H. (2016). Serine Metabolism Supports the Methionine Cycle and DNA/RNA Methylation through De Novo ATP Synthesis in Cancer Cells. Mol Cell *61*, 210-221.

Maddocks, O.D.K., Athineos, D., Cheung, E.C., Lee, P., Zhang, T., van den Broek, N.J.F., Mackay, G.M., Labuschagne, C.F., Gay, D., Kruiswijk, F.*, et al.* (2017). Modulating the therapeutic response of tumours to dietary serine and glycine starvation. Nature *544*, 372-376.

Mattaini, K.R., Sullivan, M.R., and Vander Heiden, M.G. (2016). The importance of serine metabolism in cancer. J Cell Biol *214*, 249-257.

Mayer, A., Schmidt, M., Seeger, A., Serras, A.F., Vaupel, P., and Schmidberger, H. (2014). GLUT-1 expression is largely unrelated to both hypoxia and the Warburg phenotype in squamous cell carcinomas of the vulva. BMC Cancer *14*, 760.

Medes, G., Thomas, A., and Weinhouse, S. (1953). Metabolism of neoplastic tissue. IV. A study of lipid synthesis in neoplastic tissue slices in vitro. Cancer Res *13*, 27-29.

Meiser, J., Schuster, A., Pietzke, M., Vande Voorde, J., Athineos, D., Oizel, K., Burgos-Barragan, G., Wit, N., Dhayade, S., Morton, J.P*., et al.* (2018). Increased formate overflow is a hallmark of oxidative cancer. Nature communications *9*, 1368.

Meiser, J., Tumanov, S., Maddocks, O., Labuschagne, C.F., Athineos, D., Van Den Broek, N., Mackay, G.M., Gottlieb, E., Blyth, K., Vousden, K*., et al.* (2016). Serine one-carbon catabolism with formate overflow. Science advances *2*, e1601273.

Mejia, N.R., and MacKenzie, R.E. (1985). NAD-dependent methylenetetrahydrofolate dehydrogenase is expressed by immortal cells. J Biol Chem *260*, 14616-14620.

Menendez, J.A., and Lupu, R. (2007). Fatty acid synthase and the lipogenic phenotype in cancer pathogenesis. Nat Rev Cancer *7*, 763-777.

Metallo, C.M., Gameiro, P.A., Bell, E.L., Mattaini, K.R., Yang, J., Hiller, K., Jewell, C.M., Johnson, Z.R., Irvine, D.J., Guarente, L*., et al.* (2011). Reductive glutamine metabolism by IDH1 mediates lipogenesis under hypoxia. Nature *481*, 380-384.

Meza-Junco, J., Montaño-Loza, A., and Aguayo-González, A. (2006). [Molecular basis of cancer]. Rev Invest Clin *58*, 56-70.

Modamio, J., Saraiva, C., Giro, G.G., Nickels, S.L., Jarazo, J., Antony, P., Barbuti, P., Hadler, R., Jäger, C., Krüger, R*., et al.* (2021). Synaptic decline precedes dopaminergic neuronal loss in human midbrain organoids harboring a triplication of the SNCA gene. bioRxiv, 2021.2007.2015.452499.

Molloy, A.M., Daly, S., Mills, J.L., Kirke, P.N., Whitehead, A.S., Ramsbottom, D., Conley, M.R., Weir, D.G., and Scott, J.M. (1997). Thermolabile variant of 5,10-methylenetetrahydrofolate reductase associated with low red-cell folates: implications for folate intake recommendations. Lancet *349*, 1591-1593.

Momb, J., Lewandowski, J.P., Bryant, J.D., Fitch, R., Surman, D.R., Vokes, S.A., and Appling, D.R. (2013). Deletion of Mthfd1l causes embryonic lethality and neural tube and craniofacial defects in mice. Proceedings of the National Academy of Sciences of the United States of America *110*, 549-554.

Moon, C.S. (2017). Estimations of the lethal and exposure doses for representative methanol symptoms in humans. Ann Occup Environ Med *29*, 44.

Mullen, A.R., Wheaton, W.W., Jin, E.S., Chen, P.H., Sullivan, L.B., Cheng, T., Yang, Y., Linehan, W.M., Chandel, N.S., and DeBerardinis, R.J. (2011). Reductive carboxylation supports growth in tumour cells with defective mitochondria. Nature *481*, 385-388.

Murray, G.I., Duncan, M.E., O'Neil, P., McKay, J.A., Melvin, W.T., and Fothergill, J.E. (1998). Matrix metalloproteinase-1 is associated with poor prognosis in oesophageal cancer. J Pathol *185*, 256-261.

Murray, G.I., Duncan, M.E., O'Neil, P., Melvin, W.T., and Fothergill, J.E. (1996). Matrix metalloproteinase-1 is associated with poor prognosis in colorectal cancer. Nat Med *2*, 461-462.

Naj, A.C., Beecham, G.W., Martin, E.R., Gallins, P.J., Powell, E.H., Konidari, I., Whitehead, P.L., Cai, G., Haroutunian, V., Scott, W.K*., et al.* (2010). Dementia revealed: novel chromosome 6 locus for late-onset Alzheimer disease provides genetic evidence for folate-pathway abnormalities. PLoS Genet *6*, e1001130.

Nakada, M., Nakamura, H., Ikeda, E., Fujimoto, N., Yamashita, J., Sato, H., Seiki, M., and Okada, Y. (1999). Expression and tissue localization of membrane-type 1, 2, and 3 matrix metalloproteinases in human astrocytic tumors. Am J Pathol *154*, 417-428.

Neophytou, C.M., Panagi, M., Stylianopoulos, T., and Papageorgis, P. (2021). The Role of Tumor Microenvironment in Cancer Metastasis: Molecular Mechanisms and Therapeutic Opportunities. Cancers (Basel) *13*.

Newman, A.C., Falcone, M., Huerta Uribe, A., Zhang, T., Athineos, D., Pietzke, M., Vazquez, A., Blyth, K., and Maddocks, O.D.K. (2021). Immune-regulated IDO1-dependent tryptophan metabolism is source of one-carbon units for pancreatic cancer and stellate cells. Mol Cell *81*, 2290-2302.e2297.

Nicholls, P. (1975). Formate as an inhibitor of cytochrome c oxidase. Biochem Biophys Res Commun *67*, 610-616.

Nilsson, R., Jain, M., Madhusudhan, N., Sheppard, N.G., Strittmatter, L., Kampf, C., Huang, J., Asplund, A., and Mootha, V.K. (2014). Metabolic enzyme expression highlights a key role for MTHFD2 and the mitochondrial folate pathway in cancer. Nature communications *5*, 3128.

Ning, S., Ma, S., Saleh, A.Q., Guo, L., Zhao, Z., and Chen, Y. (2018). SHMT2 Overexpression Predicts Poor Prognosis in Intrahepatic Cholangiocarcinoma. Gastroenterol Res Pract *2018*, 4369253.

Noguchi, K., Konno, M., Koseki, J., Nishida, N., Kawamoto, K., Yamada, D., Asaoka, T., Noda, T., Wada, H., Gotoh, K.*, et al.* (2018). The mitochondrial one-carbon metabolic pathway is associated with patient survival in pancreatic cancer. Oncol Lett *16*, 1827-1834.

Nogueira, V., Park, Y., Chen, C.C., Xu, P.Z., Chen, M.L., Tonic, I., Unterman, T., and Hay, N. (2008). Akt determines replicative senescence and oxidative or oncogenic premature senescence and sensitizes cells to oxidative apoptosis. Cancer Cell *14*, 458-470.

Osborn, M.J., Freeman, M., and Huennekens, F.M. (1958). Inhibition of dihydrofolic reductase by aminopterin and amethopterin. Proc Soc Exp Biol Med *97*, 429-431.

Oudin, A., Baus, V., Barthelemy, V., Fabian, C., Klein, E., Dieterle, M., Wantz, M., Hau, A.C., Dording, C., Bernard, A.*, et al.* (2021). Protocol for derivation of organoids and patient-derived orthotopic xenografts from glioma patient tumors. STAR Protoc *2*, 100534.

Overall, C.M., and López-Otín, C. (2002). Strategies for MMP inhibition in cancer: innovations for the post-trial era. Nat Rev Cancer *2*, 657-672.

Paget, S. (1989). The distribution of secondary growths in cancer of the breast. 1889. Cancer Metastasis Rev *8*, 98-101.

Pareek, V., Tian, H., Winograd, N., and Benkovic, S.J. (2020). Metabolomics and mass spectrometry imaging reveal channeled de novo purine synthesis in cells. Science *368*, 283-290.

Parle-McDermott, A., Pangilinan, F., O'Brien, K.K., Mills, J.L., Magee, A.M., Troendle, J., Sutton, M., Scott, J.M., Kirke, P.N., Molloy, A.M.*, et al.* (2009). A common variant in MTHFD1L is associated with neural tube defects and mRNA splicing efficiency. Hum Mutat *30*, 1650-1656.

Pasquier, B., Pasquier, D., N'Golet, A., Panh, M.H., and Couderc, P. (1980). Extraneural metastases of astrocytomas and glioblastomas: clinicopathological study of two cases and review of literature. Cancer *45*, 112-125.

Paukert, J.L., Williams, G.R., and Rabinowitz, J.C. (1977). Formyl-methenyl-methylenetetrahydrofolate synthetase (combined); correlation of enzymic activities with limited proteolytic degradation of the protein from yeast. Biochem Biophys Res Commun *77*, 147-154.

Pavlova, N.N., and Thompson, C.B. (2016). The Emerging Hallmarks of Cancer Metabolism. Cell metabolism *23*, 27-47.

Pearson, G.W. (2019). Control of Invasion by Epithelial-to-Mesenchymal Transition Programs during Metastasis. J Clin Med *8*.

Pham, V.T., Lacroix, C., Braegger, C.P., and Chassard, C. (2017). Lactate-utilizing community is associated with gut microbiota dysbiosis in colicky infants. Sci Rep *7*, 11176.

Pietzke, M., Meiser, J., and Vazquez, A. (2020). Formate metabolism in health and disease. Mol Metab *33*, 23-37.

Pike, S.T., Rajendra, R., Artzt, K., and Appling, D.R. (2010). Mitochondrial C1-tetrahydrofolate synthase (MTHFD1L) supports the flow of mitochondrial one-carbon units into the methyl cycle in embryos. J Biol Chem *285*, 4612-4620.

Piraud, R.S.a.C.B.a.M. (2022). Automatic-Cell-Counter. (GitHub, Zenodo).

Piskounova, E., Agathocleous, M., Murphy, M.M., Hu, Z., Huddlestun, S.E., Zhao, Z., Leitch, A.M., Johnson, T.M., DeBerardinis, R.J., and Morrison, S.J. (2015). Oxidative stress inhibits distant metastasis by human melanoma cells. Nature *527*, 186-191.

Pollari, S., Käkönen, S.M., Edgren, H., Wolf, M., Kohonen, P., Sara, H., Guise, T., Nees, M., and Kallioniemi, O. (2011). Enhanced serine production by bone metastatic breast cancer cells stimulates osteoclastogenesis. Breast Cancer Res Treat *125*, 421-430.

Porporato, P.E., Payen, V.L., Pérez-Escuredo, J., De Saedeleer, C.J., Danhier, P., Copetti, T., Dhup, S., Tardy, M., Vazeille, T., Bouzin, C*., et al.* (2014). A mitochondrial switch promotes tumor metastasis. Cell Rep *8*, 754-766.

Porstmann, T., Santos, C.R., Lewis, C., Griffiths, B., and Schulze, A. (2009). A new player in the orchestra of cell growth: SREBP activity is regulated by mTORC1 and contributes to the regulation of cell and organ size. Biochem Soc Trans *37*, 278-283.

Possemato, R., Marks, K.M., Shaul, Y.D., Pacold, M.E., Kim, D., Birsoy, K., Sethumadhavan, S., Woo, H.K., Jang, H.G., Jha, A.K*., et al.* (2011). Functional genomics reveal that the serine synthesis pathway is essential in breast cancer. Nature *476*, 346-350.

Prasannan, P., and Appling, D.R. (2009). Human mitochondrial C1-tetrahydrofolate synthase: submitochondrial localization of the full-length enzyme and characterization of a short isoform. Arch Biochem Biophys *481*, 86-93.

Prasannan, P., Pike, S., Peng, K., Shane, B., and Appling, D.R. (2003). Human mitochondrial C1-tetrahydrofolate synthase: gene structure, tissue distribution of the mRNA, and immunolocalization in Chinese hamster ovary calls. J Biol Chem *278*, 43178-43187.

Ren, R.J., Wang, L.L., Fang, R., Liu, L.H., Wang, Y., Tang, H.D., Deng, Y.L., Xu, W., Wang, G., and Chen, S.D. (2011). The MTHFD1L gene rs11754661 marker is associated with susceptibility to Alzheimer's disease in the Chinese Han population. J Neurol Sci *308*, 32-34.

Rhee, S.G. (2006). Cell signaling. H2O2, a necessary evil for cell signaling. Science *312*, 1882-1883.

Robert, S.M., Buckingham, S.C., Campbell, S.L., Robel, S., Holt, K.T., Ogunrinu-Babarinde, T., Warren, P.P., White, D.M., Reid, M.A., Eschbacher, J.M*., et al.* (2015). SLC7A11 expression is associated with seizures and predicts poor survival in patients with malignant glioma. Sci Transl Med *7*, 289ra286.

Ron Milo, R.P. (2015). Cell biology by the numbers, Vol 1st Edition (Garland Science).

Rossi, M., Amaretti, A., and Raimondi, S. (2011). Folate production by probiotic bacteria. Nutrients *3*, 118-134.

Samani, N.J., Erdmann, J., Hall, A.S., Hengstenberg, C., Mangino, M., Mayer, B., Dixon, R.J., Meitinger, T., Braund, P., Wichmann, H.E*., et al.* (2007). Genomewide association analysis of coronary artery disease. N Engl J Med *357*, 443-453.

Savci-Heijink, C.D., Halfwerk, H., Hooijer, G.K., Horlings, H.M., Wesseling, J., and van de Vijver, M.J. (2015). Retrospective analysis of metastatic behaviour of breast cancer subtypes. Breast Cancer Res Treat *150*, 547-557.

Saxena, M., Balaji, S.A., Deshpande, N., Ranganathan, S., Pillai, D.M., Hindupur, S.K., and Rangarajan, A. (2018). AMP-activated protein kinase promotes epithelial-mesenchymal transition in cancer cells through Twist1 upregulation. J Cell Sci *131*.

Schaeffer, D., Somarelli, J.A., Hanna, G., Palmer, G.M., and Garcia-Blanco, M.A. (2014). Cellular migration and invasion uncoupled: increased migration is not an inexorable consequence of epithelial-to-mesenchymal transition. Mol Cell Biol *34*, 3486-3499.

Schneider, C.A., Rasband, W. S., & Eliceiri, K. W. (2012). NIH Image to ImageJ: 25 years of image analysis. . (Nature Methods).

Schuster, A., Klein, E., Neirinckx, V., Knudsen, A.M., Fabian, C., Hau, A.C., Dieterle, M., Oudin, A., Nazarov, P.V., Golebiewska, A.*, et al.* (2020). AN1-type zinc finger protein 3 (ZFAND3) is a transcriptional regulator that drives Glioblastoma invasion. Nature communications *11*, 6366.

Shannon, K.W., and Rabinowitz, J.C. (1986). Purification and characterization of a mitochondrial isozyme of C1-tetrahydrofolate synthase from Saccharomyces cerevisiae. J Biol Chem *261*, 12266-12271.

Shannon, K.W., and Rabinowitz, J.C. (1988). Isolation and characterization of the Saccharomyces cerevisiae MIS1 gene encoding mitochondrial C1-tetrahydrofolate synthase. J Biol Chem *263*, 7717-7725.

Shima, I., Sasaguri, Y., Kusukawa, J., Yamana, H., Fujita, H., Kakegawa, T., and Morimatsu, M. (1992). Production of matrix metalloproteinase-2 and metalloproteinase-3 related to malignant behavior of esophageal carcinoma. A clinicopathologic study. Cancer *70*, 2747-2753.

Shin, M., Momb, J., and Appling, D.R. (2017). Human mitochondrial MTHFD2 is a dual redox cofactor-specific methylenetetrahydrofolate dehydrogenase/methenyltetrahydrofolate cyclohydrolase. Cancer Metab *5*, 11.

Siegel, R.L., Miller, K.D., and Jemal, A. (2020). Cancer statistics, 2020. CA Cancer J Clin *70*, 7-30.

Sincevičiūtė, R., Vaitkienė, P., Urbanavičiūtė, R., Steponaitis, G., Tamašauskas, A., and Skiriutė, D. (2018). MMP2 is associated with glioma malignancy and patient outcome. Int J Clin Exp Pathol *11*, 3010-3018.

Snell, K. (1985). Enzymes of serine metabolism in normal and neoplastic rat tissues. Biochim Biophys Acta *843*, 276-281.

Snell, K., Natsumeda, Y., Eble, J.N., Glover, J.L., and Weber, G. (1988). Enzymic imbalance in serine metabolism in human colon carcinoma and rat sarcoma. Br J Cancer *57*, 87-90.

Sonveaux, P., Végran, F., Schroeder, T., Wergin, M.C., Verrax, J., Rabbani, Z.N., De Saedeleer, C.J., Kennedy, K.M., Diepart, C., Jordan, B.F.*, et al.* (2008). Targeting lactate-fueled respiration selectively kills hypoxic tumor cells in mice. J Clin Invest *118*, 3930-3942.

Soto-Guzman, A., Navarro-Tito, N., Castro-Sanchez, L., Martinez-Orozco, R., and Salazar, E.P. (2010). Oleic acid promotes MMP-9 secretion and invasion in breast cancer cells. Clin Exp Metastasis *27*, 505-515.

Sugiura, T., Nagano, Y., Inoue, T., and Hirotani, K. (2004). A novel mitochondrial C1-tetrahydrofolate synthetase is upregulated in human colon adenocarcinoma. Biochem Biophys Res Commun *315*, 204-211.

Sun, K., Tang, S., Hou, Y., Xi, L., Chen, Y., Yin, J., Peng, M., Zhao, M., Cui, X., and Liu, M. (2019). Oxidized ATM-mediated glycolysis enhancement in breast cancer-associated fibroblasts contributes to tumor invasion through lactate as metabolic coupling. EBioMedicine *41*, 370-383.

Taddei, M.L., Giannoni, E., Comito, G., and Chiarugi, P. (2013). Microenvironment and tumor cell plasticity: an easy way out. Cancer Lett *341*, 80-96.

Taïb, B., Aboussalah, A.M., Moniruzzaman, M., Chen, S., Haughey, N.J., Kim, S.F., and Ahima, R.S. (2019). Lipid accumulation and oxidation in glioblastoma multiforme. Sci Rep *9*, 19593.

Tedeschi, P.M., Markert, E.K., Gounder, M., Lin, H., Dvorzhinski, D., Dolfi, S.C., Chan, L.L., Qiu, J., DiPaola, R.S., Hirshfield, K.M.*, et al.* (2013). Contribution of serine, folate and glycine metabolism to the ATP, NADPH and purine requirements of cancer cells. Cell death & disease *4*, e877.

Tepper, N., and Shlomi, T. (2015). Efficient Modeling of MS/MS Data for Metabolic Flux Analysis. PLoS One *10*, e0130213.

Ternes, D., Tsenkova, M., Pozdeev, V.I., Meyers, M., Koncina, E., Atatri, S., Schmitz, M., Karta, J., Schmoetten, M., Heinken, A.*, et al.* (2022). The gut microbial metabolite formate exacerbates colorectal cancer progression. Nature Metabolism.

Tibbetts, A.S., and Appling, D.R. (2010). Compartmentalization of Mammalian folate-mediated one-carbon metabolism. Annu Rev Nutr *30*, 57-81.

Timmerman, L.A., Holton, T., Yuneva, M., Louie, R.J., Padró, M., Daemen, A., Hu, M., Chan, D.A., Ethier, S.P., van 't Veer, L.J.*, et al.* (2013). Glutamine sensitivity analysis identifies the xCT antiporter as a common triple-negative breast tumor therapeutic target. Cancer Cell *24*, 450-465.

Titus, S.A., and Moran, R.G. (2000). Retrovirally mediated complementation of the glyB phenotype. Cloning of a human gene encoding the carrier for entry of folates into mitochondria. J Biol Chem *275*, 36811-36817.

Tolsma, T.O., and Hansen, J.C. (2019). Post-translational modifications and chromatin dynamics. Essays Biochem *63*, 89-96.

Trachootham, D., Zhou, Y., Zhang, H., Demizu, Y., Chen, Z., Pelicano, H., Chiao, P.J., Achanta, G., Arlinghaus, R.B., Liu, J.*, et al.* (2006). Selective killing of oncogenically transformed cells through a ROS-mediated mechanism by beta-phenylethyl isothiocyanate. Cancer Cell *10*, 241-252.

Van Dam, F., and Van Gool, W.A. (2009). Hyperhomocysteinemia and Alzheimer's disease: A systematic review. Arch Gerontol Geriatr *48*, 425-430.

Vande Voorde, J., Ackermann, T., Pfetzer, N., Sumpton, D., Mackay, G., Kalna, G., Nixon, C., Blyth, K., Gottlieb, E., and Tardito, S. (2019). Improving the metabolic fidelity of cancer models with a physiological cell culture medium. Science advances *5*, eaau7314.

Vander Heiden, M.G., Cantley, L.C., and Thompson, C.B. (2009). Understanding the Warburg effect: the metabolic requirements of cell proliferation. Science *324*, 1029-1033.

Vazquez, A., Markert, E.K., and Oltvai, Z.N. (2011). Serine biosynthesis with one carbon catabolism and the glycine cleavage system represents a novel pathway for ATP generation. PLoS One *6*, e25881.

Visse, R., and Nagase, H. (2003). Matrix metalloproteinases and tissue inhibitors of metalloproteinases: structure, function, and biochemistry. Circ Res *92*, 827-839.

Vogel, F.C.E., and Schulze, A. (2021). Fatty acid synthesis enables brain metastasis. Nat Cancer *2*, 374-376.

W. Kelly, J. Michalek, A.E. Diaz Duque, V. Madhusudanannair, L. Caflisch, B. Konkel, J. Floyd, and Brenner, A. (2020). 368MO Fatty acid synthase inhibitor TVB-2640 with bevacizumab in recurrent glioblastoma,. Annals of Oncology, *Volume 31, Supplement 4,*.

Walkup, A.S., and Appling, D.R. (2005). Enzymatic characterization of human mitochondrial C1-tetrahydrofolate synthase. Arch Biochem Biophys *442*, 196-205.

Wang, H., Li, X.T., Wu, C., Wu, Z.W., Li, Y.Y., Yang, T.Q., Chen, G.L., Xie, X.S., Huang, Y.L., Du, Z.W.*, et al.* (2015). miR-132 can inhibit glioma cells invasion and migration by target MMP16 in vitro. Onco Targets Ther *8*, 3211-3218.

Wang, L., Xiong, H., Wu, F., Zhang, Y., Wang, J., Zhao, L., Guo, X., Chang, L.J., Zhang, Y., You, M.J.*, et al.* (2014). Hexokinase 2-mediated Warburg effect is required for PTEN- and p53-deficiency-driven prostate cancer growth. Cell Rep *8*, 1461-1474.

Wang, M., Wang, T., Liu, S., Yoshida, D., and Teramoto, A. (2003). The expression of matrix metalloproteinase-2 and -9 in human gliomas of different pathological grades. Brain Tumor Pathol *20*, 65-72.

Wang, Y., Stancliffe, E., Fowle-Grider, R., Wang, R., Wang, C., Schwaiger-Haber, M., Shriver, L.P., and Patti, G.J. (2022). Saturation of the mitochondrial NADH shuttles drives aerobic glycolysis in proliferating cells. Mol Cell.

Warburg, O. (1956). On the origin of cancer cells. Science *123*, 309-314.

Warburg, O., Wind, F., and Negelein, E. (1927). THE METABOLISM OF TUMORS IN THE BODY. J Gen Physiol *8*, 519-530.

Welch, D.R., and Hurst, D.R. (2019). Defining the Hallmarks of Metastasis. Cancer Res *79*, 3011-3027.

Westermarck, J., and Kähäri, V.M. (1999). Regulation of matrix metalloproteinase expression in tumor invasion. Faseb j *13*, 781-792.

Winer, A., Adams, S., and Mignatti, P. (2018). Matrix Metalloproteinase Inhibitors in Cancer Therapy: Turning Past Failures Into Future Successes. Mol Cancer Ther *17*, 1147-1155.

Wisniewski, J.R., Zougman, A., and Mann, M. (2008). Nepsilon-formylation of lysine is a widespread post-translational modification of nuclear proteins occurring at residues involved in regulation of chromatin function. Nucleic Acids Res *36*, 570-577.

Wong, N., Ojo, D., Yan, J., and Tang, D. (2015). PKM2 contributes to cancer metabolism. Cancer Lett *356*, 184-191.

Wray, J. (1670). Some uncommon observations and experiments made with an acid juyce to be found in ants. Phil. Trans. Roy. Soc. London *2063-2069*.

Wu, J.S., Jiang, J., Chen, B.J., Wang, K., Tang, Y.L., and Liang, X.H. (2021). Plasticity of cancer cell invasion: Patterns and mechanisms. Transl Oncol *14*, 100899.

Wu, M., Wanggou, S., Li, X., Liu, Q., and Xie, Y. (2017). Overexpression of mitochondrial serine hydroxyl-methyltransferase 2 is associated with poor prognosis and promotes cell proliferation and invasion in gliomas. Onco Targets Ther *10*, 3781-3788.

Yang, M., and Vousden, K.H. (2016). Serine and one-carbon metabolism in cancer. Nat Rev Cancer *16*, 650-662.

Yao, C.H., Liu, G.Y., Yang, K., Gross, R.W., and Patti, G.J. (2016). Inaccurate quantitation of palmitate in metabolomics and isotope tracer studies due to plastics. Metabolomics *12*.

Ye, J., Fan, J., Venneti, S., Wan, Y.W., Pawel, B.R., Zhang, J., Finley, L.W., Lu, C., Lindsten, T., Cross, J.R.*, et al.* (2014). Serine catabolism regulates mitochondrial redox control during hypoxia. Cancer Discov *4*, 1406-1417.

Ye, R.D., Boulay, F., Wang, J.M., Dahlgren, C., Gerard, C., Parmentier, M., Serhan, C.N., and Murphy, P.M. (2009). International Union of Basic and Clinical Pharmacology. LXXIII. Nomenclature for the formyl peptide receptor (FPR) family. Pharmacol Rev *61*, 119-161.

Yin, J., Ren, W., Huang, X., Deng, J., Li, T., and Yin, Y. (2018). Potential Mechanisms Connecting Purine Metabolism and Cancer Therapy. Front Immunol *9*, 1697.

Yin, K. (2015). Positive correlation between expression level of mitochondrial serine hydroxymethyltransferase and breast cancer grade. Onco Targets Ther *8*, 1069-1074.

Young, A., Gardiner, D., Brosnan, M.E., Brosnan, J.T., and Mailloux, R.J. (2017). Physiological levels of formate activate mitochondrial superoxide/hydrogen peroxide release from mouse liver mitochondria. FEBS Lett *591*, 2426-2438.

Zhang, B., Zheng, A., Hydbring, P., Ambroise, G., Ouchida, A.T., Goiny, M., Vakifahmetoglu-Norberg, H., and Norberg, E. (2017). PHGDH Defines a Metabolic Subtype in Lung Adenocarcinomas with Poor Prognosis. Cell Rep *19*, 2289-2303.

Zhang, L., Chen, Z., Xue, D., Zhang, Q., Liu, X., Luh, F., Hong, L., Zhang, H., Pan, F., Liu, Y.*, et al.* (2016). Prognostic and therapeutic value of mitochondrial serine hydroxyl-methyltransferase 2 as a breast cancer biomarker. Oncol Rep *36*, 2489-2500.

Supplementary Figures

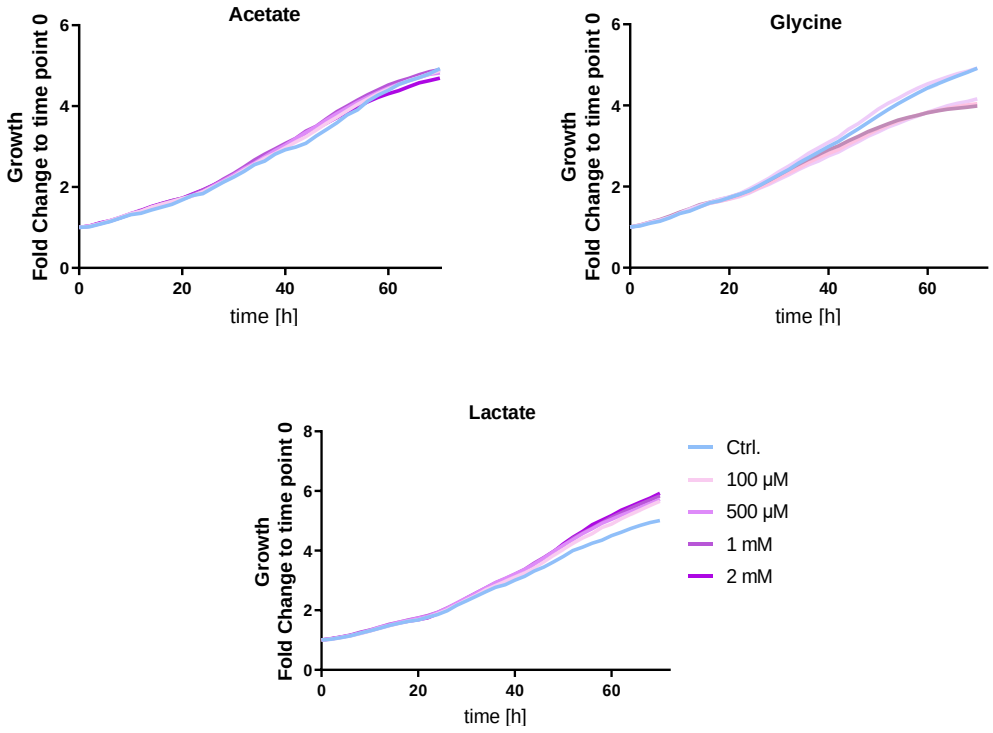

Supplementary Figure 1.1: Small Metabolites do Not Affect the Proliferation of LN-229 Cells
Proliferation curves of LN-229 cells that were treated for 72 hours with different concentrations (0 µM, 100 µM, 500 µM, 1mM, and 2mM) of small metabolites (Na-acetate, glycine, Na-lactate). The curves display the fold change with respect to time point zero.

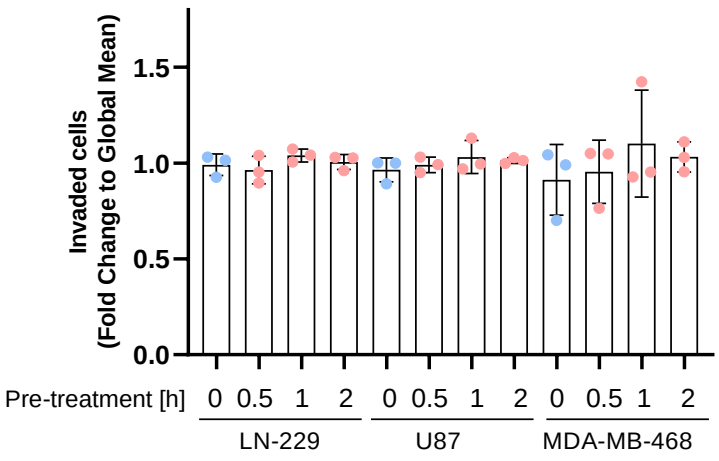

Supplementary Figure 2.1: 2 Hours of Formate Treatment do Not Prime Cancer Cells to an Invasive Phenotype
Invasion of LN-229, U87, and MDA-MB-468 cells that were pre-treated for 0, 0.5, 1, and 2 hours with 500 µM Na-formate. The invasion was assessed using ECM-collagen-coated Boyden chambers. Each dot represents an independent experiment, the bars represent the mean, and the error bars visualize the standard deviation (SD).

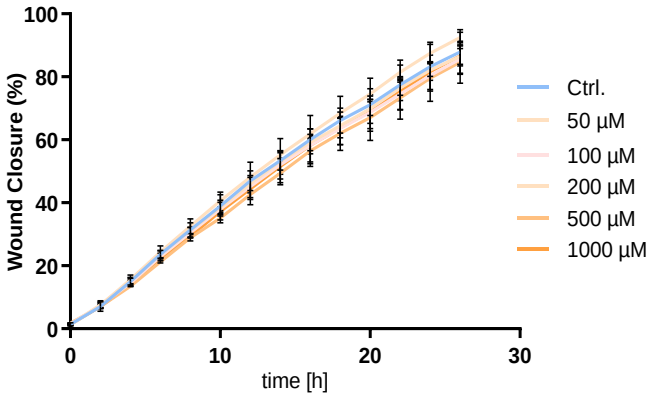

Supplementary Figure 4.1: Formate does Not Impact Cancer Cell Migration
The migratory potential of LN-229 cells in response to different formate concentrations (0 µM, 50 µM, 100 µM, 200 µM, 500 µM, and 1000 µM) assessed through a time-dependent quantification of relative wound density in IncuCyte. Each graph represents the mean of 3 independent experiments and the error bars visualize the standard error of the mean (SEM).

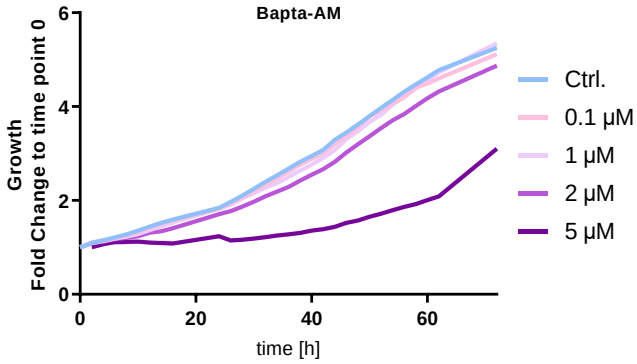

Supplementary Figure 4.2: Bapta-AM Does Not Impact Cancer Cell Proliferation
Proliferation curves of LN-229 cells that were treated for 72 hours with different Bapta-AM concentrations (0 µM, 0.1 µM, 1 µM, 2 µM, and 5 µM). The curves display the fold change with respect to time point zero.

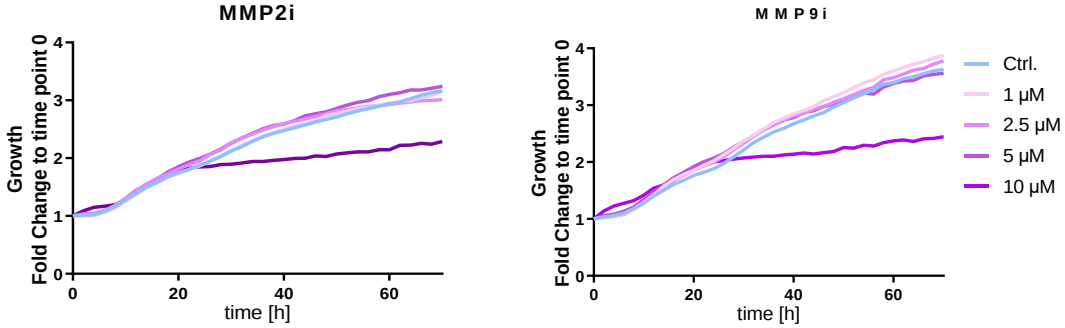

Supplementary Figure 4.3: MMPi does Not Impact Cancer Cell Proliferation
Proliferation curves of LN-229 cells that were treated for 72 hours with different concentrations (0 µM, 1 µM, 2.5 µM, 5 µM, and 10 µM) of MMP2 or MMP9 inhibitors. The curves display the fold change with respect to time point zero.

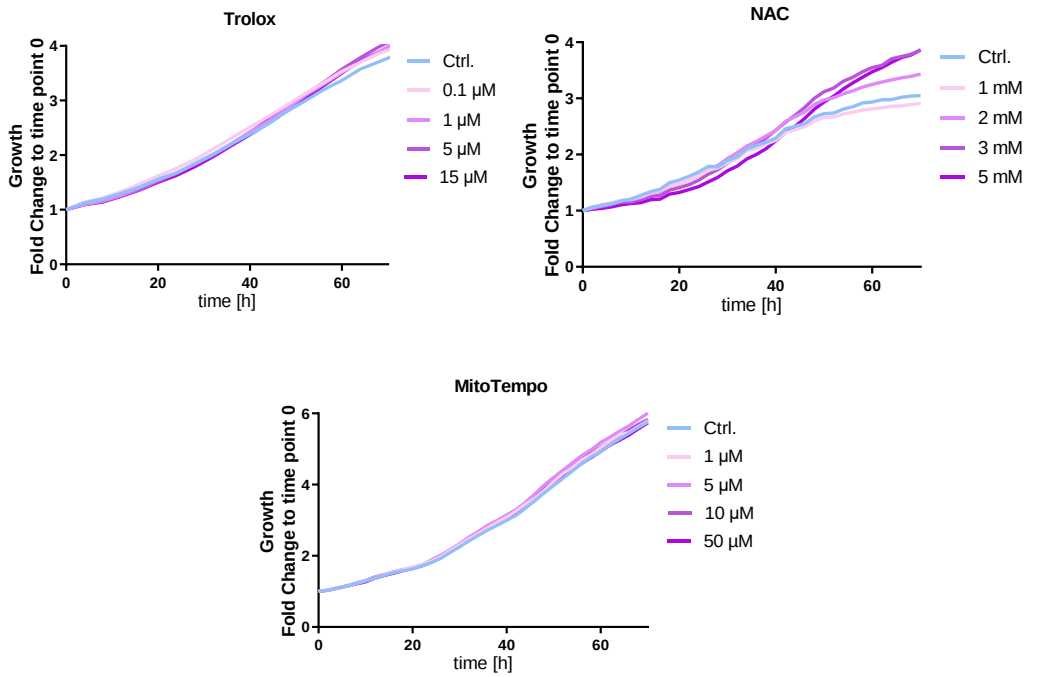

Supplementary Figure 5.1: ROS Scavengers do Not Impact Cancer Cell Proliferation
Proliferation curves of LN-229 cells that were treated for 72 hours with different concentrations of Trolox (0 µM, 0.1 µM, 1 µM, 5 µM, and 15 µM), NAC (0 mM, 1 mM, 2 mM, 3 mM, and 5 mM) and MitoTempo (0 µM, 1 µM, 5 µM, 10 µM, and 50 µM). The curves display the fold change with respect to time point zero.

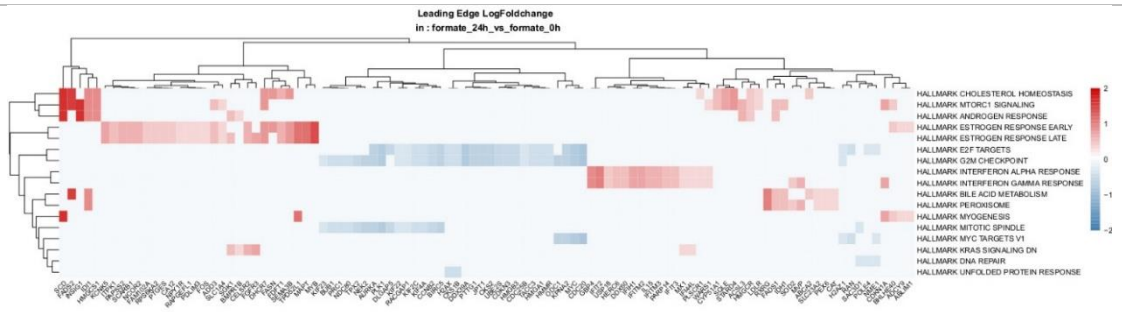

Supplementary Figure 5.2: GSEA Analysis
Gene set enrichment analysis (GSEA) representing LN-229 cells treated for 24 hours with 500 µM formate compared to LN-229 control cells. The measurement stems from RNAseq data.

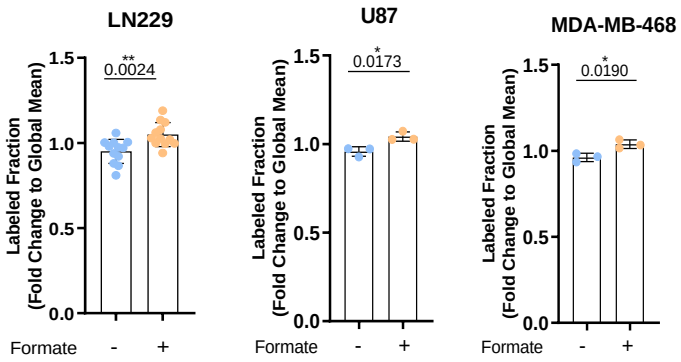

Supplementary Figure 5.3: Formate Promotes Fatty Acid Synthesis
Labelled fraction of Hexadecenoic acid 2 upon the addition of [U-^{13}C]glucose and [U-^{13}C]glutamine tracer in response to 72 hours of 500 µM formate treatment in LN-229, U87, and MDA-MB-468 cells. Each dot represents an independent experiment with triplicate wells, the bars represent the mean, and the error bars visualize the standard deviation (SD). The data was evaluated using an unpaired *t*-test with Welch's correction.

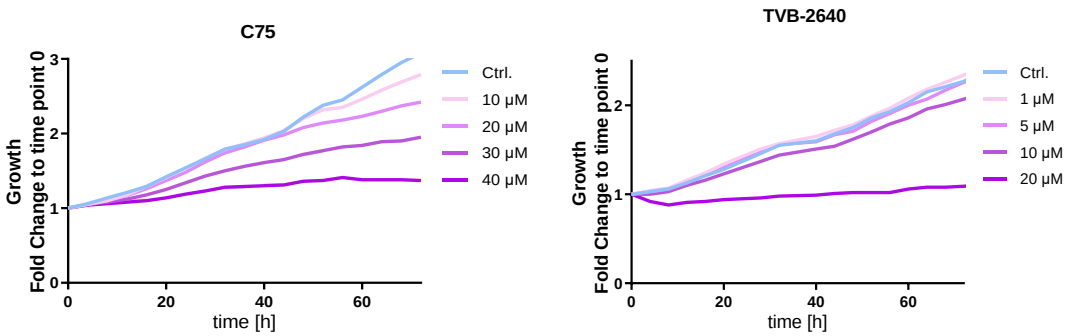

Supplementary Figure 5.4: FASN Inhibitors do Not Impact Cancer Cell Proliferation
Proliferation curves of LN-229 cells that were treated for 72 hours with different concentrations of the FASN inhibitors: C75 (0 µM, 10 µM, 20 µM, 30 µM, and 40 µM) and TVB-2640 (0 µM, 1 µM, 5 µM, 10 µM, and 20 µM). The curves display the fold change with respect to time point zero.

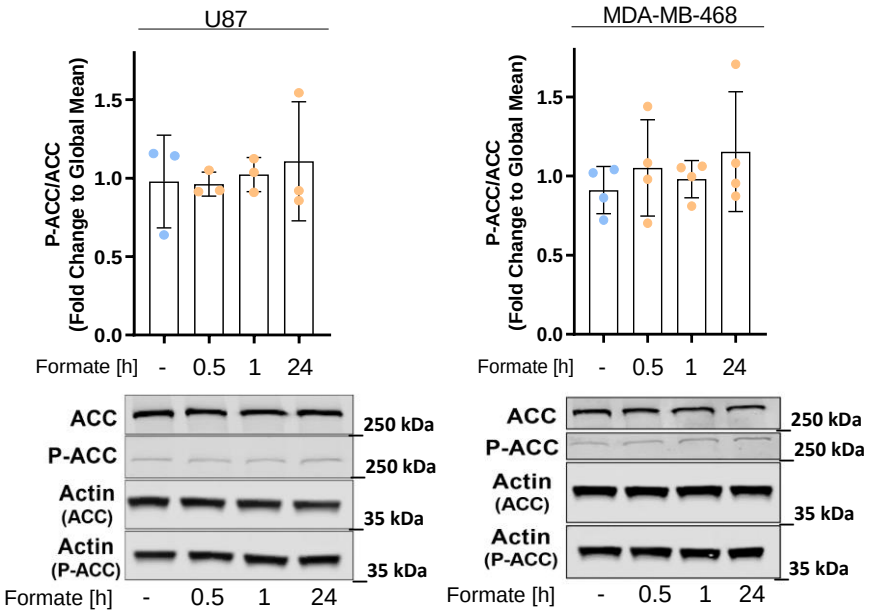

Supplementary Figure 6.1: Formate does Not Impact ACC Activity
Expression of ACC and the corresponding phosphorylated protein in U87 and MDA-MB-468 cells pre-treated for different durations (0, 0.5, 1, and 24 hours) with 500 µM formate. The signal intensity of P-ACC and ACC has been quantified with respect to the signal intensity of β-actin. Each dot represents an independent experiment, the bars represent the mean, and the error bars visualize the standard deviation.

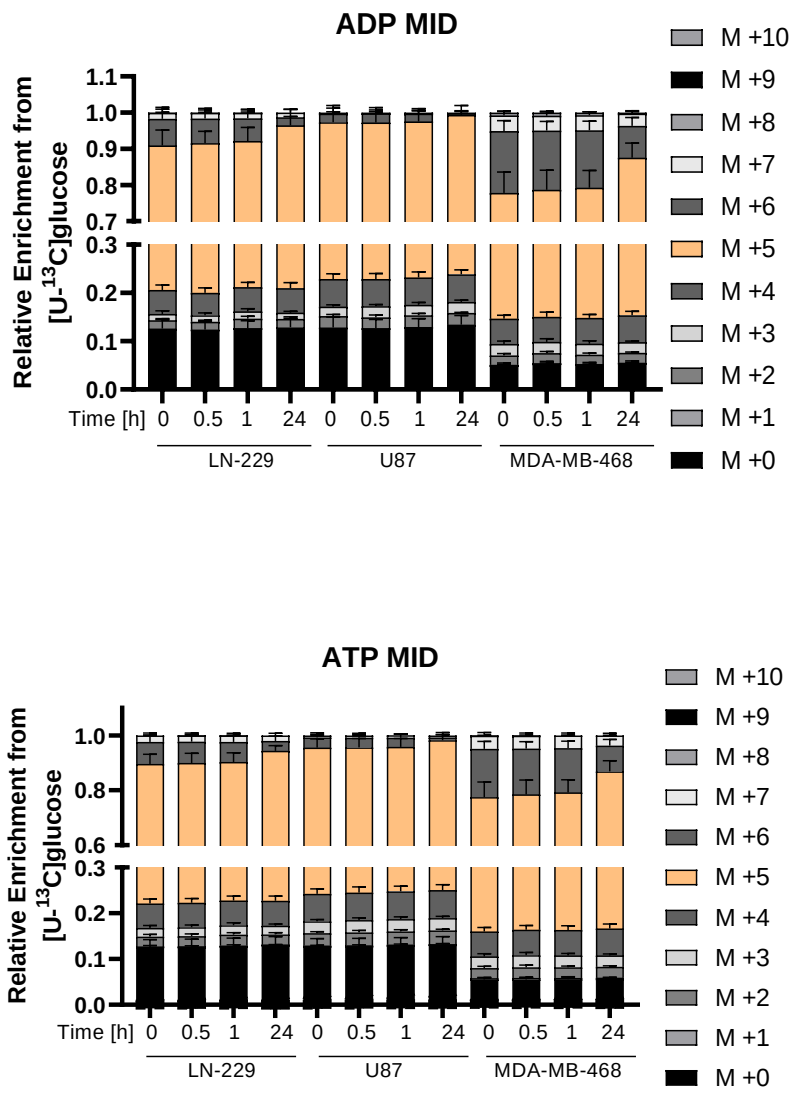

Supplementary Figure 6.2: Formate Triggers ADP and ATP Synthesis
MID of intracellular ADP and ATP after the addition of [U-^{13}C]glucose tracer in LN-229, U87, and MDA-MB-468 cells in response to different durations (0, 0.5, 1, and 24 hours) of 500 µM formate treatment. Each bar represents the mean of 3 independent experiments in triplicate wells. The error bars visualize the standard error of the mean (SEM).